Rep. Prog. Phys. **62** (1999) 1573–1659. Printed in the UK PII: S0034-4885(99)42161-X

Phase separation in confined systems

Lev D Gelb†§, K E Gubbins†, R Radhakrishnan† and M Sliwinska-Bartkowiak‡

† North Carolina State University, Department of Chemical Engineering, 113 Riddick Labs, Raleigh, NC 27695-7905, USA

‡ Instytut Fizyki, Uniwersytet im Adama Mickiewicza, ul Grunwaldzka 6, 60-780 Poznan, Poland

Received 12 April 1999

Abstract

We review the current state of knowledge of phase separation and phase equilibria in porous materials. Our emphasis is on fundamental studies of simple fluids (composed of small, neutral molecules) and well-characterized materials. While theoretical and molecular simulation studies are stressed, we also survey experimental investigations that are fundamental in nature. Following a brief survey of the most useful theoretical and simulation methods, we describe the nature of gas–liquid (capillary condensation), layering, liquid–liquid and freezing/melting transitions. In each case studies for simple pore geometries, and also more complex ones where available, are discussed. While a reasonably good understanding is available for phase equilibria of pure adsorbates in simple pore geometries, there is a need to extend the models to more complex pore geometries that include effects of chemical and geometrical heterogeneity and connectivity. In addition, with the exception of liquid–liquid equilibria, little work has been done so far on phase separation for mixtures in porous media.

§ Present address: Department of Chemistry, Florida State University, Tallahassee, FL 32306-4390, USA.

0034-4885/99/121573+87$90.00

Contents

		Page
1.	Introduction	1575
2.	Simulation and theoretical methods	1580
	2.1. Grand canonical Monte Carlo	1580
	2.2. Gibbs ensemble Monte Carlo	1582
	2.3. Semi-grand Monte Carlo	1582
	2.4. Quench molecular dynamics	1582
	2.5. Lattice models	1583
	2.6. Histogram analysis methods	1584
	2.7. Histogram-biased Monte Carlo simulations	1584
	2.8. Density functional theory	1585
	2.9. Intermolecular potential functions	1586
3.	Capillary condensation	1587
	3.1. Experimental studies	1588
	3.2. Theoretical and simulation studies: simple pore geometries	1595
	3.3. Theoretical and simulation studies: complex pore geometries	1606
4.	Layering transitions	1617
	4.1. Experiments	1617
	4.2. Theoretical treatments and systematics of surface phase transitions	1618
	4.3. Molecular simulation	1621
5.	Liquid–liquid equilibria	1622
	5.1. Experimental results	1624
	5.2. Lattice models	1632
	5.3. Molecular simulation results	1633
6.	Freezing	1637
	6.1. Experiments on freezing/melting	1638
	6.2. Simulation studies: simple pore geometries	1642
	6.3. Simulation studies: complex pore geometries	1649
	6.4. Freezing versus glass transition	1650
7.	Conclusions	1651
	Acknowledgments	1652
	References	1652

1. Introduction

Molecules confined within narrow pores, with pore widths of a few molecular diameters, can exhibit a wide range of physical behaviour. The introduction of wall forces, and the competition between fluid–wall and fluid–fluid forces, can lead to interesting surface-driven phase changes. These include new kinds of phase transitions not found in the bulk phase, e.g. layering, wetting and commensurate–incommensurate transitions, as well as shifts in transitions (e.g. freezing, gas–liquid, liquid–liquid) that are familiar from bulk behaviour. In such confined systems the confined phase is usually termed the *adsorbate*, and the porous material the *adsorbent*.

The fundamental scientific interest in these phase changes is to understand the new physics that results from finite-size effects, varying dimensionality, and surface forces. When the pore width is of the order of the range of the intermolecular forces, a large fraction of the confined molecules will experience a reduction in the number of nearest-neighbour molecules, and we might expect this to lead to large shifts in phase coexistence curves and a lowering of any critical points. These expectations are confirmed by experiment. For a slit-shaped pore (as in some carbons or in the surface force apparatus), reduction of the pore width will cause the behaviour of the confined system to change from nearly three-dimensional to two-dimensional. For a cylindrical pore (as in some zeolites and in carbon buckytubes), reduction in pore diameter will lead to one-dimensional behaviour. Thus, investigations of such confined fluids provide a way to study both finite-size effects and varying dimensionality. A fundamental question is how such transitions (and any associated critical points) are affected by state conditions and pore variables (pore geometry and size, molecular structure of the pore surface, pore connectivity, etc).

In addition to scientific interest, a fundamental understanding of these phenomena is necessary for many industrial and geophysical operations. Micro- and meso-porous (pore widths of under 2 nm and 2–50 nm, respectively) materials are widely used in the chemical, oil and gas, food and pharmaceutical industries for pollution control, mixture separation, and as catalysts and catalyst supports for chemical reactions. The design of such processes is largely empirical at the present time, with little scientific basis. Improved understanding of the effects of confinement on the equilibrium composition of reacting mixtures, and on adsorption and diffusion rates, could lead to significant improvements in these industrial processes. Confinement effects are also important for many applications in lubrication and adhesion, and in geology and geophysics. Many rock and soil formations are porous, and the flow, diffusion and selective adsorption of water, aqueous solutions, pollutants, oil and gas in soils and rocks is important in such fields as tertiary oil recovery, gas field technology, removal of pollutants from ground water and soils, and in frost heaving. Materials with very regular pores are finding application in the fabrication of nanomaterials (conducting polymers, opto-electronic devices, metal wires, etc). In these applications the nanopores are used as templates for the material fabrication, which often involves *in situ* chemical reaction and/or fluid–solid or solid–solid phase changes.

Some examples of nanoporous materials are given in table 1, together with approximate pore shapes and sizes. It is convenient to divide these into those with crystalline or regular structures, and those that are amorphous. For crystalline (e.g. aluminosilicates, aluminophosphates) or regular (e.g. carbon buckytubes) materials, x-ray or neutron diffraction can be employed to determine the atomic structures, and hence the pore geometry and dimensions. Such information provides the coordinates of the solid atoms, and this structural information greatly facilitates the interpretation of experiments carried out on these materials. In addition, modelling of confinement effects in such materials is greatly simplified. Even in these materials some structural uncertainties usually remain. The location of water molecules and ions in the framework structure may be unknown. *Ab initio* calculations, and in some

Table 1. Nanoporous materials. Data taken, in part, from [167].

Material	Surface	Pore shape	Pore width (nm)
A. Crystalline, regular			
Aluminosilicates	O, Al, Si	Cylinder, cage	0.3–1.0
Aluminophosphate	O, Al, P	Cylinder	0.8–1.3
MCM-41	O, Al, Si	Cylinder	1.5–10
Carbon nanotube	C	Cylinder	2–10
B. Amorphous			
Porous glass	O, Si	Cylinder	$4–1 \times 10^4$
Silicas, oxides	O, Si, etc	Cylinder	1.0 up
Silica aerogel	O, Si	Void	5–50
Pillared clay	O, Si, Al	Slit + pillars	>0.5
Microporous BN	B, N, H	Slit	<1
Activated C fibre	C	Slit	0.6–1.3
Activated C aerogel	C	Slit + void	1.5–30

cases classical simulations, can help in determining the likely location of such molecules. In addition, defects in the lattice or pore structure can sometimes lead to large effects on adsorption, particularly if the pore structure consists of straight cylindrical pores that are not interconnected (as in some aluminosilicates and many aluminophosphates). In such cases, a very small percentage of lattice defects can block large amounts of pore volume. At the present time the small pore zeolites, conventional aluminosilicates and aluminophosphates [237], can be prepared in a highly crystalline form. The larger pore materials, MCM-41 [19] and carbon nanotubes [71] are difficult to prepare in a pure and completely uniform state. MCM-41 (Mobil Catalyst Material 41; figure 1) is a large pore aluminosilicate prepared by a liquid crystal templating process; the pore size can be controlled by varying the chain length of the liquid crystal molecules. A problem with MCM-41 is that ordered pore domains are usually very small. This situation is improved upon in a second generation of ordered mesoporous materials, prepared by a sol–gel synthesis of silicates in lyotropic liquid crystal media [7]. Such mesoporous silicas have large domains and can be extended using amphiphilic block copolymers as templates [117, 383].

Amorphous nanoporous materials vary considerably in their micro-structure and degree of regularity, and are in general very difficult to characterize completely. For example, controlled pore glass (CPG) and the related Vycor glasses [128] have pore cross sections that are approximately circular, and are thought of as having roughly cylindrical pores. They are prepared by a spinodal decomposition process that involves quenching a liquid mixture of oxides into the two-liquid-phase region; the pore size is determined by the time at which the quenched mixture is kept at an intermediate temperature, before the final quench to room temperature. Such glasses have a narrow distribution of pore sizes, and have been widely used in experimental studies. The interpretation of such experimental results has often relied on models in which the pore structure is represented by a collection of straight, cylindrical, non-connected pores having a range of diameters. However, electron micrographs of these glasses show a networked structure with winding pores (figure 2), and simple straight cylinder models of these materials do not capture some important confinement effects (see sections 3 and 5).

Silica and many porous oxides are made by sol–gel processes [155]. Silica gel is usually formed in an aqueous medium, and the solvent is subsequently removed. In the case of *xerogels*,

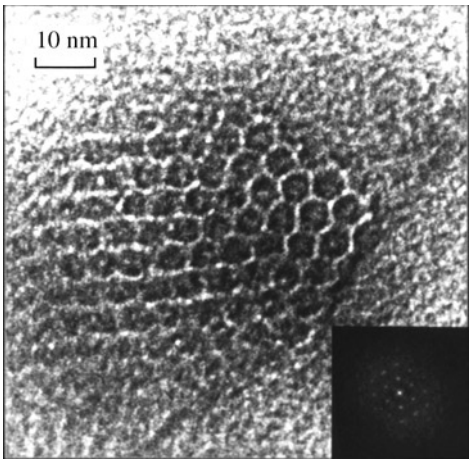

Figure 1. Transmission electron micrograph (TEM) of MCM-41, showing uniform pores of hexagonal cross section. From [149].

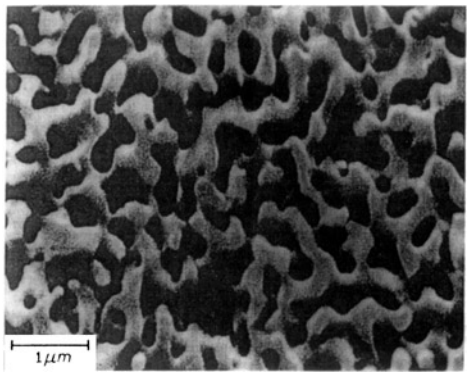

Figure 2. Scanning electron micrograph of a CPG of 300 nm mean pore diameter. From [128].

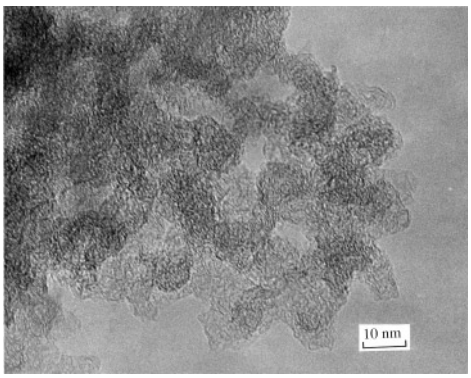

Figure 3. TEM of a carbon aerogel, magnification 2200 000. From [132].

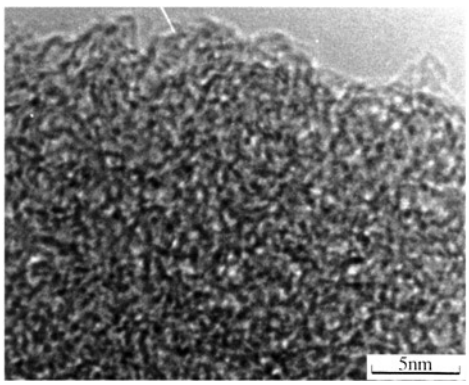

Figure 4. TEM of a pitch-based activated carbon fibre. White areas are pores, grey areas are pore walls, dark areas are thicker pore walls [271].

the structure is compressed and the porosity reduced by the surface tension forces as the liquid medium is removed. *Aerogels* are gels in which the liquid phase has been replaced by a gas in such a way as to avoid the shrinkage that would normally occur if the gel were directly dried; thus, they are characterized by very high porosity. Carbon aerogels are prepared by supercritical drying, followed by pyrolysis, of an organic gel such as resorcinol-formaldehyde gel [286,287]. They are mesoporous and may contain some micropores [131, 133]. An example is shown in figure 3. Silica aerogels [155] can be prepared by replacing the water by alcohol, heating the gel to a temperature above the critical temperature of the alcohol (to avoid the tension associated with a gas–liquid meniscus, and consequent compression of the gel), followed by removal of the alcohol vapour. Porous materials fabricated by sol–gel processes generally consist of roughly spherical solid particles separated by void space. Models consisting of a random array of spheres to represent the solid have been used to study such materials.

Activated carbons [15, 156, 233, 236, 285] can take a variety of forms (figures 4 and 5).

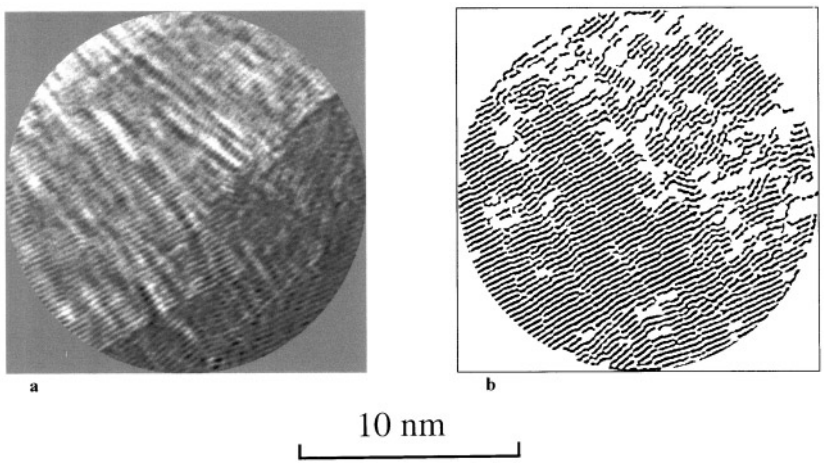

Figure 5. High-resolution TEM image before (*a*) and after (*b*) image analysis of a graphitized anthracene soot sample. From [277].

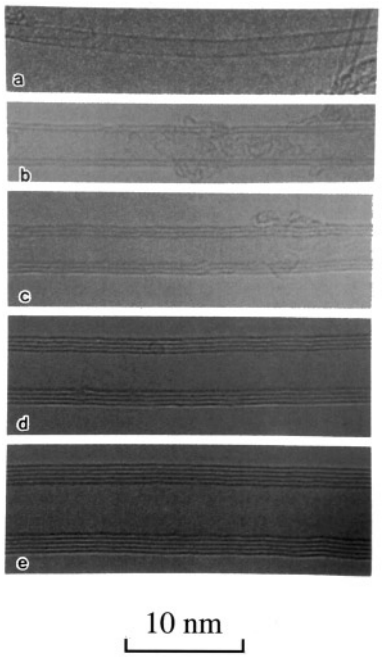

Figure 6. High-resolution TEM images of carbon nanotubes with increasing numbers of concentric tubes, one to five layers in (*a*)–(*e*). From [2].

They are usually prepared by heating organic material (e.g. wood, coal, polymers, vegetable matter) to a high temperature in the presence of an oxidizing agent (often steam). Such carbons have been modelled using a collection of slit-shaped pores of varying widths, with the pore surfaces modelled as graphite basal planes. Variations on this include wedge-shaped pores, and blocks of graphite with sections randomly removed [27, 28]. Carbon nanotubes (figure 6) can be prepared as regular straight carbon tubes; the diameter and number of graphite sheets in the walls can be controlled in the manufacturing process.

In a bulk system we can think of a first-order phase transition as being accompanied by an

infinitely sharp change in a suitable order parameter, usually the density or composition. At the equilibrium transition point the two phases have equal free energies or chemical potentials. Correlation lengths grow to infinite size as the system approaches a critical point. In a confined system, care must be used to define what is meant by a phase change. For a slit-shaped pore, true phase transitions are known to occur. The correlation length can grow to infinity in the two dimensions parallel to the pore walls, but in the third dimension, normal to the walls, it can only grow to the pore width H. Critical points will be associated with gas–liquid and liquid–liquid equilibria in such systems. For cylindrical pores the situation is more complicated. The confined system can separate into two or more phases having equal grand free energies. However, the correlation length can only grow to infinity in one dimension, that along the axis of the cylinder. Such a one-dimensional system cannot exhibit a true phase transition. Phase separation consists of the formation of small micro-domains of each phase. The average length of these micro-domains depends on the diameter of the pore and the temperature, being larger for larger pores and lower temperatures (see figure 43). As the temperature approaches a pore pseudo-critical temperature the average domain length decreases. However, away from this critical region the average domain length can be macroscopic, running to many micrometres or millimetres. In such cases it is convenient to refer to the system as phase separated, and to refer to the point at which such phase separation no longer occurs as a critical point. This is discussed further in sections 3 and 5.

Both experimental and theoretical work in this field are beset with significant difficulties. On the experimental side, it is difficult to describe the adsorbed material, and one must attempt to infer its molecular structure from a range of experimental techniques. With the exception of the crystalline materials, one of the greatest difficulties is in determining the morphology of the material. Often the distribution of pore sizes and shapes is poorly known, and little is known of connectivity and surface chemistry. In such situations any interpretation of experimental results is speculative. In equilibrium experiments it is often difficult to know if true thermodynamic equilibrium has been achieved. Metastable states are a considerably greater problem in these systems than in bulk materials. In some cases, such as freezing and liquid–liquid separation in amorphous materials, it is likely that equilibrium is never attained in any reasonable time. Other common difficulties in the experiments include: (a) the possibility that the surfaces and pore structure may change with temperature or pressure; and (b) trace amounts of impurities in the adsorbate may preferentially adsorb on the pore walls, leading to spurious results.

In theoretical and simulation work the problems are somewhat different. In contrast to the experiments, the molecular structure of the adsorbate is completely known. However, in trying to simulate amorphous systems, the lack of knowledge of the morphology of the porous material is often the greatest problem. Two possible approaches to this problem are: (i) attempt to build a model that looks as much as possible like the real material by studying electron micrographs and other laboratory measures; (ii) try to mimic by simulation the manufacturing process used to make the real material. Other complications that arise in modelling are: (a) metastable states arise frequently, as in the experiments. However, in theory and simulation we can calculate free energies, and thus determine which of several different states of the system is the true equilibrium one, and the point at which true phase equilibrium exists. (b) Usually the pore walls are assumed to be rigid and do not change with the state conditions of the bulk fluid. This requirement can be relaxed, as in clay swelling, for example: (c) vibration of solid atoms is usually neglected, but will be important for some properties. (d) The intermolecular potentials (fluid–fluid and fluid–solid) are uncertain. The fluid–fluid potentials are often assumed to be the same as those for the bulk fluid, i.e., the external field from the walls is assumed to have a negligible influence on these. In the case of the fluid–solid interactions, the importance of electrostatic, induction, and three-body and higher-body interactions is often unknown.

In addition to its use to model real systems, simulation and theory can also be used to study the behaviour of adsorbates confined in hypothetical porous materials that do not necessarily correspond to real materials. Such simulations offer the possibility of systematic investigations not possible in the laboratory, since the simulator can vary the pore geometry, connectivity and surface chemistry at will.

Earlier reviews of adsorption have addressed some aspects of phase separation in porous media [55, 78, 79, 126, 127, 325], but have not been comprehensive. In what follows we review the current state of knowledge of phase separation and phase transitions in porous materials. Our emphasis is on simple fluids (composed of small, neutral molecules) and well-characterized materials. Although we emphasize theoretical and simulation studies, we also discuss examples of experimental investigations. The most useful theoretical and simulation methods for this work are described in section 2. Subsequent sections describe various kinds of phase separations (condensation, layering transitions, liquid–liquid equilibria, and freezing). We do not cover wetting in detail, which has been reviewed separately [96, 344], nor do we discuss solid–solid transitions. Also, complex fluids, such as ionic fluids [200, 204], polymers [17, 76, 392], colloidal suspensions [177, 373] and amphiphiles, are not covered.

2. Simulation and theoretical methods

A variety of molecular simulation schemes have been used to study phase transitions in confined systems. The principal methods that have been used are grand canonical Monte Carlo (GCMC) simulation and Gibbs ensemble Monte Carlo (GEMC) simulation. Other methods that have been applied less frequently to these problems are semi-grand Monte Carlo (SGMC), histogram-reweighting and histogram-biasing methods, and molecular dynamics. A number of texts which cover these techniques in considerable depth are available, including *Computer Simulation of Liquids* [4], *Understanding Molecular Simulation* [98], and *Computer Simulation and the Statistical Mechanics of Adsorption* [260].

Among theoretical methods, the most widely used has been density functional theory (DFT) [77, 80, 126]. While integral equation theories have proved useful for investigating the structure of confined fluids [140, 178, 179], a realistic description of phase changes has proved more difficult, requiring complex closures. Here we give a brief review of simulation and density-functional techniques and their application to confined fluid phase equilibria.

2.1. Grand canonical Monte Carlo

The GCMC method simulates an open system specified by fixed temperature T, volume V and chemical potential μ. It is the staple technique for the simulation of an adsorbed fluid (or fluid mixture) in equilibrium with a bulk fluid reservoir, which is frequently the situation encountered in experimental studies of confined fluids. The method was first used in studies of bulk fluids [1, 263], and was quickly extended to adsorbed systems [365, 366].

GCMC, like other Monte Carlo methods used in molecular simulation, is based on the use of a Markov chain to generate a series of molecular configurations [134, 318] with the correct distribution of energy and density. In the grand canonical ensemble, the probability associated with any given (classical) state s of the system is

$$P(s) \propto \exp[-\beta(\mathcal{V}(s) - N\mu) - \ln N! - 3N \ln \Lambda + N \ln V], \tag{1}$$

where Λ is the de Broglie wavelength, $\beta = 1/k_B T$, $\mathcal{V}(s)$ is the total intermolecular potential energy of the system, and N is the number of molecules in the system. Most simulators use the original prescription for generating the Markov chain proposed by Norman and Filinov [4, 263].

In this method, subsequent steps in the chain are generated by modifying the current molecular configuration in one of three ways: either creating a new molecule at a random position, destroying an existing molecule, or displacing an existing molecule by a random vector. These 'moves' are then accepted or rejected according to criteria based on the temperature and chemical potential. Thermodynamic quantities of interest can be estimated by averaging their microscopic counterparts over a large number, M, of these configurations; for instance, the average internal energy $\langle U \rangle$ is estimated by the average of the instantaneous potential energy, $\frac{1}{M}\sum_i^M V(\boldsymbol{s})$. In general, there is considerable freedom in choosing the parameters controlling the simulation, and statistically efficient choices of these parameters, as well as the total simulation length, vary widely between different systems.

The thermodynamic potential appropriate to the grand canonical ensemble is the grand free energy, Ω, given by

$$\Omega = F - \mu\langle N \rangle \tag{2}$$

where F is the Helmholtz free energy, $F = U - TS$ and $\langle N \rangle$ is the average number of molecules (for a mixture the last term on the right-hand side of equation (2) is replaced by sum over all components, $\sum_\alpha \mu_\alpha \langle N_\alpha \rangle$). For a pore of general shape the exact differential of Ω is given by

$$\mathrm{d}\Omega = -S\,\mathrm{d}T - P_b\,\mathrm{d}V - \langle N \rangle\,\mathrm{d}\mu + \gamma\,\mathrm{d}A \tag{3}$$

where S is the entropy, P_b is the bulk phase pressure, γ is the solid–fluid interfacial tension and A is the surface area. For slit-shaped pores this is often written as [11, 78]

$$\mathrm{d}\Omega = -S\,\mathrm{d}T - P_b\,\mathrm{d}V - \langle N \rangle\,\mathrm{d}\mu + 2\gamma\,\mathrm{d}A - Af\,\mathrm{d}H \tag{4}$$

where A is now the surface area of one of the pore walls, H is the pore width and has been allowed to vary, and f is the solvation force (also called the solvation pressure), defined as $f = P_H - P_b$, where P_H is the pressure exerted on the pore walls by the adsorbate. From (4) the form of the Gibbs adsorption isotherm is obtained,

$$\left(\frac{\partial\Omega}{\partial\mu}\right)_{T,V,A,H} = -\langle N \rangle. \tag{5}$$

An important refinement in the use of GCMC simulations to study capillary phase equilibria was the development of an integration scheme that allowed precise location of the thermodynamic condensation pressure in mesoporous systems [290]. In this method, the grand free energy Ω is integrated along the adsorption isotherm using equation (5). The lower limit of the integration is taken as an ideal gas state, for which the grand potential can be calculated directly from the external potential [127].

The grand potential density of the desorption branch of the isotherm is determined using a three-part integration. First, a supercritical (and hence reversible) adsorption isotherm is measured. Then a second integration along a path of decreasing temperature at constant μ is done, using the expression

$$\left(\frac{\partial(\Omega/T)}{\partial(1/T)}\right)_{V,A} = U - \langle N \rangle\mu \tag{6}$$

with U the (absolute) potential energy of the system. Finally, the desorption isotherm itself is integrated using equation (5). The thermodynamic transition chemical potential is found at the intersection of the $\Omega(\mu)$ curves for the adsorption and desorption branches. These methods have been used to study liquid–vapour coexistence in both simple cylindrical models [291] and more complex models [274, 275]. For pores of irregular geometry or pore models based on an atomistic description of the adsorbent, this integration scheme is the only method so far used to calculate capillary condensation phase diagrams. We note that the thermodynamic

transition pressure cannot be determined by experiment in general, because the internal energy data required for this integration scheme is extremely difficult to obtain. We also note that, for the case of slit pore geometry, a *mechanical* route to Ω has been proposed [378].

2.2. Gibbs ensemble Monte Carlo

The GEMC method is a more recent development [279] which directly calculates phase coexistence by simulating the two phases in different simulation cells, with both mass and volume exchange between the two phases; for a pure fluid, this imposes equality of the pressure, temperature, and chemical potentials between the two phases, which implies phase coexistence. The method has also been extended to mixtures [281]. The chemical potential of each component in each phase can be calculated at no extra cost in this type of simulation [338]. Since its introduction, the Gibbs ensemble has enjoyed wide use in the study of bulk phase equilibria [280].

A Gibbs ensemble simulation is also based on a Markov chain generation; in this case, the different types of moves are displacement of molecules (in each box), transfer of molecules *between* boxes, and exchange of volume between boxes; the latter is generally accomplished by rescaling the physical dimensions of each simulation cell.

For some confined systems, this method can be used directly to obtain capillary condensation [160, 278] phase diagrams and liquid–liquid phase diagrams [119]. The system must be of a sufficiently ideal geometry that volume-scaling moves can be used; this essentially restricts one to studying smooth-walled pores of either cylindrical or planar geometry.

2.3. Semi-grand Monte Carlo

The SGMC method was developed for use in studying multicomponent phase equilibria [182]. In the case of a binary mixture, it consists of a simulation at constant $(T, N, \mu_1 - \mu_2)$, which is achieved by including simulation moves that attempt to change molecules of species '1' into molecules of species '2', and vice versa. In the constant-pressure version of the algorithm, the simulation is performed at constant $(T, P, \mu_1 - \mu_2)$. In both cases, the absolute chemical potentials of both species can be calculated using a modification of the Widom insertion method [182]. This method is especially useful for studying liquid mixtures [67] in which the quantity of main interest is the mole fraction, rather than the density.

The semi-grand method can be used for studying liquid–liquid coexistence in pore systems [106, 108]. However, if the bulk phase in equilibrium is to be specified as well, the method has little advantage over direct grand canonical ensemble simulation of the binary mixture, since the chemical potential of both species is specified in advance in the GCMC method.

2.4. Quench molecular dynamics

Molecular dynamics is a widely used technique in which the classical equations of motion for the system are integrated using a finite-difference algorithm. The resulting trajectory samples the microcanonical ensemble of states, and can be used to obtain thermodynamic averages. More important for phase equilibria calculations are the constant-temperature modifications of this method, in which the total kinetic energy of the system is adjusted, either by direct rescaling or by various schemes of coupling to an external bath of constant temperature [21, 145, 264].

Most molecular dynamics studies of phase equilibria in confined systems have focused on the kinetics of two-phase separation. In these studies a system is prepared at supercritical

temperature and then quenched into the two-phase region by resetting the thermostat in the equations of motion. The phase separation then proceeds dynamically. It can be quantitatively followed by tracking either the total potential energy of the system or measuring structural quantities such as the inter-species radial distribution function. This method has principally been used to study the separation of liquid mixtures, and has been applied in planar pores [168], two-dimensional 'strip' pores [398], cylindrical pores [106, 107, 396], and more complex disordered media [343].

2.5. Lattice models

The isomorphism between the spin-$\frac{1}{2}$ Ising model and the classical lattice gas is well known, and discussed in most standard texts on statistical mechanics [147]. The Ising model is given generally by

$$E\{s_i\} = -\sum_{\langle ij \rangle} \epsilon_{ij} s_i s_j - H \sum_{i=1}^{N} s_i, \tag{7}$$

where the first sum is taken over all pairs of spins, and the second term is the contribution of an (optional) applied magnetic field H. ϵ_{ij} is the interaction energy between each pair of spins. The Ising model has been studied in many dimensions, for many lattice geometries, and for many spatially varying external fields. Most work, however, has focused on a three-dimensional cubic lattice, with only isotropic nearest-neighbour couplings.

This simple Ising model is isomorphic with a simple model for liquid–vapour equilibria, the *lattice gas*. The lattice gas is generally given by a simple uniform lattice in which lattice sites can be occupied by a single 'gas' molecule. Gas molecules on neighbouring sites interact through some energy $-\epsilon_{lg}$. This model is made equivalent to the Ising model with nearest-neighbour interactions on the same lattice by equating occupied lattice gas sites with spin 'up' Ising sites, etc. The thermodynamic state of the lattice gas is specified by a temperature and chemical potential (μ), while the state of the Ising model is specified by a temperature and a magnetic field H; the mapping is given by $2(\epsilon\gamma - H) \leftrightarrow \mu$, with γ the coordination number of a lattice site.

In a similar way, the simple Ising model can be used to describe a coarse model for a mixture of two species. The two spin states correspond with the two species in this case. The mole fraction of the mixture is just the net magnetization, and the nearest-neighbour coupling ϵ corresponds with $\epsilon_{11} + \epsilon_{22} - 2\epsilon_{12}$, these being the nearest-neighbour couplings between isolated pairs of '1' atoms, '2' atoms, and the cross-coupling [147].

The kinetics of phase separation and domain motion in the Ising model have been extensively studied by computer simulation. Ising calculations are of the Monte Carlo type, so that there is no physically defined *time*; instead, an (arbitrary) time parameter is associated with each particular Monte Carlo simulation algorithm. Of particular interest are two algorithms; the standard spin-flip algorithm and dynamics, in which the total magnetization is not conserved, and the 'Glauber' dynamics associated with the spin-*exchange* Ising model, in which the only allowed move is the exchange of spins on neighbouring lattice sites. The spin-exchange model is suitable for studying the dynamic separation (or mixing) of liquid mixtures, although it omits hydrodynamic effects.

In this review we will hold to the usual liquids-oriented notation in describing the thermodynamics of confined systems, exept where directly concerned with spin system calculations. Those more familiar with magnetic systems might review the mappings described above in order to better reconcile these different descriptions.

2.6. Histogram analysis methods

A variety of new methods have been used in the last decade to obtain bulk phase coexistence and critical point data to very high precision. These methods are based on the collection and analysis of histograms of the energy and (usually) number of particles over the course of a Monte Carlo simulation, from which can be extracted the density of states and free energies in the system.

Histogram data were first collected some time ago, in studies of the supercritical Lennard-Jones (LJ) fluid [235]. The fact that these data could be used to efficiently estimate free energy differences was suggested by Bennett [20], after which these techniques were widely applied in analysis of spin systems and lattice models. Histogram methods were applied to phase transitions by Ferrenberg and Swendsen [87], who later determined optimal methods for the combination of data from multiple simulations [88] and uncertainty analysis [86].

Histogram methods were finally re-applied to continuous systems by Wilding and Bruce [385, 386], in conjunction with 'mixed-field' finite-size scaling analysis, which allowed the determination of the critical parameters of a LJ fluid to very high precision.

In the grand canonical ensemble, the probability of observing a state s with given $U = \mathcal{V}(s)$ and N is given in equation (1). Equivalently, the probability of observing a state with energy U and number of particles N could be written as

$$P(U, N) \propto \exp(\beta\mu N) \times \exp(-\beta U) \times W(U, N), \tag{8}$$

where $W(U, N)$ is the *microcanonical density of states* of energy U and number N. In a given (long) GCMC simulation, if we collect a histogram of the energy and number of particles, the number of 'counts' in each histogram bin will be proportional to $P(U, N)$, and so the density of states can be recovered up to a constant factor from the simulation data by dividing by the Boltzmann factor and chemical potential term. Furthermore, multiple simulations at different state points can be used to build up an accurate density of states over a large range of N and U by combining data. Ferrenberg and Swendsen [88] give an optimal statistical recipe for this combination.

The probability $P(U, N)$ can be estimated for *different* temperatures and chemical potentials, by reweighting the histogram according to

$$\frac{P_{\beta',\mu'}(U, N)}{P_{\beta,\mu}(U, N)} \propto \exp((\beta'\mu' - \beta\mu)N) \times \exp(-(\beta' - \beta)U), \tag{9}$$

which is obtained by dividing the previous expression by itself at different β and μ. This new distribution can be used to regenerate quantities such as $\langle U \rangle$ and $\langle N \rangle$, and to locate thermodynamic transitions.

The form of $P(U, N)$ near a critical point is universal up to some scaling factors. Wilding [385] showed that this property could be used to precisely locate the critical point in both finite and infinite systems.

Histogram schemes are also immediately extensible to multicomponent systems. In addition, they can be used to obtain surface tension data in both spin systems [23] and molecular simulations [148]. These methods have not yet been extensively applied in the study of confined fluids, but ought to allow for detailed and direct characterization of critical fluids in some porous materials.

2.7. Histogram-biased Monte Carlo simulations

A closely related technique, based on similar ideas, is that of histogram-*biased* simulation [22, 270]. In this family of techniques, the Monte Carlo chain itself is biased to favour certain

areas of phase space; this results in a biased probability distribution histogram, which can be *corrected* after completion of the simulation by dividing out the biasing function. The strength of this technique is that it allows distant sections of phase space (such as the solid-like and liquid-like regions) to be covered by a single series of simulations, so that transition points can be located as described above.

2.8. Density functional theory

DFT has been used extensively in theoretical treatments of confined phase equilibria and is the basis of much of our theoretical understanding of capillary phenomena [83]. In this family of methods, which are applicable to both confined and bulk systems, the equilibrium density profile $\rho(\boldsymbol{r})$ is obtained by minimizing a free-energy *functional* [77,80,126]. For the particular case of a pore system in equilibrium with a bulk phase, we write the grand potential Ω as a functional of the density profile:

$$\Omega[\rho(\boldsymbol{r})] = F[\rho(\boldsymbol{r})] - \int \mathrm{d}\boldsymbol{r}\, \rho(\boldsymbol{r})[\mu - V_{\mathrm{ext}}(\boldsymbol{r})] \tag{10}$$

where F is the intrinsic Helmholtz free energy of the fluid (i.e. the Helmholtz energy in the absence of the external field) and V_{ext} is the potential field due to the pore material. For the LJ and similar fluids, F is usually given by a first-order perturbation around the hard-sphere fluid, with the attractive part of the fluid–fluid potential interactions approximated by a mean-field term:

$$F[\rho(\boldsymbol{r})] = F_h[\rho(\boldsymbol{r})] + \tfrac{1}{2}\int \mathrm{d}\boldsymbol{r} \int \mathrm{d}\boldsymbol{r}'\, \rho(\boldsymbol{r})\rho(\boldsymbol{r}')\phi_{\mathrm{att}}(|\boldsymbol{r} - \boldsymbol{r}'|). \tag{11}$$

Generally, the attractive part of the fluid–fluid potential is taken from the Weeks–Chandler–Andersen division of the LJ potential [382]. The intrinsic free energy of the hard sphere fluid is then split into an ideal part and an excess part. The ideal part is trivial; the excess part is dealt with in one of several ways, which distinguish the several commonly used forms of the theory.

- Local density approximation. In this approximation, the excess (over the ideal gas) free energy of the hard-sphere fluid is taken to depend only on the local density, so that

$$F_h^{\mathrm{ex}}[\rho(\boldsymbol{r})] = \int \mathrm{d}\boldsymbol{r}\, \rho(\boldsymbol{r}) f_{\mathrm{ex}}(\rho(\boldsymbol{r})) \tag{12}$$

  where f_{ex} is the excess free energy per molecule of the bulk hard-sphere fluid given by some equation of state. This theory, while simple to use, does not account for even short-range correlations in the fluid, and is not able to describe the structures assumed by fluids in narrow pores.
- Tarazona's weighted density approximation. In this theory, the excess hard-sphere free energy is still written as a single integral over the density profile, but the integrated quantity is now a functional of some weighted density:

$$F_h^{\mathrm{ex}}[\rho(\boldsymbol{r})] = \int \mathrm{d}\boldsymbol{r}\, \rho(\boldsymbol{r}) f_{\mathrm{ex}}[\overline{\rho}(\boldsymbol{r})]. \tag{13}$$

  $\overline{\rho}(\boldsymbol{r})$ is a weighted average over the original density profile, with weighting functions chosen so that the theory gives a good description of the direct correlation functions of the bulk fluids. In Tarazona's theory the weighted density is an implicit function of the local density; the weighting functions themselves are functions of the weighted density. Further details and applications of this theory to various systems can be found in the original papers [348, 349].

- Kierlik and Rosinberg's weighted density approximation. This theory is formally similar to Tarazona's. The four weighting functions used here are chosen such that this theory exactly reproduces the Percus–Yevick result for the direct pair correlation function in the uniform hard-sphere fluid. In addition, these weighting functions are independent of the density, so that the calculation of the weighted density from the local density is conceptually simpler [170]. This version of DFT has been found to be somewhat more accurate in very small pores than the Tarazona recipe, and has the added advantage that it is easily and unambiguously extended to adsorbed mixtures [161, 171].

A number of papers [171, 349, 367] have extensively compared these and other theories for confined systems. There have also been applications of other liquid-state theories to confined fluids; integral equations in particular, have been found to be in excellent agreement with simulation data [178, 179], and have been used to obtain solvation forces between large particles [139, 141] and between large particles and surfaces [112].

2.9. Intermolecular potential functions

Calculated property behaviour for confined fluids is sensitive to the model used for the fluid–wall interaction. When the wall structure is included, the location of the various wall atoms must be defined in the simulation; such locations may be taken from x-ray or neutron diffraction data for the experimental material, or may be defined as part of the model in other cases. It is common to assume pairwise additivity of the intermolecular potentials; the total intermolecular interaction of a given adsorbate molecule i with the walls is then obtained by summing the pair interactions with individual wall atoms, $\sum_j u_{sf}(i, j)$, where the sum is over all wall atoms, j. In some applications it is possible to treat the walls as structureless; in this case a fluid–wall intermolecular potential is obtained by replacing the sum over fluid–wall interactions by a sum of integrals over wall atoms in a given plane. This is a reasonable approximation at higher temperatures and when the adsorbate molecule is large compared with the spacing between wall atoms. In graphitic carbons, for example, the C–C spacing between surface carbon atoms is only 1.42 Å , so that even a small molecule such as methane (diameter 3.81 Å) feels only a rather small corrugation in the fluid–solid interaction as it moves parallel to the surface. In the case of a planar graphite surface the graphite layers are separated by a uniform spacing, $\Delta = 3.35$ Å. Assuming a LJ (12, 6) potential for the fluid–wall atom interaction and integrating over the interactions with individual carbon atoms in each graphite plane, followed by summation over these planes, gives the '10, 4, 3 potential' [340, 341]

$$u_{sf}(z) = 2\pi\rho_s\epsilon_{sf}\sigma_{sf}^2\Delta\left[\frac{2}{5}\left(\frac{\sigma_{sf}}{z}\right)^{10} - \left(\frac{\sigma_{sf}}{z}\right)^4 - \left(\frac{\sigma_{sf}^4}{3\Delta(z+0.61\Delta)^3}\right)\right], \quad (14)$$

where z is the distance from the graphite surface, σ_{sf} and σ_{sf} are LJ potential parameters for the solid–fluid interaction, and $\rho_s = 0.114$ Å^{-3} is the atomic density of the solid. Here the '10' and '4' terms represent the repulsive and attractive interactions of the fluid molecule with the surface graphite plane, and the '3' term results from the summation over the remaining layers of the solid. For a slit pore, the fluid molecule will interact with both graphite walls, so that the total fluid–solid interaction will be the sum of two terms of the type given by (14), i.e. $u_{sf}(z) + u_{sf}(H - z)$.

If, in addition to integrating over each graphite plane, one integrates over all of the graphite planes in the z direction, the (9, 3) potential is obtained [341]:

$$u_{sf}(z) = \frac{2}{3}\pi\rho_s\epsilon_{sf}\sigma_{sf}^3\left[\frac{2}{15}\left(\frac{\sigma_{sf}}{z}\right)^9 - \left(\frac{\sigma_{sf}}{z}\right)^3\right]. \quad (15)$$

The (9, 3) potential is, in general, a considerably poorer approximation to the true solid–fluid interaction than the (10, 4, 3) potential, and underestimates the depth of the potential well [341]. Analogous potentials for structureless walls have been developed for pores of cylindrical geometry [294].

For low temperatures and for surfaces where the atomic spacing is not small the structureless approximation will not be appropriate. The LJ intermolecular potential has often been used as an approximate two-body potential between atoms or simple molecules. However, even for molecularly simple systems both higher-order two-body dispersion and three-body interactions have been shown to be significant, often contributing of the order 15% to the intermolecular potential energy [55, 188, 258, 261, 288]. Implicit in these commonly used potential functions for dispersion is the assumption that the polarizability is isotropic. This is not, in general a good approximation for polyatomic molecules [121] or for carbon surfaces, since the polarizability of graphite is quite anisotropic [257]. Some of the implications of this have been discussed by Nicholson [258] and Nicholson and Parsonage [260].

For many systems both direct electrostatic and induction forces between the adsorbate molecule and the surface atoms will be significant [188, 258]. For zeolites and some other materials it is necessary to account for charges on the adsorbent species, and these can lead to strong direct electrostatic and also induction forces with adsorbate molecules. Quantum mechanical calculations are helpful in determining the magnitude of partial charges to be assigned to various adsorbent atoms [384].

Although suitable functional forms for the solid–fluid intermolecular potential can be constructed, it is generally necessary to fit some parameters to experimental data. Data for the zero-coverage heat of adsorption and Henry's law constants are especially valuable in this regard, since they depend only on the adsorbate–adsorbent interaction, and are sensitive to details of this potential.

It is usual to use expressions for the fluid–fluid potential that have been developed for the bulk fluid [121, 227]. However, it should be noted that the parameters in such pair potentials have been optimized for bulk fluid properties, and such parametrizations include the effects of three-body forces. Adsorbed fluids, in contrast, are inhomogeneous, and additional kinds of three-body forces are present. For example, the 'mediated' three-body interaction involves two adsorbate molecules and a wall atom [258]. Despite these reservations, three-body dispersion interactions are unlikely to account for more than 5–10% of the total interaction, so that the uncertainties associated with these effects may not be too serious.

3. Capillary condensation

The gas–liquid transition has been extensively studied in pores, by experiment, DFT, and molecular simulation. Such a transition occurs when the temperature is below the pore critical temperature, and the pore width is greater than a few times the adsorbate molecule diameter. Such a transition appears in the adsorption isotherm (amount adsorbed versus bulk gas pressure) as a sudden and large jump in the amount adsorbed at the *capillary condensation pressure*. In a porous material in which all the pores are of the same size and shape, with homogeneous walls, such a condensation may be a sharp transition, signified by a sudden vertical jump in adsorption. In real systems, this jump is often replaced by steeply rising adsorption, i.e. continuous filling. Such behaviour can result from a distribution of pore sizes and shapes, from connectivity among pores, and from heterogeneity of the walls; in the last case, clusters of adsorbed molecules may form at strongly adsorbing centres prior to filling, and the filling may not occur as a sharp transition. Capillary condensation is usually accompanied by hysteresis. That is, desorption starting from pores that are filled with a dense fluid phase occurs via a

different path than adsorption in the pressure range where condensation occurs. Provided that the temperature is above the triple-point temperature of the bulk adsorbate, such hysteresis is usually taken to be a signature of capillary condensation. (For temperatures below the triple point, hysteresis may be due to a fluid–solid or solid–solid transition.)

3.1. Experimental studies

Although many experimental studies of capillary condensation have been reported, relatively few of these have been for well-characterized materials with a narrow pore size distribution (PSD). In this section we consider several examples of investigations where well-characterized materials have been used. Such materials have included Vycor and CPG, silica aerogels, and more recently MCM-41. The porous glasses have networked pores of roughly cylindrical shape, with pore sizes from about 4.5 nm upwards; although these materials are amorphous, the PSD is narrowly peaked about the mean pore size. MCM-41 is an aluminosilicate material having straight, non-interconnected, cylindrical pores of nearly uniform diameter. This material can have pore sizes in the range 1.5–10 nm.

Results for the adsorption of xenon in two porous materials, Vycor glass (mean pore size about 5 nm) and active carbon, are shown in figure 7 for a range of temperatures [42, 46, 265]. In both cases we observe a low-pressure region of the adsorption isotherm that is reversible, followed by a sharp increase in adsorption for a narrow range of pressures, accompanied by a hysteresis loop; the hysteresis region indicates capillary condensation. The capillary condensation pressure increases with temperature, and the hysteresis loop becomes narrower at the higher temperatures, finally disappearing at some *hysteresis critical temperature* which lies below the bulk critical temperature. The hysteresis loops arise from metastability, and so do not represent true equilibrium states; points on these irreversible sections of the adsorption isotherm generally represent a system trapped in a local minimum in the free energy. In principle, it should be possible to calculate the grand free energy for these 'gas-like' and 'liquid-like' states in the pore, and so determine the point of true thermodyamic equilibrium, using equations (5) and (6). This is difficult in practice due to the difficulty in measuring U, and does not appear to have been attempted using experimental data.

Although the broad features of the adsorption isotherms shown in figure 7 are similar for glasses and carbons, there are marked differences in the behaviour of the hysteresis loops in the two cases. In the case of the glasses these loops are more triangular in shape, and become smaller in both width and height as T is increased. For the active carbons these loops have a parallelogram shape, and while becoming narrower do not vary much in height as T is increased. These differences are believed to arise from differences in pore shape in the two cases, the glasses having roughly cylindrical pores and the carbons pores that are slit shaped.

By plotting the temperature versus the total number of moles adsorbed, n^t, at the extremes of the hysteresis loop it is possible to construct a *hysteresis phase diagram*. Such a diagram is superficially similar to what one expects for the true equilibrium 'gas–liquid' coexistence curve in the pore, but will differ from the latter since the 'gas' and 'liquid' points at a given temperature are not in true thermodynamic equilibrium. Hysteresis vanishes above the *hysteresis critical temperature*, T_{ch}. Such hysteresis phase diagrams are shown in figure 8 for CO_2 in Vycor and for Xe in active carbon. For CO_2 in Vycor the adsorption isotherms are found to be reversible for temperatures below about 193–200 K. The pore triple-point temperature is believed to lie in this range, thus providing a lower limit to capillary condensation and hysteresis. For simple fluids such as CO_2 and Xe in Vycor the pore triple-point temperature is believed to lie below the bulk value (see section 4 and figure 8). For the Xe/active carbon system the two branches of the hysteresis coexistence curve remain more widely separated than for CO_2/Vycor

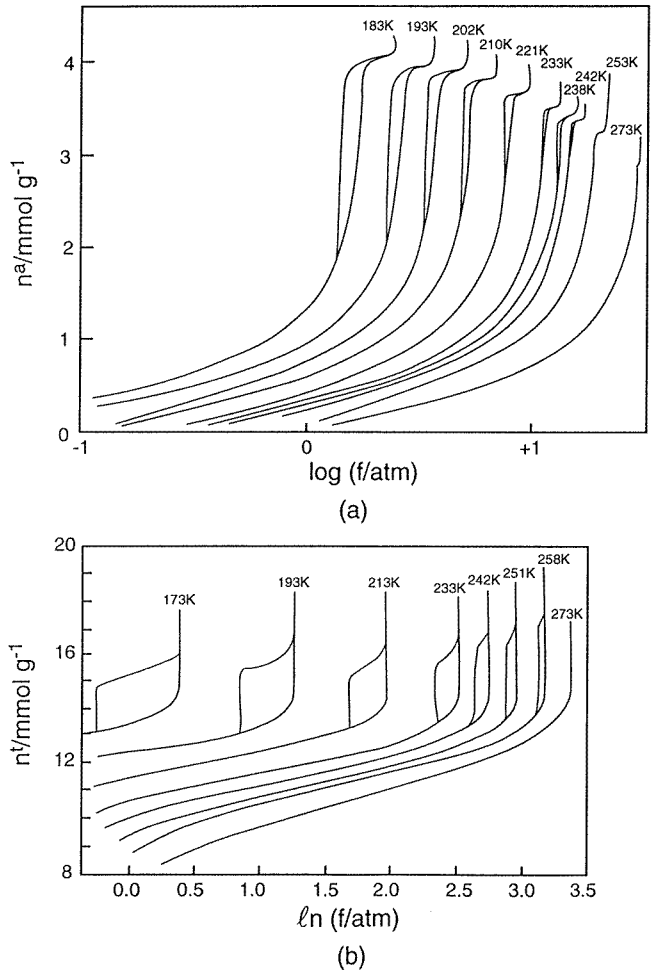

Figure 7. Adsorption isotherms for xenon, plotted as moles adsorbed per g of adsorbent versus log of fugacity of xenon in the bulk gas phase: (*a*) in Vycor glass, (*b*) in active carbon. From [46].

or Xe/Vycor until close to T_{ch}, reflecting the different shape of the hysteresis loops in the adsorption isotherms for the carbon and Vycor systems. Moreover, the top of the coexistence curve is flatter for the Xe/active carbon system than for the Vycor system. This could arise from the more nearly two-dimensional nature of the pores in the case of the carbon. The hysteresis phase diagram for Xe/Vycor is similar to that for CO_2/Vycor, and when these are plotted in reduced units as T/T_{ch} versus n^t/n^t_{ch}, where n^t_{ch} is the value of n^t at the hysteresis critical point, the two curves coincide within experimental error (figure 9). Comparison of the hysteresis phase diagram with the bulk coexistence curve can be made by converting the total moles adsorbed to the average density of fluid in the pores, ρ, as shown for CO_2/Vycor in figure 10. The coexistence curve in the pore is seen to be narrowed and the hysteresis critical point is depressed relative to that for the bulk. The considerably higher density for the 'gas' phase in the pore relative to that for the bulk is due to the adsorption of dense layers of adsorbate on the pore walls, leading to a high value of ρ on averaging over the pore cross section. The density of the 'liquid' phase is similar to that for the bulk liquid. The pore critical temperature

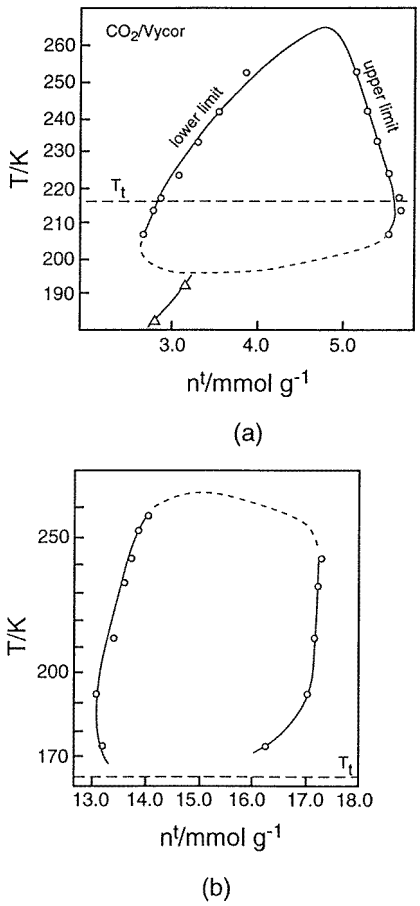

Figure 8. Hysteresis phase diagrams for (*a*) CO_2 in Vycor, (*b*) Xe in active carbon. The triple-point temperature for the bulk fluids is shown as dashed lines labelled T_t. From [46].

is expected to be lower than the bulk value, since from simple mean field theory [144]

$$T_c = c\frac{z\epsilon}{k} \tag{16}$$

where c is a constant, z is the mean coordination number for a molecule in the fluid and ϵ is the interaction energy with a nearest-neighbour molecule. For a confined adsorbate the average coordination number will be lower than for the bulk fluid, since many molecules will lie close to a pore wall, leading to a lower critical temperature.

Thommes and Findenegg [354] have reported similar measurements for SF_6 in CPGs. These materials have a narrower PSD than Vycor. The hysteresis phase diagrams are shown in figure 11 for two pore sizes. The shift in the critical temperature, $\Delta T_c = T_c - T_{ch}$, was 0.480 ± 0.23 K for CPG having a mean pore width of 31 nm, and 0.92 ± 0.24 K for a 24 nm mean pore width. Similar measurements [64] for a CPG with a mean pore size of 7.7 nm gave $\Delta T_c = 15 \pm 5$ K. The data near the pore critical region can be represented by the usual power law,

$$\rho_p^l - \rho_p^g = a(T_{ch} - T)^\beta \tag{17}$$

where ρ_p^l and ρ_p^g are the mean density in the pore for the liquid and gas phases, respectively. Fits to the data gave the critical exponent as $\beta = 0.45$ for the 24 nm CPG and $\beta = 0.53$ for

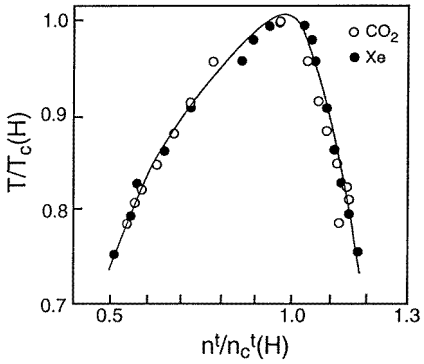

Figure 9. Comparison of hysteresis phase diagrams for CO_2/Vycor and Xe/Vycor, in reduced units. From [46].

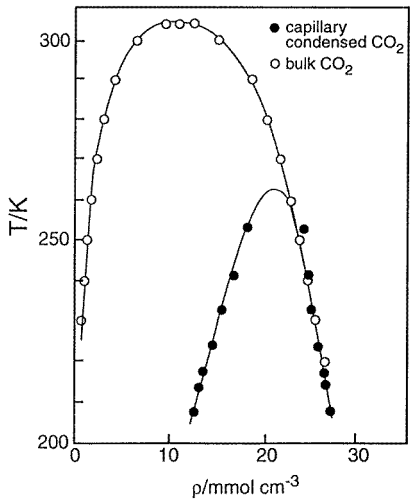

Figure 10. Comparison of hysteresis phase diagram for CO_2/Vycor with phase diagram for bulk CO_2. From [46].

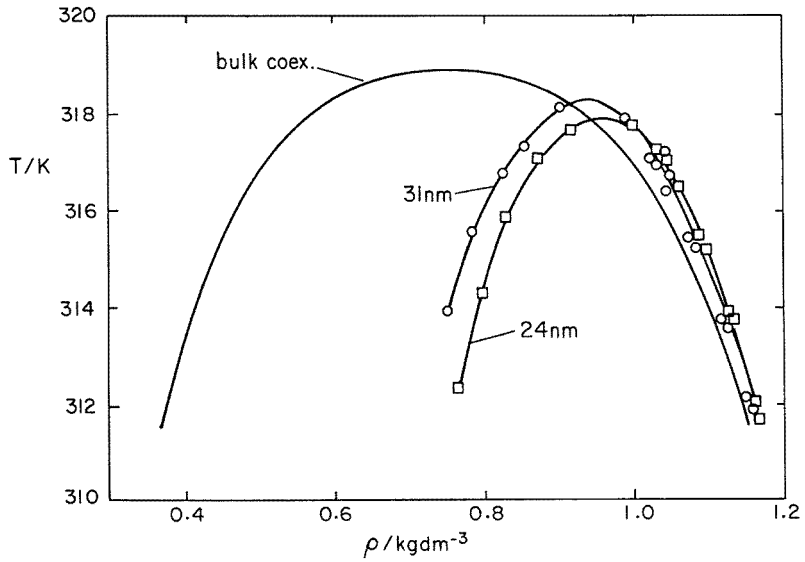

Figure 11. Vapour–liquid coexistence curve for bulk sulfur hexafluoride, and hysteresis phase diagrams for SF_6 in CPG of mean pore diameters 31 and 24 nm. From [354].

the 31 nm glass. These values are considerably larger than the Ising value of 0.33 for three-dimensional systems, and close to the classical value ($\beta = 0.5$). However, these differences from the Ising value were not regarded as necessarily significant in view of the large error bars on the density data. The shift in the hysteresis critical point was found to increase with decreasing pore width, and to be consistent with a power law of the form

$$\Delta T_c = bH^{-y} \tag{18}$$

with $y \sim 2.5$. Similar measurements have been reported by Findenegg *et al* [90] for cyclopentane, iso-pentane, perfluoropentane and SF_6 in CPG with mean pore diameters of

7.7 and 24 nm. Measurements have been reported by other workers for Vycor and silica gels having fairly narrow PSDs (e.g., [213–215, 273]).

Gross and Findenegg [123] have studied adsorption and capillary condensation of SF_6 in a mesoporous silica material having straight, non-interconnected pores, prepared by a sol–gel synthesis of silicates in lyotropic liquid crystal media [7]. This material is similar to MCM-41, but has larger ordered domains. Gross and Findenegg found a capillary phase diagram similar to that of figure 11. The lowering of the critical temperature, ΔT_c, was 20 ± 5 K, reflecting the smaller average pore diameter of about 3 nm.

Thommes *et al* [355] have also shown that adsorption is reduced at temperatures very close to, but slightly above, the bulk critical point. Starting at a temperature in the one phase region above the bulk critical point, and cooling along the critical isochore, the amount adsorbed in a CPG, at first increases as T is reduced, as expected. However, at a temperature about 1.5 K above T_c the adsorption goes through a maximum and on further lowering the temperature the adsorption is much reduced. There have been several attempts to explain this *critical depletion effect* using molecular simulation [217, 387] and theoretical methods [216, 217] for the independent slit pore model. Although an initial study based on lattice gas theory [216] did seem to show the critical depletion effect, recent molecular simulation studies [217, 387] and DFT calculations [217] show that there is no critical depletion effect for the independent slit pore model; the apparent depletion found in the lattice gas results was an artifact of that simple theory. Thus this effect remains to be explained. Apparently, it arises from effects omitted in this simple model, possibly pore geometry, connectivity or some form of heterogeneity.

The mesoporous glasses used in these studies have a networked pore structure that makes a molecular analysis of the capillary condensation results difficult (see later in this section and section 5). Mesoporous MCM-41, an aluminosilicate molecular sieve with straight, parallel cylindrical pores and with negligible pore interconnections, is a more suitable material for investigating capillary condensation. The pore diameter can be tailored within the range 2–10 nm. Recently, experimental studies of capillary condensation and hysteresis for simple adsorbates in these materials have been reported by several workers [37–39, 187, 206, 243, 246, 309, 310]. Some typical results are shown in figure 12 for argon in MCM-41 samples having two different average pore diameters. At the lower temperatures the isotherms show the sharp rise characteristic of capillary condensation, accompanied by hysteresis. As the temperature is raised the hystersis loop shrinks and vanishes at the hysteresis critical temperature T_{ch}. For these systems $T_{ch} \approx 62$ K for the smaller mean pore radius of $r_p = 1.2$ nm, and $\approx$100 K for $r_p = 2.1$ nm.

The hysteresis critical temperature T_{ch}, can be distinguished from the *pore critical temperature*, T_{cp}, defined as the temperature where the sharp jump in adsorption due to capillary condensation just disappears. While some authors have implicitly assumed that the hysteresis critical temperature coincides with the pore critical temperature, there is evidence that these two temperatures are different, with $T_{cp} > T_{ch}$. This is plausible on theoretical grounds, since it is known that for straight unconnected pores, as in MCM-41, the hysteresis results from the system being trapped in a local minimum in the free energy. On adsorption, for example, this local free-energy minimum would correspond to the gas-like state, and the system may remain in this state at pressures somewhat above the true thermodynamic transition pressure. However, we might expect that as the temperature is raised this local minimum well in the free energy either disappears or becomes too small to hold the system in the gas-like state (fluctuations in such small systems can be large). In this situation, hysteresis would disappear somewhat below the pore critical temperature. Morishige and Shikimi [246] have estimated T_{cp} for argon in siliceous MCM-41 by measuring how the slope of the adsorption isotherm in the capillary condensation region varies with temperature. In a perfectly monodisperse material, in which

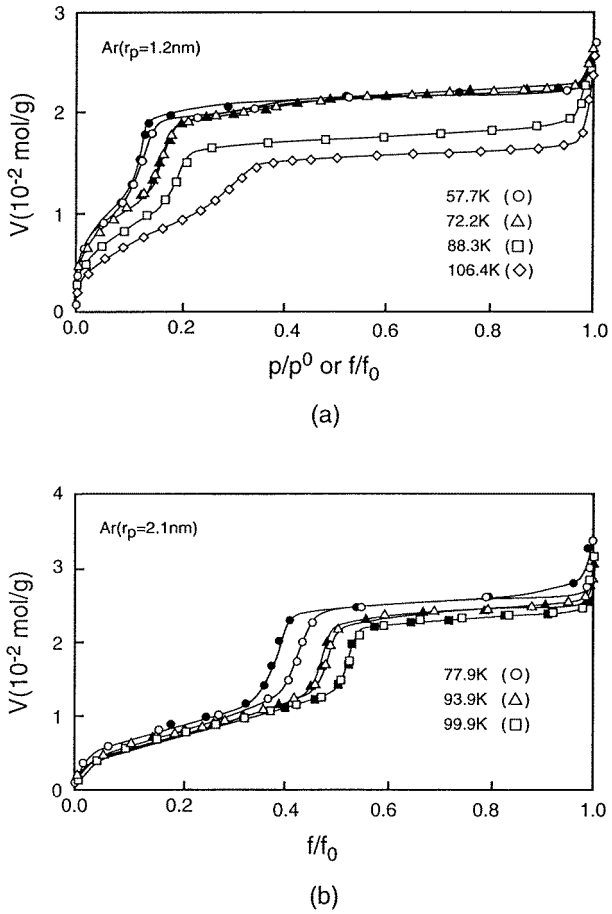

Figure 12. Adsorption isotherms for argon in siliceous MCM-41 at various temperatures for two mean pore radii: (*a*) $r_p = 1.2$ nm, (*b*) 2.1 nm. Adsorption points are shown as open circles, desorption as filled circles. In (*a*) the isotherms at the two lower temperatures, 57.7 and 72.2 K, are plotted against reduced pressure, while the others are plotted versus reduced fugacity. The triple-point temperature of bulk argon is 83.8 K. From [246].

all pores are of the same diameter, surface structure and composition, capillary condensation should result in a sharp vertical jump in V, the adsorption; thus, the slopes $(\partial \ln P/\partial V)_T$ or $(\partial \ln f/\partial V)_T$ should be zero. By plotting the experimentally determined values of the slope $(\partial \ln P/\partial V)_T$ or $(\partial \ln f/\partial V)_T$ against temperature [253] it is possible to make a rough estimate of T_{cp}, as shown in figure 13 for argon. In the temperature range where capillary condensation occurs these derivatives are positive but small; their non-zero values arise from the distribution of pore sizes in the real material. For temperatures up to about to about 98 K the derivative increases slowly, but above this temperature, it increases more rapidly with T. Such a rapid increase is expected when T is above the pore critical temperature. Morishige and Shikimi interpret the intersection of these two straight line regions as being the pore critical temperature, $T_{cp} \simeq 98$ K. If this interpretation is correct, then T_{cp} is significantly larger than T_{ch}, which for this system is approximately 62 K. Both of these temperatures are substantially below the bulk fluid critical temperature of argon, which is 150.7 K, as expected for such

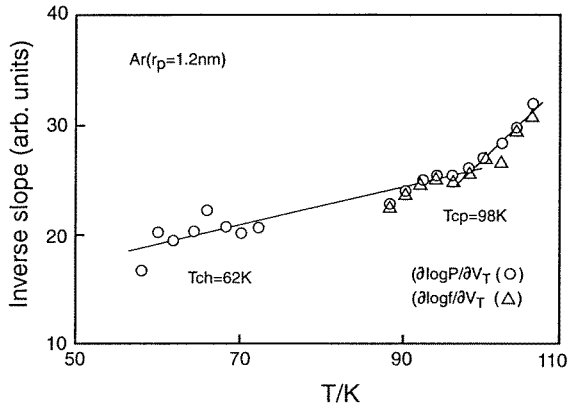

Figure 13. Effect of temperature on the inverse slope of the adsorption isotherm at the point of capillary condensation, for argon in siliceous MCM-41 with a mean pore radius of 1.2 nm. The inverse slope at higher pressures is estimated on the basis of both $(\partial \log P/\partial V)_T$ and $(\partial \log f/\partial V)_T$. From [246].

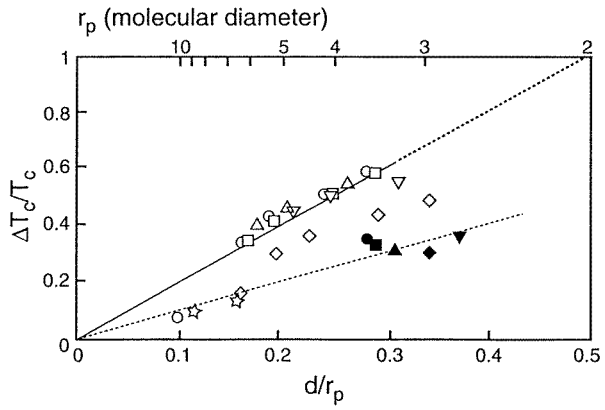

Figure 14. Shifts in the hysteresis and pore critical temperatures, $(T_c - T_{ch})/T_c$ and $(T_c - T_{cp})/T_c$, vs reduced inverse pore radius, for various adsorbates in mesopores: Ar (○), N_2 (△), O_2 (□), C_2H_4 (▽), CO_2 (↓) and Xe (∗). Open and closed points represent T_{ch} and T_{cp}, respectively. The four open points at smaller values of d/r_p, which lie well below the line for the hysteresis critical temperature of MCM-41, are results for T_{ch} for networked mesoporous adsorbents, Vycor [46] and silica gel [214]. Lines are guides for the eye. From [246].

small pores. Morishige and Shikimi have estimated pore critical temperatures for other gases, including N_2, O_2, CO_2 and C_2H_4, in this material, and find that $T_{cp} > T_{ch}$ in each case, the difference being of the order 40–60%.

A dimensionless plot of the shift in the both the hysteresis and pore critical temperatures against the inverse pore radius is shown in figure 14 for several adsorbates. According to simple theories of adsorption [83] such a plot should be linear, and the results agree with this prediction within experimental error. The results for $(T_c - T_{ch})/T_c$ versus d/r_p, where d is the diameter of the adsorbate molecule, for Ar, N_2, O_2 and C_2H_4 fall on a single straight line passing through the origin; the data for CO_2 and for C_2H_4 at $r_p = 1.4$ nm deviate from this relationship. The shifts in the pore critical temperature are smaller than those for the hysteresis critical temperature. Also included in figure 14 are four points for $(T_c - T_{ch})/T_c$

versus d/r_p for the networked porous materials Vycor and silica gel. The shift in hysteresis critical temperature for these materials is considerably smaller than for the straight cylindrical pores of MCM-41. Such a result might be expected, since in MCM-41 as the pore critical point is approached the molecular correlation length can grow only to the pore diameter in the radial direction normal to the pore axis. In networked materials, on the other hand, we expect the correlation length to be able to grow to larger values, on average, so that the depression of the pore critical point would be less.

A few studies have been reported for silica aerogels. In particular, Chan and colleagues [389, 390] have studied the liquid–vapour transition for ^{4}He and for nitrogen in a silica aerogel having a porosity of 95%, using heat capacity measurements in the case of ^{4}He and light scattering in the case of N_2. In spite of the disordered nature of the void spaces, sharp transitions were seen, with a pore critical temperature that is somewhat below the bulk value. They found that the coexistence curves were much narrower than those for the bulk fluid. They were able to determine the critical exponent of equation (16), and found it to be $\beta = 0.280 \pm 0.05$ for ^{4}He and $\beta = 0.350 \pm 0.05$ for nitrogen. These values are consistent with that found for bulk fluids ($\beta = 0.33$), but not with the random-field Ising model [66], for which a value of β close to zero is expected.

In principle, carbon nanotubes also offer an attractive material for fundamental studies of capillary condensation, since the pores are straight, non-interconnected cylinders with monodisperse pore size. So far adsorption studies have been limited due to several problems, including difficulty in obtaining the nanotubes in a sufficiently pure form and strong adsorption on the outer surfaces [102].

3.2. Theoretical and simulation studies: simple pore geometries

There have been many studies of fluids confined in pores of simple geometry over the last decade. Here we define 'simple geometry' to mean pores of some simple and regular shape, usually slit-like or cylindrical, although some studies have been reported for pores of spherical shape. Furthermore, our definition implies that the surfaces are homogeneous (fluid interactions with the wall are the same for different regions of the wall), the pores are not interconnected, and are independent in the sense that the adsorbate molecules in a given pore are unaware of the existence of those in neighbouring pores; the pores all have the same geometry, although they can differ in pore width.

3.2.1. Macroscopic thermodynamic treatment. For sufficiently large pores it is possible to use a macroscopic treatment of capillary condensation. For such pores, oscillations in the density profile due to the fluid–wall forces can be ignored, and the grand free energy can be written as the sum of a bulk and a surface term, $\Omega = -PV + 2\gamma A$, as follows from integration of equation (3) using Euler's theorem (here we have implicitly assumed a slit geometry, and the area A is that of one of the pore walls). By writing equations for the grand free energy of the confined gas-like and liquid-like phases, assuming that the liquid wets the walls completely (contact angle is zero), and equating the grand free energies it is possible to derive an equation for the pressure P at which capillary condensation occurs [82, 83, 122]:

$$\ln\left(\frac{P}{P_0}\right) = -\frac{2\gamma_{lg}}{RT\rho_l H} \tag{19}$$

where P_0 is the saturated vapour pressure of the bulk fluid, γ_{lg} is the gas–liquid surface tension for the bulk fluid, R is the gas constant, and ρ_l is the density of the bulk liquid. This equation, called the Kelvin equation after its originator, should be valid for large pores and

for temperatures well below the pore critical temperature. Its derivation is based on several assumptions: density oscillations due to the walls can be neglected, the system is large enough that a surface tension can be defined [357], the gas phase can be treated as an ideal gas, the liquid phase is incompressible, and the surface tension can be taken to be the value for the bulk fluid at this temperature.

Because the Kelvin equation fails to account for the strong adsorbed layers on the pore walls, it is common to modify equation (16) by replacing the true pore width H by some modified pore width which accounts for the adsorbed layers that form prior to capillary condensation. Usually this is done by replacing H by $H - 2t$, where t is the thickness of the adsorbed layer on the wall. A systematic treatment of the influence of wetting on corrections to the Kelvin equation was carried out by Derjaguin [65]. He showed that H should be replaced by $H - 2t$ only when the solid–fluid forces are exponential or of finite range; when dispersion forces are present and wetting films develop H should be replaced by $H - 3t$; see the discussion by [81, 83]. In practice, this thickness is usually estimated from an adsorption isotherm (or 't-curve') for the adsorbate fluid on a non-porous surface of the same chemical type as the porous material. In addition, the Kelvin equation can be modified to account for nonideality of the gas phase, liquid compressibility, and non-zero contact angle.

An estimate of the range of applicability of equation (18) can be obtained by determining the capillary condensation pressure for suitable model fluid/pore systems, using either DFT or molecular simulation, and comparing the result with the prediction of the Kelvin equation or its modified form. Such comparisons for simple models of nitrogen in carbon slit pores indicate that the Kelvin equation becomes inaccurate for pore sizes below about 7.5 nm [378]. This estimated lower bound to the pore width below which the Kelvin equation breaks down will depend on the temperature and the material. Nevertheless, the figure of 7.5 nm is in good general agreement with an estimate of Fisher and Israelachvili [93], which was based on experimental observations of cyclohexane between mica surfaces in the surface force apparatus. They concluded that the Kelvin equation broke down for separations H below 8.0 nm (16 molecular diameters). These estimates are for cases where the liquid completely wets the surface. When the contact is non-zero (partial wetting) the Kelvin equation may remain accurate to somewhat smaller pore widths [349]. The Kelvin equation, and its modified forms, overestimates the capillary condensation pressure for a given pore size; conversely, it underestimates the pore width corresponding to a given capillary condensation pressure. These errors become large for small pores, as shown in figure 15 [197]. The modified Kelvin equation is seen to be in significant error even for pores of 4–5 nm. For pores of $H = 2$ nm, use of the modified Kelvin equation to predict the pore size from a known capillary condensation pressure is in error by a factor of about 2 for these model carbons. Errors of this magnitude have also been shown to occur when this equation is applied to realistic models of porous silica glasses [110]. The non-local form of DFT is in very good agreement with the simulation results shown in figure 15. Local DFT (not shown) gives capillary condensation pressures that are somewhat too low [195]. Comparisons of the modified Kelvin equation, and other semi-empirical approaches, with molecular simulation have also been made for straight cylindrical pores [197]. The results are similar to those shown in figure 15.

3.2.2. Microscopic treatment: theory and molecular simulation for pure fluids. Work up to 1990 has been reviewed by Evans [79], and most of what follows focuses on more recent work. Such studies have often included investigations on heats of adsorption, structure of the adsorbent, and in some cases solvation forces, as well as capillary condensation. They differ in (a) the method used, (b) the pore geometry (primarily slit or cylinder), and (c) the use of a structured versus a structureless wall. The methods used have included DFT, lattice gas model

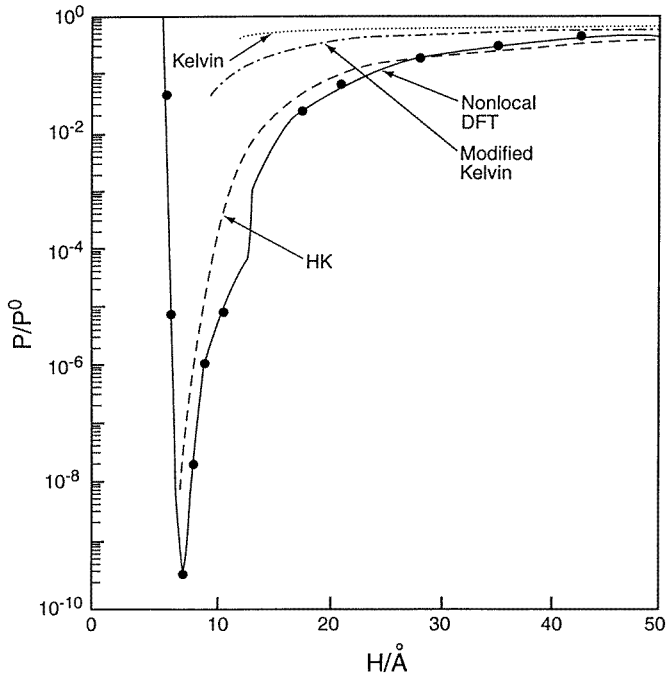

Figure 15. Pore filling pressures versus pore width from the Kelvin and modified Kelvin equations, the Horvath–Kawazoe equation (HK), DFT and molecular simulation (points) for a simple model of nitrogen adsorption in a slit carbon pore at 77 K. Here H is defined as the distance between the planes passing through the centres of the carbon atoms making up the first layer of each wall. The DFT and simulation results show capillary condensation for the larger pores, with continuous filling at some smaller pore widths. The sharp increase in the curve for $H <\sim 7$ is due to the molecular sieving effect. From [197].

calculations [44, 230], integral equation theory [140, 178, 179], and molecular simulation. These different methods have been found to give similar results for capillary condensation.

In the case of pores of slit geometry with the walls lying in the xy plane, the molecular correlation length, ξ, can grow to infinity in the x and y directions, although its growth is limited to H in the z direction normal to the walls. True phase transitions are possible in such a geometry, and capillary criticality will correspond to the two-dimensional Ising universality class [79]. Fisher and Nakanishi [94] used scaling arguments to show that for large pores the decrease in the critical temperature in the pore should obey

$$\Delta T_c = (T_c - T_{cp})/T_c \propto H^{-1/\nu} \qquad \text{(large } H\text{)} \tag{20}$$

where ν is the critical exponent for the correlation length, and takes the value 0.63 for bulk three-dimensional fluids. For small pores [79]

$$\Delta T_c \propto H^{-1} \qquad \text{(small } H\text{)}. \tag{21}$$

Since the criticality is of the two-dimensional Ising class, we expect the jump in adsorption, Γ, due to capillary condensation to vanish as $\Gamma \propto (T_{cp} - T)^{\beta}$, with $\beta = \frac{1}{8}$ rather than the bulk three-dimensional value of $\beta = 0.32$. Even for very strongly attractive adsorbents, such as carbon, molecular simulations [160] suggest that β is very close to the unperturbed two-dimensional value of $\frac{1}{8}$.

Numerous studies of adsorption behaviour and capillary condensation in slit pores have been reported [10, 11, 58, 79, 83, 162, 195–197, 230, 254, 259, 283, 311, 312, 325, 328, 376, 378].

Calculations of adsorption isotherms for a given pore size bear a qualitative resemblance to those found experimentally. For mesopores and sub-critical temperatures, as the pressure is increased layers of adsorbate molecules first form on the walls of the pores, leading to an initially rapid increase in adsorption. At higher pressures there is a sudden, discontinuous jump in adsorption, corresponding to the capillary condensation transition [378]. Following the transition, the pores are filled with a nearly incompressible liquid-like phase, and little further increase in adsorption is observed on further increasing the pressure. Starting from such filled pores and decreasing the pressure, capillary evaporation is delayed and occurs at a lower pressure than that observed for condensation. Such hysteresis effects are due to metastability. The system becomes trapped in a local minimum in the free energy, and remains in the metastable state until the pressure has changed sufficiently that the local minimum disappears or becomes small enough that a small fluctuation in the density is sufficient for the system to change to the state representing a deeper minimum in the free energy [294]. If such calculations are repeated at higher temperatures the capillary condensation moves to higher pressures and the hysteresis loops decrease in size, until they eventually disappear [83, 84]. This adsorption behaviour is similar to that shown by the experimental systems in figure 7, except that since the pores are monodisperse in these model systems the jumps in adsorption corresponding to capillary condensation are sharp discontinuities. In addition, the shape of the hysteresis loops in the model calculations are somewhat different to those observed in the experiments, being usually more rectangular in form. In the simulations it is possible to determine the true thermodynamic transition condition by using equations (4) and (5), and the integration scheme described in section 2.1 [290, 291]. In general, the true phase transition pressure lies between the adsorption and desorption curves.

For a given adsorbate/adsorbent system at a fixed subcritical temperature, the capillary condensation pressure is reduced as the pore width H gets smaller. This is illustrated for a simple model of nitrogen in a graphitic carbon having slit pores in figure 16. The capillary critical temperature also decreases as the pore width gets smaller. For sufficiently narrow pores the sharp capillary condensation transition no longer occurs, and is replaced by a steep but continuous filling. In the example shown in figure 16 this occurs for a pore width H^* between 3.75 and 4.00. This phenomenon is due to the fact that the pore critical temperature lies somewhat below 77 K for the pore of width 3.75, but is above 77 K for $H^* = 4.0$. Thus, the pore width below which continuous filling occurs will depend on the temperature.

From figure 16 it can be noted that the capillary condensation pressure is very sensitive to the pore width. This observation is the basis of commonly used methods for measurement of the PSD for porous materials [122]. The usual procedure is to assume the pore structure of the material can be represented as a collection of non-interconnected pores all of which have the same geometry (e.g. slit or cylinder) and surface structure, but which can differ in pore width H, so that the total adsorption Γ can be represented by

$$\Gamma = \int \rho(P, H) f(H)\, \mathrm{d}H \tag{22}$$

where $\rho(P, H)$ is the mean density of fluid in the pore of width H at pressure P, $f(H)$ is the PSD, and the integration is carried out over all possible values of the pore width. In early approaches to determination of the PSD, the Kelvin equation or a modified form of it was used to determine the relation between capillary condensation pressure and pore size [122]. In such methods the pore width H in equation (16) is replaced by $(H - nt)$, where t is the thickness of the adsorbed film on the wall and n is 2 or 3, depending on the particular method used [81]. The film thickness is usually estimated empirically from an adsorption isotherm for a nonporous sample of the material of interest. Such methods are known to give pore sizes that are too small for pore widths below 7–10 nm (see figure 15), and more accurate theories for the prediction of

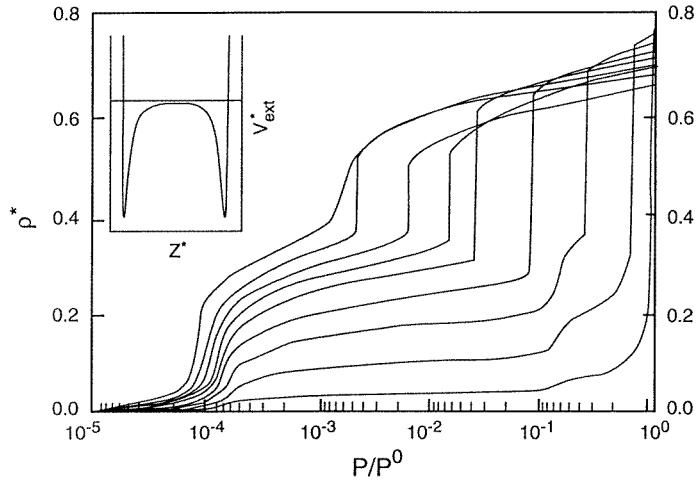

Figure 16. Adsorption isotherms for a LJ model of nitrogen in slit-shaped graphitic carbon pores with 10, 4, 3 walls at 77 K, from the Tarazona form of DFT. Reading from left to right, the pore widths are $H^* = H/\sigma$ =3.75, 4.0, 4.25, 4.5, 5, 6, 8, 14 and 40, where σ is the LJ diameter of the N_2 molecule. The inset shows the characteristic solid–fluid potential profile for a mesoporous slit. From [195].

$\rho(P, H)$ have been proposed. Thus, Seaton *et al* [331] used local DFT to predict this quantity, while later workers have used either non-local DFT [157,195–197,255,266–269,301,311,320] or molecular simulation. An example of the application of these methods to determine the PSD of an activated carbon, CXV, is shown in figure 17; the pores are assumed to be slit shaped. The use of DFT results in a great improvement in the accuracy of prediction of the adsorption $\rho(P, H)$ for various pore sizes in equation (21). Moreover, DFT is accurate for pores of any size, in contrast to the Kelvin-based and other semi-empirical methods, and provides a good prediction of the entire isotherm (not just the condensation pressure). The principal problems remaining in such PSD determinations result from the oversimplification represented by equation (21). In addition, it is usually necessary to use some assumed mathematical form for the PSD given by $f(H)$ in (21); however, this is not believed to be a major problem provided that the function assumed for this is sufficiently flexible (e.g. it allows for multiple peaks of widely varying width).

Using DFT or molecular simulation, it is possible to explore the effects of system variables on the adsorption behaviour in a systematic manner. For example, Balbuena and Gubbins [10–12] have used the Tarazona form of DFT to study the effects of varying temperature, pressure, pore width, and the LJ intermolecular force ratios σ_{sf}/σ_{ff} and $\epsilon_{sf}/\epsilon_{ff}$, where sf and ff refer to solid–fluid and fluid–fluid interactions, respectively, for adsorption into slit pores. They determine the ranges of these variables for which the adsorption behaviour is found to be in each of the classes of the IUPAC classification shown in figure 18. Classes IV and V are of interest here, since the hysteresis loops are a signature of capillary condensation. The step-wise adsorption shown in class VI indicates adsorption by layers; that is, adsorption proceeds by completing a given layer before starting the next layer. Such layering transitions are discussed in section 4.

An example of the results of this classification of adsorption behaviour is shown in figure 19, which is for the case when the ratio $\sigma_{sf}/\sigma_{ff} = 0.9462$; this ratio corresponds to the adsorption of methane on graphite, for which $\epsilon_{sf}/\epsilon_{ff} = 0.435$. In this figure a class VII

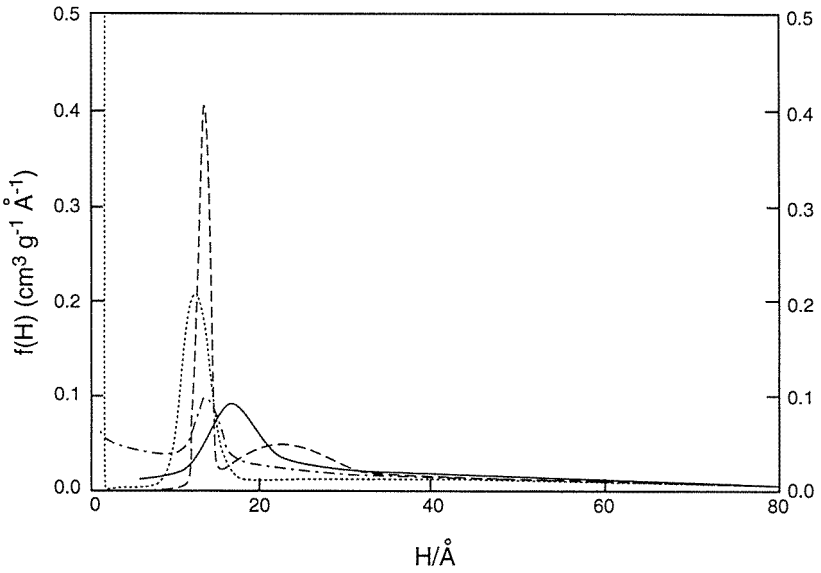

Figure 17. PSD for an activated carbon, CXV, based on inversion of equation (22) using nitrogen adsorption data at 77 K over the reduced pressure range $P/P_0 = 0$ to 1: solid curve, Tarazona non-local DFT; dashed curve, local DFT; dotted curve, Kelvin equation; dash-dotted curve, modified Kelvin equation. From [195].

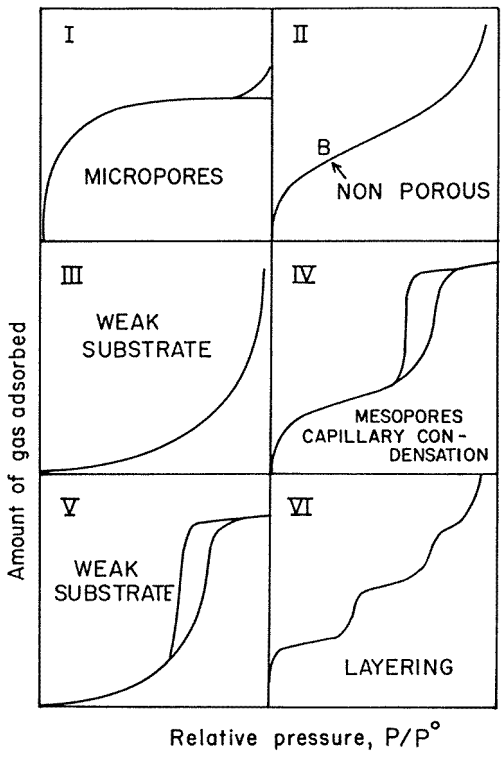

Figure 18. The six types of adsorption isotherm according to the 1985 IUPAC classification. From [333].

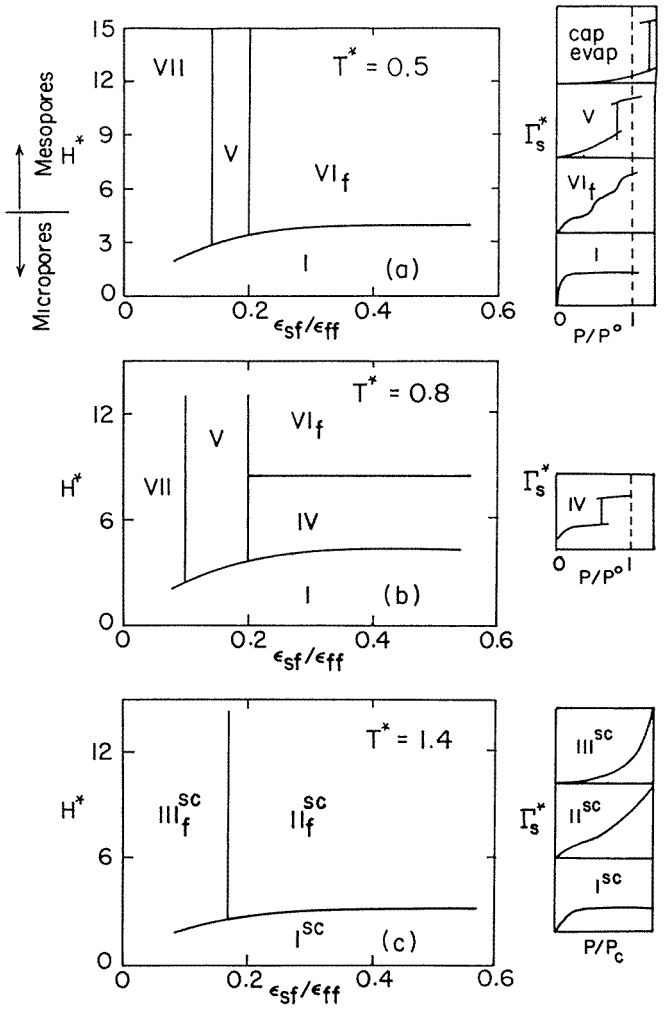

Figure 19. Classification of adsorption isotherms for slit pores for $\sigma_{sf}/\sigma_{ff} = 0.9462$: (*a*) $T^* = kT/\epsilon = 0.5$; (*b*) $T^* = 0.8$; (*c*) $T^* = 1.4$, from DFT. The lines in the figure are approximate and refer to qualitative changes in the adsorption behaviour. Subscript f means 'finite', i.e. the adsorption remains finite as $P \to P_0$ (T is below the wetting temperature). Superscript sc means 'supercritical' (T is above the pore critical temperature). From [11].

has been added to the empirical classification of figure 18; class VII is similar to V, but because the solid–fluid interaction is very weak compared with the fluid–fluid one, and the temperature is relatively high, condensation does not occur until $P/P_0 > 1$, i.e., the pressure is greater than the bulk vapour pressure, a phenomenon referred to as *capillary evaporation*. Subscript f on the classes in figure 19 indicates that the adsorption remains finite at $P/P_0 = 1$, in contrast to adsorption on single surfaces above the wetting temperature. As with the adsorption results, it is possible to classify capillary condensation (and layering transition) behaviour in terms of these independent variables [10, 11]. An example of these results is shown in figure 20. A similar classification of adsorption and capillary condensation behaviour has been made for pores of cylindrical geometry [12].

Turning from slit to cylindrical pores, we can recognize two main differences. First,

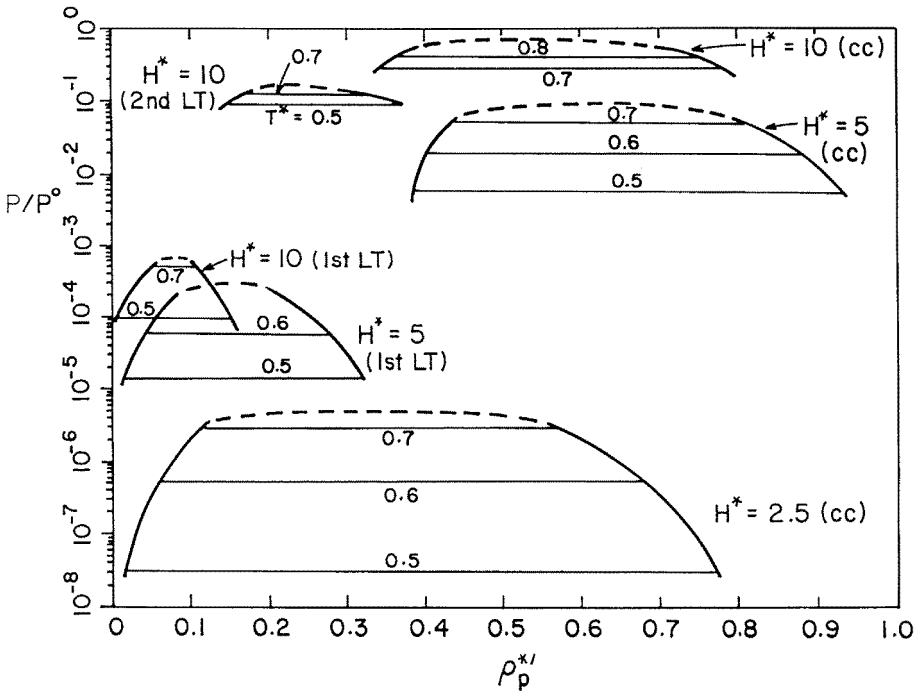

Figure 20. Phase coexistence envelopes for capillary condensation (cc) and first (first LT) and second (second LT) layering transitions for potential parameters corresponding to the methane/carbon system from DFT. Results for pore widths $H^* = 2.5$, 5.0 and 10.0 are shown. Dashed curves are a rough estimate of the pore critical region. The abscissa is the reduced density in the pore, $\rho_p^{*\prime} = \rho_p' \sigma_{ff}^3$, where ρ_p' is the number density excluding the dead space (thickness $0.7\sigma_{ff}$) near the walls. From [11].

because the fluid is now confined in two dimensions rather than one, the confinement effects are greater. Thus, we observe capillary condensation at lower pressures, and the lowering of the critical temperature is greater than for slit pores of the same width. Second, for narrow cylindrical pores the system approaches a one-dimensional system, and so cannot exhibit true phase transitions at temperatures above 0 K. Any first-order phase transition in a cylinder must be rounded by finite-size effects [300]. A rough estimate for the effect of rounding on the chemical potential shows [78, 79] that the change in μ scales as $\exp[-(R/\sigma)^2]$, where R is the radius of the cylinder and σ is the diameter of the confined fluid molecule. Thus, even for $(R/\sigma) = 2.5$ the rounding is small, and the capillary condensation transition appears sharp in both simulations and DFT calculations [83, 291]. A second consequence of these finite-size effects is that, because of the finite surface area of the gas–liquid interface in a cylinder, we do not observe single domains of 'gas' and 'liquid' phase in the cylinder, but rather a series of alternating domains of each phase [300]. The average length of these domains depends on the specific system, the pore diameter and the temperature, becoming shorter for small diameter pores and for temperatures approaching the pore critical value. Such alternating domains have been observed in simulations of long cylindrical pores for both capillary condensation [138] and liquid–liquid equilibria [106]. Typical results for the average domain length are shown in figure 43; it is seen that, except near the pore critical temperature, the average domain length is quite large, often thousands of nanometres or more, so that it is reasonable to talk of these domains as microphases.

Numerous studies of capillary condensation have been reported for straight cylindrical pores [12, 14, 83, 137, 138, 283, 290, 291, 293, 294, 302, 376]. For a given pore diameter the intermolecular potential experienced by an adsorbate molecule due to the walls has a deeper well than for a slit of the same width, so that capillary condensation occurs at lower pressures. In addition, the mean density of adsorbate in the filled pore is generally lower for cylinders, a result of packing considerations [12]. Of particular interest is the approach to one-dimensional behaviour in narrow cylinders [291, 302].

Pores of other regular geometries have been studied, including spheres [118, 391] as an approximate model of some zeolite cavities, and pores of square [33] and triangular [35] cross-section.

The hysteresis associated with capillary condensation has been studied by several methods. Early studies were carried out by mean field DFT and GCMC simulations [83,84,294] for both slit and cylindrical pores. As the chemical potential (bulk gas pressure) is gradually increased the adsorbed phase remains in the gas-like state for some distance beyond the point of true thermodynamic transition. This is because the system remains in a local minimum in the grand free energy that corresponds to the gas-like state; only when the barrier separating this local minimum from the global one becomes very small does the system exhibit condensation [294]. A similar phenomenon occurs on desorption, with the system persisting in the liquid state at chemical potentials (pressures) below the true equilibrium value. Such metastability is similar to that found in bulk liquids in the gas–liquid coexistence region, but is more pronounced in confined systems. However, neither DFT nor GCMC calculations allow the presence of both gas-like and liquid phases simultaneously, so that it is not possible to observe the influence of a meniscus. This problem is not present in molecular dynamics or canonical Monte Carlo, where the phase change can be effected by changing the overall density of the confined fluid. Molecular dynamics calculations [138] have been used to observe the interface between the coexisting phases, and its influence on hysteresis, for cylindrical pores of infinite length. Calculations for pores having open ends, using both a lattice gas model and canonical Monte Carlo simulations, allow the formation and disappearance of menisci at the open end of the pore, and have shown [230, 283] that this effect has a large influence on the width of the hysteresis loops. Open-ended tubes of finite length also result in end effects (the net adsorbate-wall interaction is reduced near the tube ends) that can significantly reduce the width of the hysteresis loop [224]. Additional effects that influence hysteresis, due to pore networking and tortuosity, are discussed in section 3.2.3.

For the most part, the studies described above have been of a general nature. However, several attempts have been made to model capillary condensation in simple geometries for specific systems, and in some cases to make direct comparison with experiment. Examples include investigations of krypton [254], nitrogen [259], methane [162, 312] and water [362] in graphitic carbons; argon and nitrogen in MCM-41 [222, 254, 311]; argon in an alumina-pillared clay [56]; and argon and nitrogen in carbon buckytubes [224]. Using a lattice gas model, Cole *et al* [54] have studied condensation of ^{4}He in carbon nanotube bundles.

3.2.3. Microscopic treatment: theory and molecular simulation for mixtures. Several studies have been made for simple mixtures in cylindrical [135, 136, 347] and slit [57, 58, 161, 346] pores. The total adsorption isotherms display capillary condensation at pressures that are usually below the bulk vapour pressure for the mixture, as for pure fluids. The essential new feature for mixtures is the change in composition due to confinement. Results for a model of an argon(1)/krypton(2) mixture in a cylindrical carbon dioxide pore [136] are shown in figure 21. The LJ model was used for the fluid–fluid and fluid–solid interactions, and the solid was treated as a structureless continuum. The results for $R^* = \infty$ show the gas–liquid

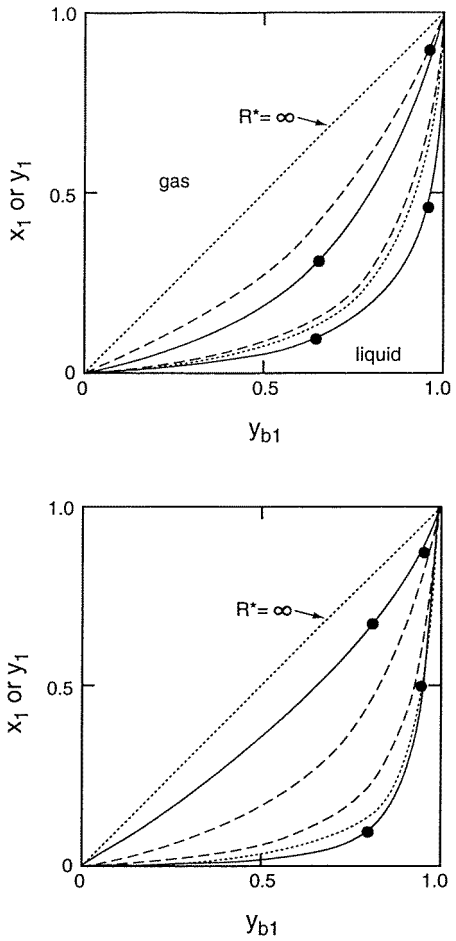

Figure 21. Mole fractions for coexisting gas (y_1) and liquid (x_1) phases for a LJ model of argon(1)/krypton(2) mixtures in a cylindrical CO_2 pore. The upper figure is for a pore of radius $R^* = R/\sigma_1 = 5$ at $T^* = kT/\epsilon_1 = 0.7$, and the lower one is for $R^* = 2.5$, $T^* = 0.6$. The horizontal axis is the mole fraction of argon in the bulk gas phase, y_{b1}, that coexists with the pore. The dotted ($R^* = \infty$, bulk system) and dashed curves denote local mean field results, while the filled circles and the solid lines drawn through them are molecular dynamics simulation results for the pore. Mole fractions are averaged over the pore width; in the case of the bulk system, x_1 and y_1 denote x_{b1} and y_{b1}. From [136].

coexistence for the bulk mixture, as predicted by the local form of DFT. The confined mixture shows a marked increase in the krypton mole fraction for the gas phase, a result of the stronger attraction of krypton to the walls. This effect is much smaller for the confined liquid phase, so that the difference in composition for the confined gas and liquid phases is much smaller than for the corresponding bulk phases. Agreement between the local DFT and molecular simulation results is only qualitative, since the local theory fails to describe the strong density oscillations of the adsorbate near the walls.

The change in composition of the confined phase is often expressed as a selectivity, S, defined by

$$S_2 = \frac{x_{p2}/x_{pl}}{y_{b2}/y_{bl}} \tag{23}$$

where x_{pi} is the average mole fraction of component i in the pore and y_{bi} is the corresponding mole fraction of i in the coexisting bulk phase. Results for the selectivity for ethane for a LJ model mixture of methane(1) and ethane(2) in a slit carbon pore with (10, 4, 3) walls are shown in figure 22. Calculations were based on an extension to mixtures [347] of the Tarazona form of DFT. For the larger pore sizes shown the temperature chosen lies above the pore critical temperature, T_{cp}, but is below T_{cp} for the smaller pore widths. The vertical jump in S at

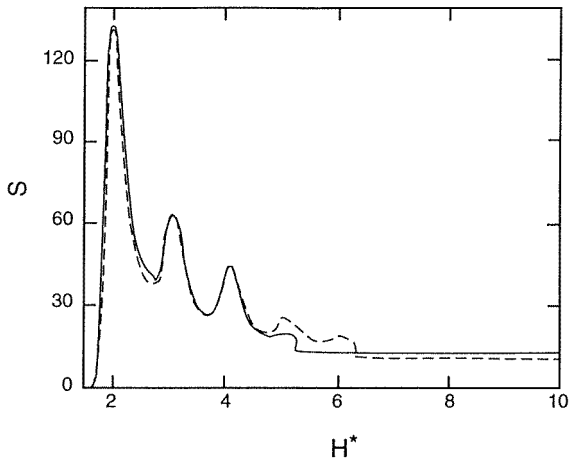

Figure 22. Selectivity for ethane versus pore width, $H^* = H/\sigma_{11}$, for methane(1)/ethane(2) mixtures in a slit carbon pore, at $T^* = kT/\epsilon_{11} = 1.5$, $y_{b1} = 0.5$. Results are shown for two pressures, $P^* = P\sigma_{11}^3/\epsilon_{11} = 0.1$ (solid curve) and 0.2 (dashed curve). Vertical jumps are due to capillary condensation. From [346].

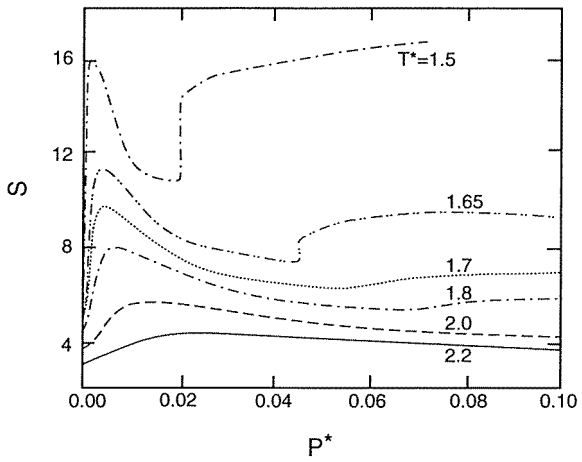

Figure 23. Selectivity isotherms for the same system as in figure 22, for $H^* = 8$ and $y_{b1} = 0.5$, for a range of temperatures. From [346].

$H = H_{cc}$ indicates the capillary condensation transition. For $H < H_{cc}$ the pore is filled with a liquid-like phase, while for $H > H_{cc}$ it is filled with a gas-like phase. The strong oscillations in S, as H is varied when the pore is filled with liquid results from the layered structure of the adsorbed phase; as H is decreased sudden changes in the average density occur at particular pore widths where a whole layer of molecules is squeezed out of the pore.

The effects of temperature and pressure on the selectivity for this system are shown in figure 23. The vertical jumps in selectivity at the lower temperature results from capillary condensation. As a result of these and similar calculations, Tan and Gubbins [346] have proposed the classification of selectivity isotherms shown in figure 24. Class I is found at temperatures well above T_{cp}. The increase in S at low pressure results from the stronger fluid–fluid attraction between ethane molecules relative to methane. Class II corresponds to temperatures slightly above T_{cp}. A second maximum in S appears as the result of a buildup of multiple adsorbed layers, a precursor to capillary condensation. Class III occurs at temperatures somewhat below T_{cp}, and exhibits capillary condensation. For temperatures well below T_{cp}, layering transitions can occur in addition to capillary condensation, leading to selectivity isotherms of class IV.

Cracknell *et al* [57] have also carried out GCMC simulations of the adsorption of

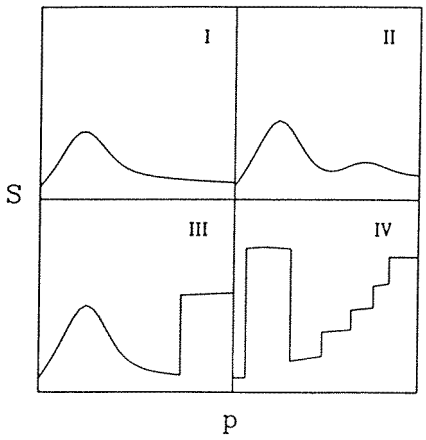

Figure 24. Classification of selectivity isotherms for mixtures in pores. From [346].

methane/ethane mixtures in graphitic slit pores. Their simulations were in qualitative, rather than quantitative, agreement with the DFT results of figures 22 and 23.

3.3. Theoretical and simulation studies: complex pore geometries

While of intrinsic scientific interest, the results for idealized pore geometries described in the previous section are not easily related to experimental results for real materials. In particular, they omit several complicating factors such as various kinds of pore heterogeneity. Among these factors are inter-pore correlation effects, surface chemical heterogeneity, variations in pore geometry, networking of pores, etc. Recent work has moved to address some of these factors, although direct comparisons with experimental data for amorphous materials are still fraught with difficulty.

3.3.1. Pore–pore correlation effects. For materials with closely spaced pores, inter-pore adsorbate interactions might have a significant effect on phase changes. In particular, for sufficiently narrow cylindrical pores the adsorbate molecules should form a one-dimensional system for a single pore. Molecular simulations and theoretical calculations [291, 302] have shown near one-dimensional behaviour in such single pores, and as expected, no phase transition occurs for $T > 0$ K. Some aluminophosphates and aluminosilicates have nearly cylindrical pores so that for appropriately sized adsorbates we expect no transition. However, in cases where the pores are closely spaced we might anticipate that pore–pore correlations would lead to a transition of the gas–liquid type at low temperatures. Such a transition has been observed using molecular simulations by Radhakrishnan and Gubbins [302] for a LJ model of methane in an array of cylindrical pores whose diameter was chosen to be that of $AlPO_4$-5, an aluminophosphate whose pores have a diameter which is just sufficient to accommodate a line of such methane molecules. When the pores are placed close together in a hexagonal array a phase transition was observed from a gas-like to a liquid-like phase at temperatures below about 52 K. This phase change occurs below the temperature at which the correlation length grows to about the inter-pore separation distance. Such pore–pore correlation effects are expected to be larger for strongly dipolar fluids, such as water, ammonia and methyl fluoride, and the resulting phase separation should occur at higher temperatures and be more easily observed for such systems.

Saravanan and Auerbach [322] have used lattice GCMC simulations to show that a

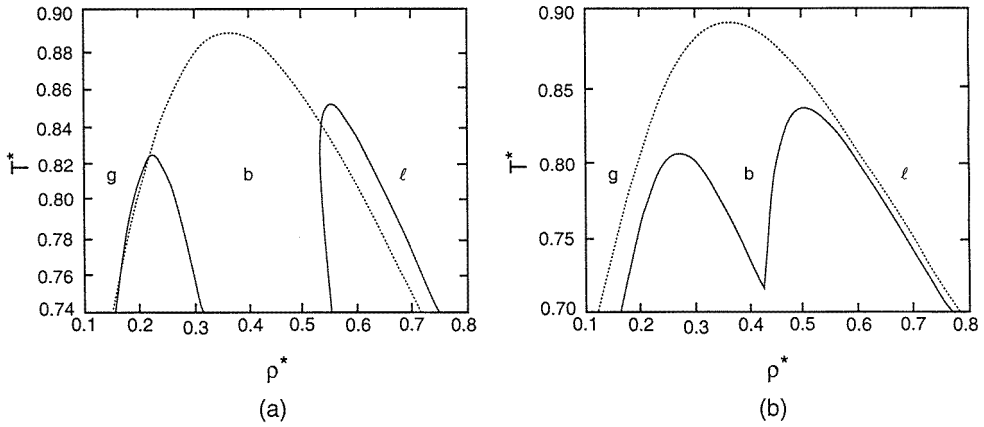

Figure 25. Temperature–density phase diagram for slit pore of width $H = 5\sigma$ with chemically heterogeneous walls consisting of alternating strips of strongly and weakly attractive regions (see text for details). Solid curves denote phase diagram for the heterogeneous walls, dotted curves are for smooth homogeneous walls with potential $V_0(z)$: (*a*) $d = 20\sigma$; (*b*) $d = 11\sigma$. Here d is the corrugation period for the heterogeneous walls; g, b and l denote 'gas', 'bridging' and 'liquid' phases, respectively. From [314].

transition from a gas-like to a liquid-like phase occurs for benzene in Na–X zeolite due to adsorbate–adsorbate correlations between neighbouring cages of the zeolite. This transition occurs at ambient temperatures, and is consistent with NMR results for this system. Cole *et al* [54], using the quantum lattice gas approach, have recently shown that condensation occurs for ^{4}He adsorbed into the interstitial channels within a bundle of carbon nanotubes due to pore–pore correlation effects between ^{4}He atoms in neighbouring channels. They predict a highly anisotropic quasi-one-dimensional condensed phase having a pore critical temperature of about 0.3 K.

3.3.2. Chemically heterogeneous surfaces. Most studies of the influence of chemical heterogeneity have been for slit-shaped pores, and these can be divided into two types. In the first, the pore surface is divided into strips of strongly and weakly attractive regions [32, 51, 314, 315, 326, 327, 372]. In the second, individual chemical groups are attached to the planar surface [224, 234, 247–249, 360, 369, 370, 372, 374]. For the case of chemically striped surfaces, the behaviour depends strongly on the ratio d/H, where d is the width of the stripe and H is the pore width. For individual groups on the surface the corresponding variable is n/H, where n is the site density on the surface. When d/H or n/H are sufficiently small the behaviour is qualitatively similar to that for homogeneous walls, since the effects of surface heterogeneity are not felt far from the walls. When d/H or n/H are large the behaviour is similar to that of a collection of independent pores of various widths or fluid–adsorbate interactions. Intermediate cases between these two extremes are of particular interest. In addition to these studies for slit pores, Segarra and Glandt [332] have studied a model of water on activated carbons in which the carbon is modelled as made up of randomly oriented platelets of graphite with a dipole distributed uniformly over the edge of the platelets to mimic the activation.

Striped surfaces have been investigated using mean field Ising lattice models [32,315], non-local DFT [51, 314] and GCMC simulation [327, 328, 372]. Although the interaction models are somewhat different in these various cases, the resulting phase diagrams are qualitatively

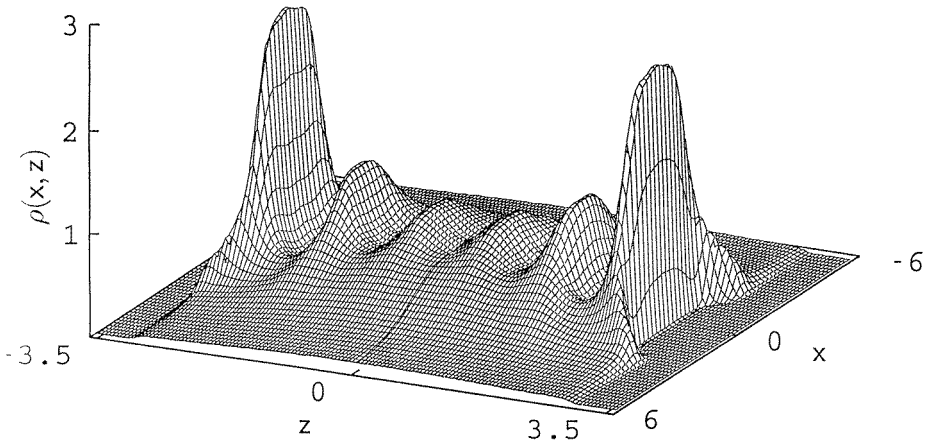

Figure 26. Density profile for a 'bridge' state for a slit pore of width $H = 7.2\sigma$ at $T^* = kT/\epsilon = 1.00$, $\mu^* = \mu/\epsilon = -11.50$, from GCMC simulations. The strongly attractive wall strip lies between $x = -2\sigma$ and $+2\sigma$. From [32].

similar. Typical results for a slit pore of width $H = 5\sigma$ (where σ is the diameter of the adsorbate molecule) for two intermediate values of d/H are shown in figure 25. For these cases the fluid–wall potential was periodic in the x direction, and of the form

$$V(\boldsymbol{r}) = V_0(z) + A(z)\cos(2\pi x/d) \tag{24}$$

where $V_0(z)$ is the mean strength of the potential, z is the direction normal to the walls, d is the period of the fluid–solid potential corrugation, and V_0 and A are given by Yukawa potentials. For $d = 20\sigma$ two coexistence regions are seen, each with its own critical point. At the lower densities, the coexistence is between a gas-like state (g) and a state (b) in which liquid 'bridges' have formed between the strongly attractive regions of the surfaces of the two walls of the pore; successive bridges of liquid are separated by gas-like regions that cover the less strongly attractive wall areas. At the higher densities there is a coexistence between the 'bridge' state and a state in which the pore is filled with a liquid-like phase (l). Such behaviour is expected when d/H is relatively large. For the smaller value, $d = 11\sigma$, these two coexistence regions merge at the lower temperatures, where coexistence is between the gas and liquid phases, but remain separated at higher temperatures. These two temperature regions are divided by a triple point, at which all three phases (g, b, l) are in coexistence. On further reducing the value of d, the triple-point temperature increases, and the triple point disappears at a value between $d = 8\sigma$ and 9σ. Typical density profiles for the bridge state are shown in figure 26, taken from the work of [32]. These results are obtained from GCMC simulations for a wall model in which the fluid–solid interaction is the LJ model, and consists of strips of strongly attractive (s) and weakly attractive (w) regions. The strongly attractive strips are of width $d_s = 4\sigma$, while the weakly attractive strips have a width $d_w = 8\sigma$.

Surfaces with individual chemical groups have been studied by lattice gas models [360]. GCMC simulations have been reported for water [224, 234, 247, 248], methane [372] and for associating chain molecules [249, 369, 370] adsorbed on model activated carbons composed of slit pores in which the surfaces are decorated with chemical groups. In the case of water and associating chains, these groups can hydrogen bond to the adsorbate molecules. For water it is found that if the site density is low enough the adsorption is similar to that in graphitic pores [248, 362]. That is, almost no adsorption occurs at low to moderate relative pressures,

but this is followed by capillary condensation. As the surface density of sites increases more adsorption occurs at low pressures, and the pore filling moves to lower pressures. At these higher site densities the pore filling ceases to be via a sharp phase transition, and occurs continuously. Examination of snapshots of the adsorption at increasing pressures shows that water molecules first adsorb singly on the surface sites, and these adsorbed molecules form adsorption sites for further water molecules to hydrogen bond to. Thus water clusters are formed around surface sites, and these grow until eventually they link up with other clusters on the same wall, or with clusters on the opposing wall in narrow pores. This filling mechanism is quite different to that for simple fluids on homogeneous pore walls, where the filling occurs a layer at a time followed by capillary condensation.

3.3.3. Geometric heterogeneity. Geometric heterogeneity can take a variety of forms. For example, the effects of surface irregularities in the pore walls, networking and interconnections among pores of the same or different size and geometry, and disordered pore structures such as those in aerogels are all of interest.

Surface irregularity. Adsorption in slit pores in which the surfaces have a step (raised region), and in which the steps are in registry for the two walls, have been studied using the non-local DFT of Tarazona by Chmiel *et al* [51]. The behaviour is dependent on the lengths of the step compared with the remainder of the surface, and on the step height relative to the pore width H, but is in many respects similar to that for the chemically striped surfaces considered in section 3.3.2. When the step height is appreciable compared with the pore width two capillary condensation transitions occur at a particular temperature, the one at lower pressures corresponding to the formation of a 'bridge' phase in which a liquid-like layer forms in the narrower part of the pore, and the one at higher pressure corresponding to the pore being filled with a liquid-like phase (cf figures 25 and 26). Related studies for stepped surfaces have been reported by Tovbin and Votyakov [360] using lattice-gas theory. Maddox and co-workers [221, 223] have studied the case of two narrow slit pores, open at one end to a bulk gas phase, and separated by a larger pore. The behaviour in this case depends strongly on the relative widths of the two pores. Curry *et al* [61] studied a slit pore in which each of the walls had a fcc(100) structure, and one of the walls was smooth while the other had a stepped surface; depending on the registry of the two walls, the confined phase may be fluid or solid. While adsorption on single walls composed of randomly packed spheres (the Bernal model) has been studied [47], there does not seem to have been a systematic study for pores for this model. Vishnyakov *et al* [372] have studied capillary condensation for methane in slit pore models of coal in which the surfaces are geometrically structured.

Networked structures. So far we have considered only materials in which the pores are independent, each connected through their open end to the bulk fluid phase with which they are in equilibrium. In such systems the adsorbate molecules in a given pore are usually unaware of the existence of adsorbate in neighbouring pores. However, most amorphous porous materials have pores that are interconnected; moreover the pores may be tortuous and of varying size. It has long been suspected that such connectivity of pores and size variation may have an important effect on the adsorption behaviour, and particularly on capillary condensation. Thus, pores of larger width may be connected to the bulk phase only through narrower pores or necks; in such cases, once the pore structure is filled with a liquid-like phase, it will be difficult for such larger pores to empty since molecules must diffuse through the liquid-like phase that still fills the smaller pore regions ('pore blocking'). In addition, near pore connection points, as the

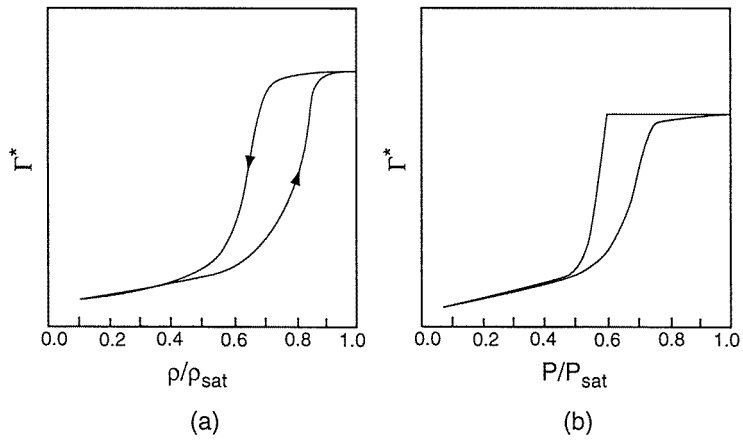

Figure 27. Adsorption isotherms for xenon in Vycor glass, calculated from (*a*) the independent single-pore model, (*b*) the network model of Mason, at $T = 0.63T_c$, where T_c is the bulk critical temperature of xenon. From [14].

pore critical point is approached by raising the temperature the correlation length can grow to lengths greater than the pore width, and this could have a significant effect on the location of the pore critical point. Possible evidence for this is seen in figure 14, where the lowering of the pore critical temperature for simple adsorbates in Vycor and silica gel, which have networked pores, is smaller than for MCM-41, which has straight pores which are not interconnected.

The effects of networking on the adsorption of simple fluids in Vycor and CPGs have been considered by several authors. Ball and Evans [14] used local DFT to study the adsorption of xenon in Vycor glass for two models: (a) a collection of independent single cylindrical pores, each open to the bulk phase, and (b) an interconnected network of such pores. Yukawa potentials were used for the intermolecular interactions, and the PSD was assumed to be given by a Gaussian distribution, with parameters appropriate for Vycor. In order to account for networking in model (b) Ball and Evans used a theory due to Mason [231, 232], in which pores are interconnected via 'windows' or necks. Application of Mason's model requires knowledge or assumption of the distribution of pore and neck sizes, and the connectivity C, defined as the average number of necks connected to a given pore. In Mason's model adsorption is assumed to be unhindered, but desorption cannot occur until the pressure falls to a value where the menisci can pass through the necks. This pressure is calculated using the local DFT, and C is taken to be 4. Mason's model leads to hysteresis due to pore blocking, even when adsorption is reversible in a single pore. Typical results from these independent pore and network models are shown in figure 27. The two models give noticeably different shapes for the hysteresis loops, the network model giving a sharper drop in adsorption, as is observed in the experiments (see figure 7(*a*)). The horizontal region at high pressure and the sharp 'knee' in the desorption curve are artifacts of the network model. The temperature dependence of these isotherms show that the size of the hysteresis loops decreases with increasing temperature, disappearing at the highest temperature studied, $T/T_c = 0.94$, for both models, in agreement with experiment. In the case of the network model the width of the loops remains constant up to $T/T_c = 0.87$ in contrast to the experimental findings; again this is an artifact of the network model.

A more realistic model of Vycor and CPG glasses has been developed by Gelb and Gubbins [109] by mimicking the spinodal decomposition manufacturing process for these glasses using quench molecular dynamics simulation. Such glasses are prepared by heating a

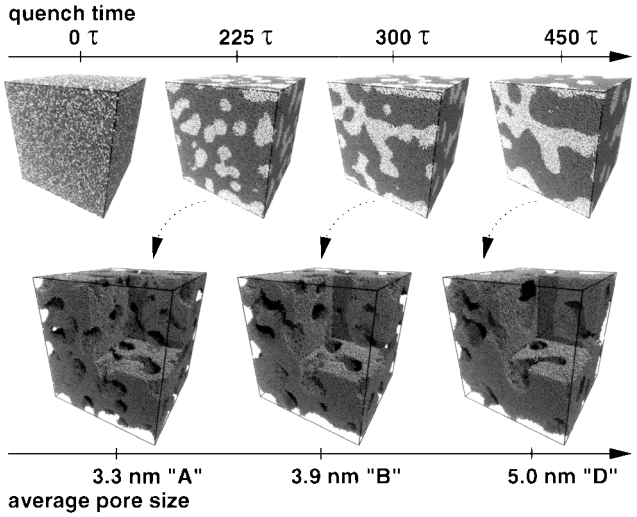

Figure 28. Preparation of model porous glasses. Quench molecular dynamic simulations for a binary mixture (top) produce a networked structure. Snapshots taken at later stages in the phase separation are made into porous samples (bottom, shown in cutaway view) by removing one of the phases. Pore size increases with time after quench. Simulation time is given in reduced units τ (τ is equivalent to 0.781 ps). From [110].

suitable mixture of oxides (typically 62.7% SiO_2, 26.9% B_2O_3, 6.6% Na_2O and 3.5% Al_2O_3 in the case of Vycor) to about 1200 °C, where it forms a homogeneous liquid mixture, and then quenching it to an intermediate temperature of about 700 °C, where it phase separates on a microscopic scale into two continuous phases, one rich in silica and the other rich in the other oxides. The mixed oxide phase forms a network structure of winding cylinders, whose diameter grows with time. By controlling the time at this intermediate temperature it is possible to control the diameter of the cylinders. When the desired diameter is reached the mixture is quenched to room temperature and the mixed-oxide phase is removed by treatment with a hot acid solution, leaving a porous glass that is 96% silica. This phase separation process is relatively insensitive to the intermolecular potentials used. Gelb and Gubbins use a symmetric LJ binary mixture in which the like pair interactions are the same for the two species, i.e. $\epsilon_{11} = \epsilon_{22} = \epsilon$ and $\sigma_{11} = \sigma_{22} = \sigma$, but the unlike pair attraction is weak, $\epsilon_{12} = 0.25\epsilon$ ($\sigma_{12} = \sigma$). Such a mixture has a liquid–liquid coexistence region which is symmetrical, with the critical mixing composition at $x_1 = 0.5$. Provided that the composition is not very dilute in one of the components, quenching this mixture into the spinodal region leads to phase splitting to produce locally tubular phases whose diameter grow with time. Following the quench, one phase can be removed and the resulting porous structure relaxed or annealed. Pore size is controlled by varying the length of the quench period; porosity can be controlled by varying the initial composition. Such simulated glass structures closely resemble those obtained experimentally in appearance, surface area, connectivity and porosity. Snapshots of this procedure for preparing model porous glasses are shown in figure 28 for several stages of the quench process; here $\tau = (\epsilon/m\sigma^2)^{0.5}t$ is the reduced time, and corresponds to 0.781 ps. In these simulations the sides of the simulation box were each 27 nm in length, and the cell contained 868 000 atoms initially with a mole fraction of $X = 0.7$, so that the porosity of the glasses formed was close to 30%. The pore volume in these glasses is fully connected.

Porous glasses generated in this way are precisely characterized, since we know the

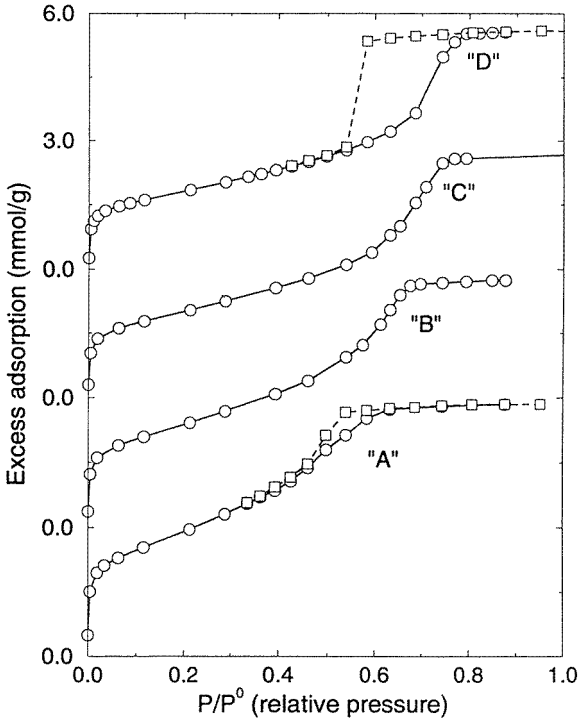

Figure 29. Adsorption isotherms for a model of nitrogen in the model glasses depicted in figure 28, at 77 K. Adsorption data are shown as circles; desorption data, shown only for the A and D glass samples, are shown as squares. The isotherms are vertically displaced for clarity, and lines are a guide to the eye. Uncertainties in the data are smaller than the symbols. Glasses A, B, C and D had average pore sizes of approximately 3.3, 3.9, 4.5 and 5.0 nm; all glasses had a porosity very close to 30%. From [110].

position of all solid atoms, and hence the surface area, PSD, porosity, connectivity, etc. In view of this, together with the fact that they appear to be realistic representations of the morphology of real CPG and Vycor glasses, they provide ideal systems on which to test commonly used characterization methods. In such calculations the LJ parameters for the substrate atoms are set equal to $\sigma = 0.27$ nm, $\epsilon/k = 230$ K, the values used to represent bridging oxygen atoms in silica [222]. Simulations of nitrogen adsorption in these glasses provide nitrogen adsorption isotherms (figure 29), which can be analysed by standard methods [122] to estimate the surface area, PSD and porosity. The accuracy of these conventional methods can be rigorously tested by comparison of such estimates with the exact values. Tests of this sort have been made for the BET (Brunauer–Emmett–Teller) method for determining surface area [109] and the BJH (Barrett–Joyner–Halenda) method for obtaining the PSD [110]. For the BET method, the estimates of surface area are found to be accurate for large mesopores (pore diameters down to about 5 nm), but corrections become significant for smaller pores, with the BET method overestimating the surface area by as much as 20–25% for pore diameters of 2 nm. The principal source of error in the BET method arises because the monolayer density for cylindrical pores is generally higher than that for a planar surface; the latter value is commonly used in applying the BET method to obtain surface areas. The BJH method for the PSD relies on the modified Kelvin equation, and so is expected to give pore diameters that are too small, based on previous tests for the independent straight cylinder model (see figure 15). This is confirmed by tests for the more realistic glass model of figure 28. Typical results for the PSD are shown in figure 30. The BJH method predicts PSDs which are narrower and have maximum pore diameters that are about 1 nm smaller than the exactly known geometric PSDs. This error is believed to be due to a combination of factors: (a) errors in using the modified Kelvin equation for small pores (figure 15); (b) the use of the independent cylinder model in

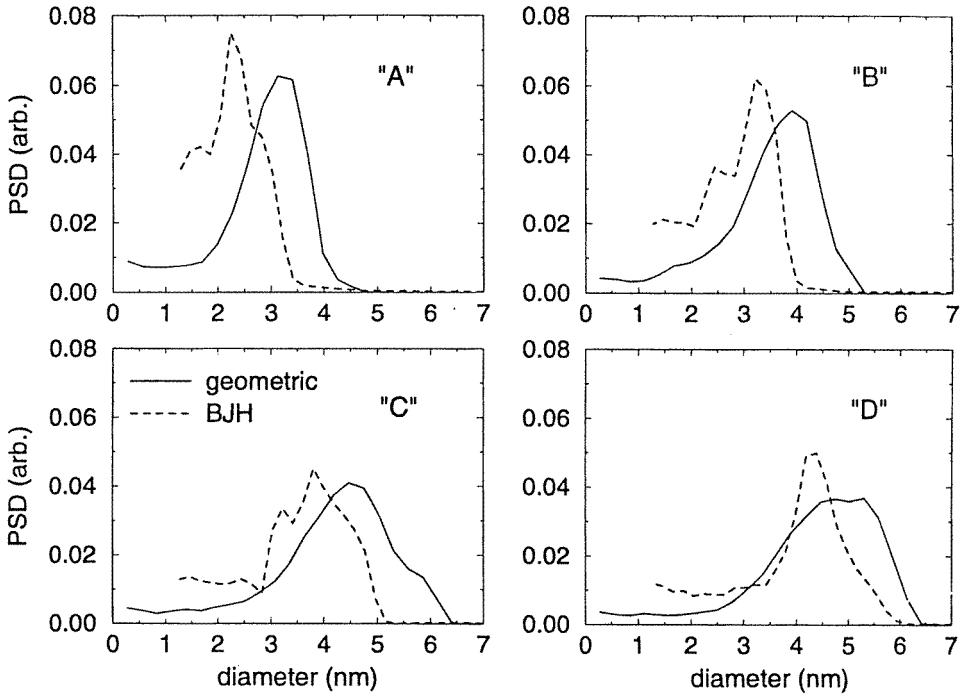

Figure 30. PSDs from geometric analysis using spherical probes (solid curves), together with PSD estimates from BJH analysis (dashed curves) of the nitrogen adsorption isotherms of figure 29. From [110].

BJH, which fails to include pore tortuosity, surface irregularities and networking effects; and (c) the use of a standard reference isotherm for a planar surface, which underestimates the density of the adsorbed layers.

These model glasses have also been used to study the adsorption and capillary condensation of xenon [111]. Some typical results are shown in figure 31, together with results for the independent straight cylinder model, and experimental results for Xe in Vycor [46]. Direct comparison of the simulation results with the experimental ones is complicated by the fact that the average pore size and porosity are not accurately known for the experimental glass. However, it is clear that for the independent cylinder model the shape of the hysteresis loops, and also the shape of the isotherm at low pressure, are both incorrect. For the more realistic glass model of figure 28 the isotherms are qualitatively very similar to the experimental ones. Slight adjustments to the mean pore size and porosity in the model calculations would bring the two sets of results into quantitative agreement.

Cracknell *et al* [56] have used molecular simulation to study capillary condensation as a function of pillar density in model pillared clays (consisting of slit pores in which the walls are spanned by cylindrical pillars placed on a hexagonal close-packed lattice). They find that below a critical pillar density capillary condensation occurs. The capillary condensation pressures are below those for the slit pores, due to the increased confinement.

Disordered (random) porous media. Many porous materials, particularly oxides such as silica, alumina, titania, zirconia, thoria and ceria, are formed from colloidal suspensions by aggregation and suspension [155, 306, 307, 363]. They are composed of microscopic particles

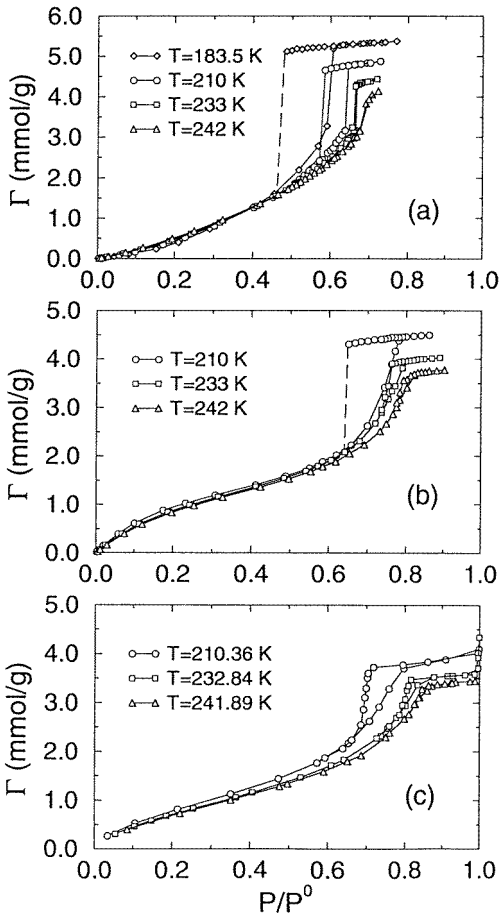

Figure 31. Adsorption isotherms for xenon in Vycor glass: (*a*) molecular simulations for the independent cylindrical pore model, pore diameter 5.1 nm; (*b*) simulation results for the glass model of figure 28, mean pore size 4.6 nm, porosity 30%; (*c*) experimental results of Burgess *et al* [46]. From [111].

that are interlinked in a random network. These particles have sizes that range from about 2 to 100 nm, and are often of spherical or cubic shape, but may also be in the form of rods or platelets [306]. Such materials have often been modelled as a rigid matrix of solid spheres ('cannonball solid'), usually randomly arranged. Some of the possible variations on such a model are shown in figure 32 [284]. Models (*a*) and (*b*) differ at higher porosities in that some unconnected spheres can occur in (*a*), as shown by the sphere labelled 1, but not in (*b*). While model (*b*) is probably the most realistic representation of this kind of disordered media, models (*c*) and (*d*) are often easier to study theoretically. MacElroy and co-workers [210,211,284] have developed models of this type for silica xerogels with solid spheres having a diameter of 2.4–2.8 nm. Silica spheres were generated using Monte Carlo simulations and a quench procedure, coupled with intermolecular interactions which included both pair and three-body potentials with parameters proposed by Feuston and Garofalini [89]. Connected matrix structures, such as (*b*) and (*d*) in figure 32, can be formed by starting with a randomly close-packed assembly of hard spheres with porosity of 0.367; such an assembly is assumed to be fully connected. Spheres are then randomly removed to get the desired porosity, with subsequent scanning to check that remaining spheres are all connected. Random structures such as (*a*) and (*c*) in figure 32 can be generated by carrying out a Monte Carlo run to generate a random configuration for hard spheres. The desired porosity is obtained by setting an appropriate lattice spacing

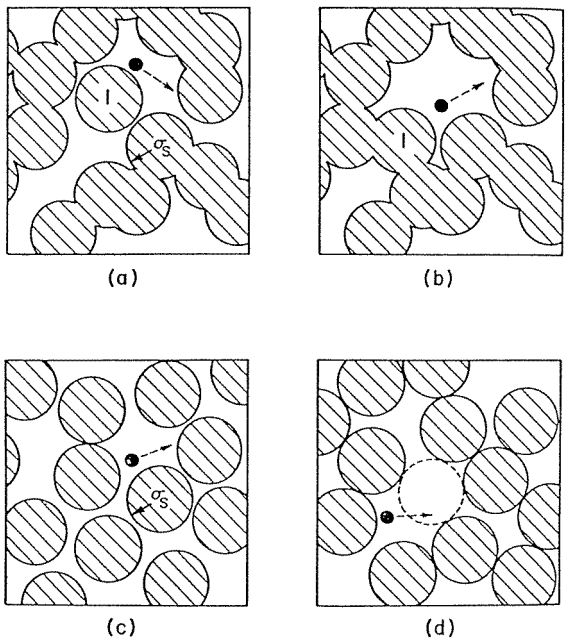

Figure 32. 'Cannonball' models for a disordered porous medium: (*a*) random overlapping spheres; (*b*) randomly connected overlapping spheres; (*c*) random non-overlapping spheres; (*d*) randomly connected non-overlapping spheres. Shaded regions are the solid matrix, the small solid circles represent a fluid molecule moving through the void space. From [284].

in the initial fcc lattice. MacElroy and co-workers used these structures to study adsorption and diffusion of methane in a silica xerogel. They found good agreement with experimental data using the more realistic connected model, (*d*) of figure 32. Connectivity of the spheres forming the matrix was found to have a pronounced effect on the diffusion rates. However, they did not determine phase diagrams for capillary condensation.

Capillary condensation in such matrices has been studied by both theoretical and simulation methods. Monson and co-workers [164–166, 274, 323] have used GCMC simulations to study a simplified version of the system used by MacElroy and Raghavan [211] to investigate methane in silica. In the work of Monson *et al* the matrix was one of random non-overlapping spheres, and the fluid–solid interaction was averaged over the atomic structure of the surface, to give the analogue of the (9, 3) potential model for planar surfaces. They found [274, 323] that the coexistence curve for capillary condensation, as determined from the simulations by thermodynamic integration (see section 2.1), is much narrower than for the bulk fluid, and that the pore critical point moves to lower temperatures and higher densities, in agreement with experimental findings (figure 33). They also find that at low temperatures a second transition occurs, from a low-density gas-like phase to a phase of moderate density. This second transition is associated with the wetting behaviour of the fluid in regions of the solid matrix where the spheres are more densely packed, and involves high-density fluid permeating these more confined regions. The effect of varying the strength of the attractive fluid–solid forces on the coexistence curve was also studied [274]. It was found that the form of the coexistence curves was sensitive to this variation. Adsorption isotherms [323] showed hystersis loops that were qualitatively in agreement with experiment for this system. Sarkisov *et al* have also obtained the coexistence curve for a matrix of spheres placed on a fcc lattice, and

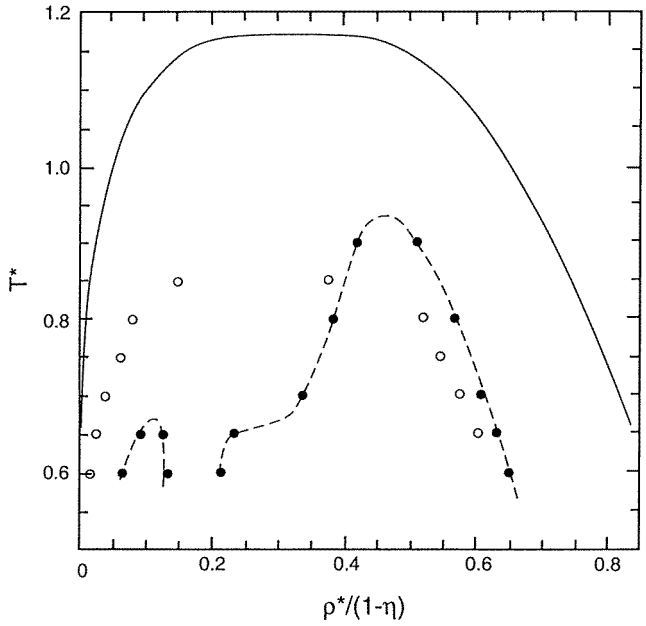

Figure 33. Temperature-density phase diagrams for a LJ fluid in a solid made up of a matrix of spheres. The coexistence curve for the bulk fluid is shown as the solid curve. Filled circles are the results for the random array of non-overlapping spheres, with a sphere density corresponding to a silica xerogel, and a fluid modelled on methane. Open circles are for an ordered fcc matrix. Here $T^* = kT/\epsilon$ and $\rho^* = \rho\sigma^3$, where ϵ and σ are the fluid–fluid LJ parameters; $(1-\eta)$ is the porosity, with η being the fraction of the volume occupied by the solid spheres. From [323].

these results are also included in figure 33. This latter coexistence curve is quite different from that for the random matrix, being similar to the bulk coexistence curve, but shifted to lower temperatures; it does not show the second low-density transition. Evidently this transition arises from the spatial variation of the density of solid spheres, and hence of the porosity.

The simulation results for these disordered porous media should be treated with caution, since the systems studied are not large enough to represent a truly random sample, and are periodic at the length scale of the simulation box. Several recent studies [5, 40, 76], using larger systems and in some cases [76] histogram re-weighting, have shown that the resulting phase diagram is highly sensitive to the particular configuration used for the solid particles.

It is interesting to note that Bryk *et al* [45] have found similar phase diagrams to that shown in figure 33 for a LJ fluid adsorbed in a system of semi-permeable walls. Their investigation is based on the Kierlik–Rosinberg form of density functional theory. For intermediate and low potential barriers separating the pores, coexistence curves exhibit two critical points and a triple point, similar to that shown in figure 25(*b*). The two parts of the coexistence curves correspond to condensation in the pore and in the semi-permeable walls.

A variety of approaches from liquid-state statistical mechanics have been applied to disordered porous materials of this kind. The system can be treated as a so-called 'quenched-annealed' binary mixture, in which the solid matrix of spheres is the 'quenched' component whose configuration is obtained by sampling from an appropriate equilibrium ensemble, while the second component is the fluid adsorbed into the matrix [316]. Madden and Glandt [218] worked out the statistical mechanics of such a system, including the appropriate cluster expansions and Ornstein–Zernike equations that relate the various total and direct

correlation functions. Givens and Stell [113, 115] subsequently showed that the Ornstein–Zernike equations given by Madden and Glandt were only approximate, and derived exact equations. These derivations relied on the 'replica method', which exploits a mathematical isomorphism between a partly quenched system and a limiting case of a corresponding equilibrium system, called the *replicated* system. The resulting Ornstein–Zernike relations are a set of coupled integral equations involving correlation functions for the matrix–matrix, matrix–fluid and fluid–fluid structure, and are known as the replica symmetric Ornstein–Zernike (RSOZ) equations. A range of approximate methods based on liquid-state theory have been explored using the replica method [114, 172–174, 205, 289, 298, 299, 317, 361]. Several of these methods have been used to determine temperature-density coexistence curves for such systems [172–174, 299]. The results are sensitive to the closure relation used in conjunction with the RSOZ equations. The most realistic of these calculations to date appear to be those based on a quench-annealed lattice gas model, solved using the mean spherical approximation as closure of the RSOZ equations [173, 174]. This model produces gas–liquid phase envelopes in which the critical temperature is lowered and the critical density raised relative to the bulk, as in the experiments and simulations. For relatively high densities of matrix particles, and sufficiently strong attraction between the fluid molecules and the matrix particles, a second pre-condensation transition is observed at low temperatures that is similar to that shown in the simulation results of figure 33. However, the calculated results, particularly those for the pre-condensation transition, are sensitive to the lattice used and the thermodynamic route chosen (e.g. 'compressibility' versus 'energy' routes).

4. Layering transitions

At relatively low temperatures, adsorption isotherms on smooth surfaces can show step-wise behaviour, which is generally interpreted as layer-wise adsorption. In these situations, the adsorbing gas prefers to complete each successive monolayer before beginning the next one. In addition, the steps in these isotherms are often quite sharp, which led to speculation that these systems undergo a series of first-order phase transitions as layers are added.

This hypothesis has been extensively tested by experiments, lattice-model simulations, molecular simulations, and classical DFT and integral equation theory calculations. As a result, these layer-wise transitions have been incorporated into a much larger picture of surface phase behaviour involving the interplay between the *surface roughening* and *surface wetting* transitions.

4.1. Experiments

Many experimental observations of layering transitions have been made on clean, planar surfaces such as graphite. Measurements have also been made on metal surfaces, magnesium oxide 'smoke', exfoliated graphite and graphite foams, and other high-surface area materials.

Methane adsorption on the MgO(100) surface shows stepwise behaviour in the isotherm at 87.4 K [104] up to the completion of the third layer, after which the isotherms become smooth; at the lower temperature of 77 K up to five steps are found in the isotherm [225]. These strongly adsorbed layers are found to be quite solid-like from quasi-elastic neutron scattering experiments [24, 25]. Similar stepwise adsorption has been found for methane adsorption on nonporous graphite at 77 K [192], as well as on exfoliated graphite and graphite foam [26].

Oxygen adsorbed on graphite also exhibits layering transitions at low temperatures, with the number of observed transitions dependent on the temperature. These layers are found

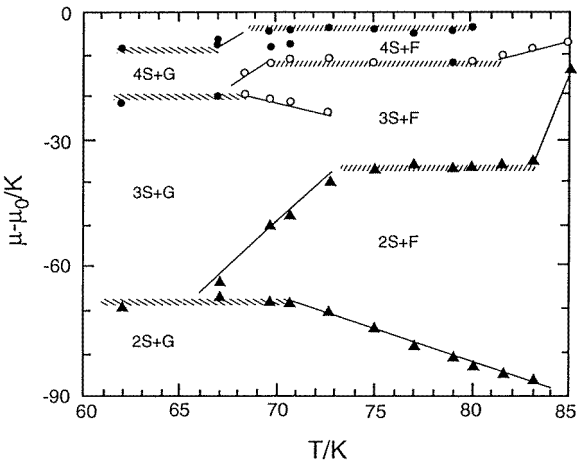

Figure 34. Phase diagram for argon multilayers on graphite. The thick cross-hatched lines indicate first-order phase transition regions (vertical isotherm steps) while the thin lines denote possible continuous transition lines (kinks in the isotherms). The symbols S, G and F, represent solid, gas and fluid phase, respectively. The fluid or disordered phase most likely exists in a region where the vertical extent of the liquid phase is not well defined. Layer critical temperatures are located at $T_c(2) = 70.0 \pm 0.3$ K, $T_c(3) = 68.3 \pm 0.5$ K, $T_c(4) = 67.2 \pm 0.2$ K and the layer triple points at $T_t(2) = 66.5 \pm 0.5$ K and $T_t(3) = 67.2 \pm 0.5$ K. Reproduced from [191].

to be crystalline below 43.8 K and liquid-like at higher temperatures [394]; the complete adsorbed phase diagram, involving adsorbed multilayer solids, liquids, and mixed states, (e.g., solid films, liquid films, and surface-melted films) has been obtained by neutron diffraction [49, 186]. In this system, transitions occur between crystalline layers at low temperatures, between liquid-like layers at temperatures much above the triple-point temperature, and between states composed of some liquid-like and some crystalline layers at intermediate temperatures.

Argon adsorption on graphite has also been extensively studied using ellipsometry [394], neutron scattering [191, 193], adsorption isotherm measurements [194] and x-ray scattering [194], and a complex adsorbed phase diagram has been determined in which as many as seven layering transitions appear at low temperatures. One estimation of this phase diagram is shown in figure 34. Remarkably, a second series of layering transitions occurs at higher temperatures between films which are thought to be surface-melted solids; the second series of transitions is offset in pressure from the first, leading to 're-entrant' behaviour [394], in which layerwise transitions disappear near 69 K and then reappear near 73 K, and then disappears at yet higher temperatures, as shown in figure 35. This behaviour indicates that a completed liquid-like layer can be re-solidified by additional adsorption [295].

Other gases that have been shown to have complex layering adsorption phase diagrams are ethylene [175, 345], ethane [256] and xenon and krypton [395]; much of the work in this area has been concisely reviewed [143].

4.2. Theoretical treatments and systematics of surface phase transitions

Pandit *et al* [282] discuss the systematics of layering, wetting, and roughening on a planar surface in terms of the strength and range of the surface-fluid interaction, using a lattice-gas approach. For a strongly-adsorbing surface, where the surface-fluid interaction is large compared with the fluid–fluid interaction, adsorption at low temperatures proceeds through a series of layer-wise first-order transitions, with the film thickness becoming infinitely large at liquid–vapour coexistence. Each of these first-order transitions has an associated critical layer temperature, at which that layer transition becomes smooth. These layer critical points approach the *surface roughening temperature* T_R at liquid–vapour coexistence. The roughening temperature can also be physically understood as that temperature where the free energy of defect formation in the surface drops to zero, which leads to a divergence in the

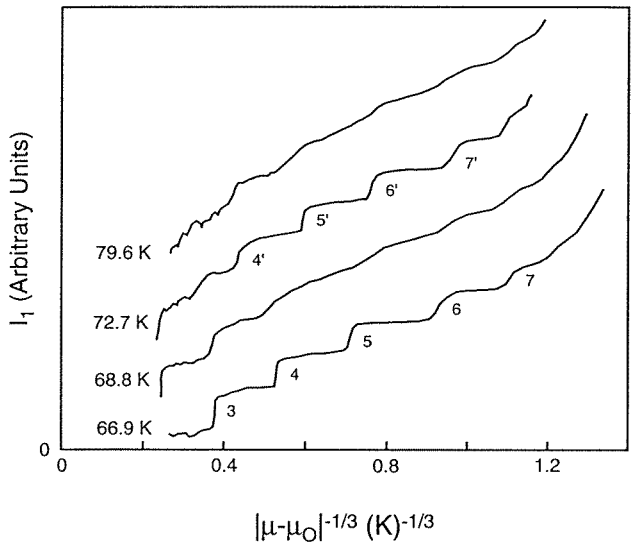

Figure 35. Ellipsometric coverage isotherms for argon on graphite at four temperatures. The abscissa is a function of the reduced pressure, given by $[\mu_n - \mu_0 = T\ln(p_n/p_0)]$. With the particular functional form used, the simple Frenkel–Halsey–Hill model predicts a uniform staircase. Reproduced from [394].

height–height correlation function along the surface. Thus, at the roughening temperature and above, there can be no layer-wise phase transitions in this type of model.

For intermediate-strength surfaces, where the interaction between fluid and surface is comparable with the fluid–fluid interaction, the picture is complicated by the additional presence of a non-zero wetting temperature. For adsorption at temperatures below the wetting temperature, the adsorbed layer is of finite thickness even at bulk liquid–vapour coexistence, while at temperatures above, the thickness of the adsorbed layer diverges. The wetting temperature is lower than the roughening temperature, and the layer-wise transition lines intersect the bulk liquid–vapour curve. This leads to adsorption isotherms at intermediate temperatures that show several steps at low pressures followed by a smooth divergence at high pressures.

Pandit *et al* also discuss the critical wetting regime in depth, as well as the layer-wise transitions that occur in the critical drying region; since this section focuses principally on physisorbed systems of the type discussed in section 3, we will not discuss these here.

Another surface phase transition relevant to confined liquids is the *prewetting* transition, which corresponds to a discontinuous but *finite* jump in the adsorbed layer thickness, typically of several monolayers' size. The prewetting transition is first order with an associated critical point, and occurs for some intermediate-strength substrates; prewetting has been verified by both lattice-gas simulations [79, 262] and experiments on binary mixtures [169] and surface melting [25]. Studies of the prewetting transition in lattice models [262] have confirmed that this transition (and other layering transitions) are of the two-dimensional Ising universality class.

In porous materials the asymptotic growth of the adsorbed layer is affected by the curvature of the pore surfaces, and ultimately interrupted at the point of pore filling. This leads to isotherms that consist of layer-wise regimes at low pressure, which lead to smooth multilayer adsorption at intermediate pressures and finally capillary condensation at higher pressures.

The prewetting transition is also still observable in some pore models [262]. Confinement in a porous material suppresses both the roughening and wetting transitions, because they involve macroscopic growth and fluctuations in the thickness of the adsorbed layer. In addition, the nontrivial geometry and surface heterogeneity of most porous materials tends to smooth out layer-wise behaviour.

Wetting and layering have been extensively studied in the context of the simple-cubic Ising model and other lattice gases. In these studies, bulk and surface external fields replace the pressure and surface-fluid attractions relevant for the gas adsorption problem. Many studies using mean-field arguments [68, 73], the quasichemical approximation [6], renormalization-group solutions [319], and Monte Carlo simulations [72, 73] have demonstrated the basic structure of the surface phase diagrams involving layering transitions. Binder and Landau [30, 31] used Monte Carlo simulations to systematically map out the changeover from layering to roughening to wetting behaviour as both the surface field strength and the first-layer spin-coupling energy are changed.

Some of the drying and layering transitions predicted by lattice model studies have not been observed in real adsorbed systems, possibly because the range of adsorption energies available with common materials is not very great. However, many adsorbed films do have quite complex phase diagrams due to the presence of solid–liquid transitions, which can (in principle) occur at different temperatures in each adsorbed layer, with each layer freezing temperature dependent on the total coverage. In addition, experiments (section 4.1) have shown a complex interplay between (layer-wise) *surface melting* in the adsorbed film and the layer-wise buildup of the adsorbate.

Some theoretical studies of adsorption using Potts models and related multi-state lattice models have focused on the interaction of solid and liquid states in the adsorbed film. These are lattice models where a given site can be unoccupied, and if occupied, can be in one of several symmetric states. Neighbouring occupied lattice sites in the same state have a more favourable energetic interaction; this gives rise to distinct solid and liquid phases, characterized by order and disorder in these symmetric states. Kahng and Ebner [163] used six- and eight-state Potts models in both mean-field studies and Monte Carlo simulations to describe the adsorption of simple gases on graphite, and obtained many complete surface phase diagrams, exhibiting a rich variety of behaviour. Another model which reduces to the three-state Potts model has been used in the mean-field approximation to study solid–liquid transitions in adsorbed films [353], and Potts-type models have been extensively studied in the context of surface melting, which is a closely related problem [105, 158, 352].

Layering transitions on strong substrates at low pressures are qualitatively easy to understand, as they may be attributed to the packing of adsorbed molecules that maximizes surface-fluid interactions. However, for thicker layers, where the substrate potential is effectively zero near the surface of the adsorbed layer, and for weaker substrates, where even the first adsorbed layers are quite liquid-like, the phase behaviour of the adsorbed film is governed by very delicate fluid correlations acting over long length scales.

DFT has been used to characterize capillary transitions and adsorption in porous materials (see section 3), and has also been used to study layering transitions. Ball and Evans [13] used non-local DFT to study the LJ fluid and the Yukawa fluid both at solid surfaces and in narrow cylindrical pores. At low temperatures steps were found in the adsorption isotherms, with very small associated metastable regions. These first-order layering transitions disappeared at a series of layer critical points, as predicted by earlier work with lattice models. In cylindrical pores the layering transitions are shifted to lower pressures (for the same fluid–wall potential), and there is a competition between the layering transitions and capillary condensation. Under the conditions used in this study, solid-like layers and layer-melting transitions were not

observed. Balbuena and Gubbins [11] have used non-local DFT to study the effects of temperature, pore width and intermolecular interaction parameters on layering transitions in slit pores. Both fluid–fluid (ff) and solid–fluid (sf) interactions were of the LJ type. The layering transition behaviour was strongly influenced by $\epsilon_{sf}/\epsilon_{ff}$, the ratio of solid–fluid to fluid–fluid attraction. Henderson [142] has used mean-field DFT with and without linear renormalization to fully analyse the interaction of the many competing length scales involved in wetting and prewetting in adsorbed films, and related these phenomena to theories of the asymptotic structure of liquids and mixtures.

4.3. Molecular simulation

Layering transitions have been studied using molecular simulations in a number of geometries. In an early study, Perterson *et al* [292] used GCMC simulations to study layering transitions in a cylindrical pore of diameter 14σ, where σ is the LJ diameter of the fluid molecule. The pores had structureless walls (the cylindrical analogy of the $(9, 3)$ fluid–wall potential was used), and the fluid–wall potential was strongly attractive; LJ parameters typical of a methane-like fluid in a carbon pore were used. Three layering transitions were found, followed by capillary condensation. In addition, a quasi-two-dimensional freezing transition occurred in the first layer at a pressure below that corresponding to the formation of the second layer. Maddox and Gubbins [220] observed stepped adsorption isotherms in grand canonical Monte Carlo simulations of argon and nitrogen in models of buckytubes; this behaviour is to be expected due to the strength and smoothness of the adsorbate-fluid potential. Interestingly, in the correponding desorption isotherms, most of the stepped behaviour is not observed because the capillary hysteresis loop is so large in these calculations; most of the layering transitions occur within the hysteresis loop of the larger transition. Since the position of the thermodynamic capillary transition is not known, this may mean that some of the layering transitions are entirely metastable, and occur at pressures where pore filling is thermodynamically favourable.

The structure of argon films adsorbed on graphite has been studied with canonical Monte Carlo simulations [295] in order to better understand experimental results. By analysis of the layer densities and in-layer pair correlation functions, the solid-like or liquid-like character of each adsorbed layer could be determined as a function of temperature and total adsorption. This reinforced the picture of reentrant layering developed from experimental studies; that increasing adsorption causes freezing transitions in already completed layers. The prewetting transition for argon adsorbing on a '9–3' wall has also been observed and characterized using molecular simulations, and the interplay of prewetting, layering and wetting in this system has been examined [85, 91]. Simulations of neon adsorption on homogeneous surfaces have found prewetting behaviour, while prewetting is absent on similar heterogeneous surfaces, indicating that substrate roughness can significantly affect adsorbate phase behaviour [34, 62].

Layering, freezing and capillary condensation transitions have been studied in a simulation study of methane adsorption in graphite slit pores [162]. In this study, the freezing transition was observed in the first layer only, and was signalled by a kink in the adsorption isotherm (see figure 36) and marked change in the in-layer pair correlation function from that of a strongly ordered liquid to that of a crystalline solid, and molecular dynamics studies found a decrease in the self-diffusion coefficient of molecules in the first layer of more than two orders of magnitude. The additional adsorbed layers in this figure are also thought to be solid at this temperature, so that the transition from a one-layer to a two-layer system (and beyond) is a transition between solid phases. As in the simulation study of adsorption in buckytubes, for the larger pores several layering transitions were observed at higher pressures *within* the

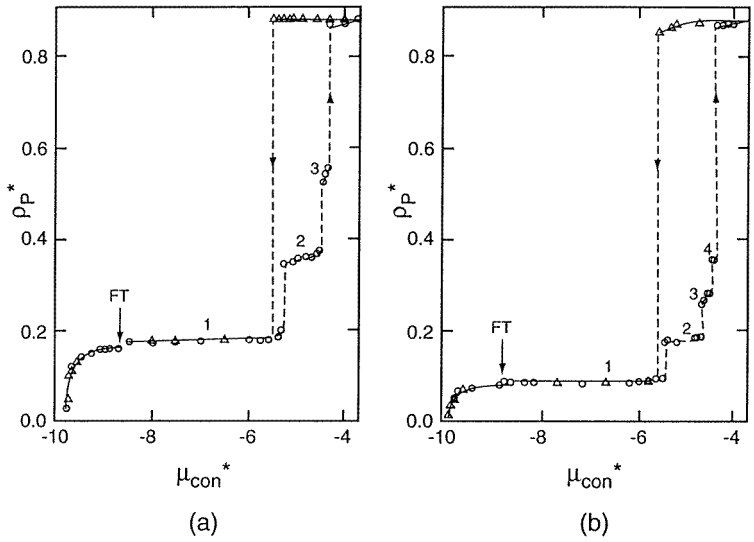

Figure 36. GCMC results for adsorption isotherms for methane in graphite slit pores at $T^* = 0.5$ and (*a*) $H^* = 10$, (*b*) $H^* = 20$, where $T^* = kT/\epsilon$ and $H^* = H/\sigma$. Adsorption is denoted by circles, desorption by triangles, and first-order transitions as dashed lines. FT is the freezing transition. Reproduced from [162].

capillary condensation hysteresis loop. The number of layering transitions observed depended on the width of the pore, as shown in figure 36; in pores 5σ (5 methane diameters) wide only one layering transition was observed before condensation, while in pores 10σ wide three transitions were seen, and in pores 20σ wide four transitions were found. The situation in this and similar systems is that a competition exists between layering transitions, which are induced by a single surface, and capillary condensation, which is caused by confinement. For sufficiently narrow pores, capillary condensation obscures many (or all) layer-wise transitions, while for large pores, layering phenomena mediate the thickness of the adsorbed layer, and thus the pressure at which capillary condensation in the central part of the pore ultimately occurs.

Forsman and Woodward [95] have used isotension ensemble MC simulations and non-local DFT to study layering transitions in a slit pore with structureless walls. The interactions were of the LJ type, and the fluid–wall interaction was given by the (9, 3) model (see section 2.9). In the isotension ensemble the number of molecules, N, the average component of the pressure tensor parallel to the walls, $P_\parallel$, and the temperature are fixed, but the surface area of the pore walls is allowed to fluctuate.

5. Liquid–liquid equilibria

Problems in liquid–liquid equilibria are often considered as special cases of liquid–vapour equilibria, since both systems can (in the vicinity of a critial point) be mapped onto Ising-type lattice models. However, the dynamic properties of binary liquid mixtures and liquid–vapour systems are very different, and the range of coupling strength to external variables is much larger for the liquid–liquid systems.

In confined systems, most studies (experimental or theoretical) have focused on either the dynamic properties of a near-critical binary mixture or the position and properties of the

phase envelope itself. A number of general trends have been observed. Firstly, these systems exhibit strong metastability well within the two-phase region, and therefore both hysteresis and history dependence are commonplace. Secondly, macroscopic phase separation does not occur on the timescales accessible in the laboratory. Thirdly, the critical temperature and mole fraction (as located by the heat capacity singularity, onset of opalescence, etc) are shifted, and the signature of these measures is considerably broadened.

Three important and appealing hypotheses have become popular in describing the dynamics and thermodynamics of these systems, and most experimental and simulation results are interpreted with the predictions of one or more of these in mind.

Brochard and De Gennes suggested that the effect of a containing gel on a liquid mixture should be much like a *random field* [41, 66]. This hypothesis should be relevant when the correlation length of the gel network is short compared with the correlation length of the liquid mixture, which will occur near to the liquid–liquid (demixing) critical point, if ever. The presence of the gel might then be considered as a weak, short-ranged random field acting on the near-critical mixture, a problem which ought to be qualitatively described by the *random field Ising model* (RFIM), itself an object of intense study. The validity of this argument depends on both the topological properties of the gel network, and the strength of interaction (in this case, a preferential attraction for one component) between the gel and the liquid mixture. As the experimental focus shifted from earlier studies on agarose and polyacrylamide gels to later studies using rigid porous glasses and aerogels, this argument was extended to these new systems. The random-field picture is difficult to investigate using molecular simulations or fine-grained lattice models due to the very large length scales involved. While using a very coarse-grained model for the fluid and gel network alleviates this problem, this is essentially just simulating an explicitly random-field lattice model, and the mapping between the real (or fine-grained model) systems and the RFIM remains unproven.

The second approach to these systems, put forth by Liu and others [202], is to consider the *wetting* properties of the binary mixture in a porous material. Through determining the bubble radius as a function of wetting forces and surface tension, these workers were able to derive a 'wetting phase diagram' for a binary liquid mixture in an ideal cylindrical pore. This theory predicts an equilibrium between *tube* configurations, in which one component is 'plated' out onto the pore surface, *plug* configurations, in which cylindrical plugs of both components exist, separated by hemispherical interfaces, and *capsule* geometries, which might be described as a plug-arrangement inside of a tube structure. For sufficiently small capillaries, capsule geometries are never observed; at near-critical temperature the stable configuration is tubular, while at lower temperatures plugs are preferred. For larger pores, capsules are intermediate between tubes and plugs, and the range of temperature in which tubular configurations are observed becomes very small. This model predicts strong *kinetic* barriers to complete phase separation at low temperatures; the plug configurations are strongly metastable. The capsule configurations are not prevented from complete phase separation, but the process is shown to be so slow that it is not observable on a convenient timescale.

Thirdly, these systems are often approached as examples of *finite-size scaling* phenomena. Finite-size scaling has been extensively reviewed elsewhere [16, 29]; here we summarize its possible application to confined systems. In a bulk system near to a critical point, the correlation length in the system is described well by a function of the form $\xi_c = \xi_0[(T - T_c)/T_c]^{-\nu}$, where T_c is the critical temperature, ν is a critical exponent, and ξ_0 is a proportionality constant. Likewise, the behaviour of quantities such as the specific heat, magnetic susceptibility, and isothermal compressibility are described well by the sum of a 'regular' part and a divergent part with a scaling function of similar form, plus possible corrections. In a *planar* pore system, the pore structure will limit the growth of the correlation length in one dimension, and a crossover

will occur to two-dimensional Ising behaviour very near the critical point, which will be shifted as [252]

$$\frac{|T_c - T_m(L)|}{T_c} \propto L^{-1/\nu} \tag{25}$$

where $T_m(L)$ is the position of the shifted maximum and L is the pore width of the system. In a cylindrical pore system, correlations can only grow large in one dimension; it is well known that in such a system no true first-order phase transition can occur, and so only a remnant of phase behaviour is observed, with no real critical behaviour or divergences. Most real materials have complex geometries, which may be locally cylindrical or planar, but have connections (and correlations) between pore sections, which are the basis for the random field picture described above. Many studies, as described below, attempt to correlate the average pore size with the shift in critical temperature from that of the bulk system using equation (25) and to confirm other hypotheses from the scaling theory, despite the non-ideality of the experimental materials' structure.

These attempts are frequently complicated by the fact that it is difficult to combine data from materials of significantly different pore geometries because the meaning of the accepted average pore size in different classes of materials is different. This is one reason why CPGs have been extensively used in these studies; these materials can be prepared with a wide range of pore sizes with essentially the same network morphology.

5.1. Experimental results

5.1.1. High-porosity materials. Maher *et al* [226] used light scattering to study the near-critical behaviour of both isobutyric acid plus water and 2,6-lutidine (2,6-dimethylpyridine) plus water in agarose and polyacrylamide gels of varying weight fraction. They report that strong light scattering occurs when the systems were quenched into the two-phase region of the binary mixtures, and that this scattering did not cease for hundreds of hours. They located the temperature at which opalescence was observed as a function of the concentration of the mixture; these data resembled the phase diagrams of the bulk mixture, except that they were shifted slightly to favour the more strongly adsorbed component, and occurred at temperatures outside (below, in the case of the water–isobutyric acid mixture and above, in the case of the water–lutidine mixture) the bulk phase envelope.

Frisken and Cannell and co-workers have extensively studied the water-lutidine mixture and the water-isobutyric acid mixture in dilute silica gels using both light scattering and neutron scattering. These studies have focused principally on the properties of the near-critical mixture in the gel, and have shown that the simple random-field approach to these systems does not fully account for many of their properties.

The water–isobutyric acid system is a type II binary mixture and has an upper critical solution temperature of $T_c = 299.83$ K with critical weight fraction near 38.8%. In their study of this mixture in 4 wt.% silica gel [99], the dynamics of order parameter (in this case, concentration) fluctuations were followed as the temperature was brought down towards the critical temperature. At high temperatures, the gel-mixture system had the same exponential fluctuation decay as the bulk mixture. Nearer to the critical point a wavelength-dependent activated term becomes important, with the most significant contributions for large q vectors. At a reduced temperature of $t \sim 0.002$, (*above* the critical temperature) the system spontaneously orders and a very long-time relaxation appears, which later dies away. A later study [101] showed that this mode re-appeared with each successive temperature decrement, but increasing the temperature had no such effect. This is consistent with a phase separation process. For temperatures slightly below the critical solution temperature, similar behaviour

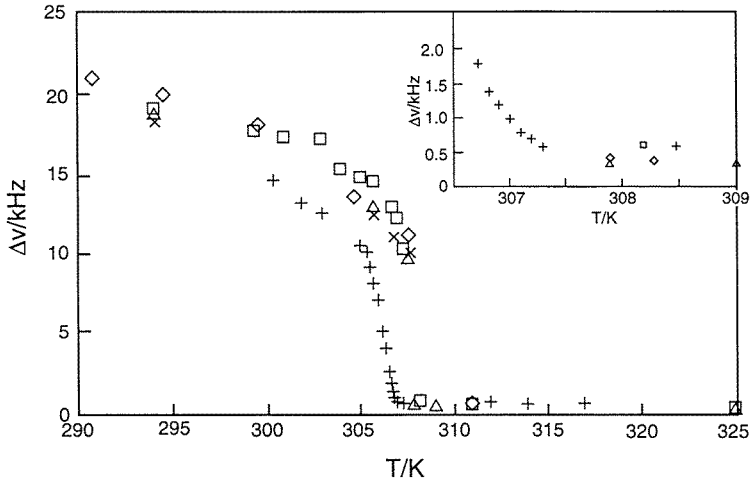

Figure 37. Phase diagram showing the relationship between the water/isobutyric acid coexistence curve of the bulk mixture (open circles, crosses), the narrow two-phase region of the silica gel/mixture system, which lies between the open diamonds, and the slow mode onset temperature (solid diamonds). Reproduced from [399].

is observed, and for deeper quenches, macroscopic phase separation was found to occur over a period of months. Using neutron scattering, [100] found that in the two-phase region of a bulk mixture of water and lutidine a gel-confined mixture showed scattering changes consistent with a slow phase separation process in which the liquids segregate into large domains.

Further studies [8] showed that for low isobutyric acid concentrations, the phase-separation induced by pressure quenching to within the coexistence envelope was described well by a dynamic scaling model with the domain size growing as $t^{1/3}$, indicating that 'domain pinning' behaviour due to the gel network is not present. For higher concentrations of acid, the scaling hypothesis did not hold at any observed time. The overall behaviour of these systems is similar to that of random field models, with the notable exception that the water–isobutyric acid–gel system appears to relax to equilibrium from a 'frozen' domain state over an accessible timescale, while random-field models do not.

The phase diagram of the gel/mixture system was measured using a more thermodynamically oriented approach, in which the concentration of isobutyric acid in the gel system was determined as a function of coexisting *bulk-phase* concentration [399]. Phase separation in the gel system was found for temperatures of 15 and 19 °C, but not at 23 °C, indicating that the critical temperature in the gel has been lowered from its bulk value of near 25.72 °C. The shift in concentration in the gel system was more dramatic; the entire phase envelope was shifted to one side of the bulk critical concentration, as shown in figure 37.

5.1.2. Low-porosity materials. Voronov *et al* have studied the behaviour of the specific heat of a mixture of water and 2,6-lutidine imbibed in porous glasses [75, 375]. This mixture has also been extensively studied by several other groups in the context of confined liquid–liquid separation (see below). At constant pressure, water and 2,6-lutidine have a *lower* critical solution temperature (LCST), so that at temperatures *above* this T_c the liquids separate into two phases. The critical *weight* fraction of the mixture is $x_c = 0.290 \pm 0.005$ (equivalent to a critical *mole* fraction of 0.0642 ± 0.0001) and the critical temperature is $T_c = 306.79 \pm 0.01$ K [375]. In these studies the heat capacity was measured as a function of temperature for both critical

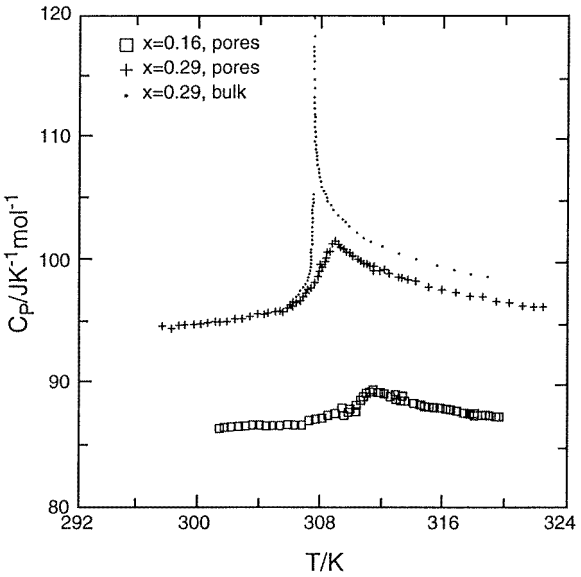

Figure 38. The specific heat of 2,6-lutidine + water in CPG of 100 nm average pore size, at $x = 0.29$ and at $x = 0.16$, and also the bulk specific heat at $x = 0.29$ as functions of temperature. Reproduced from [75].

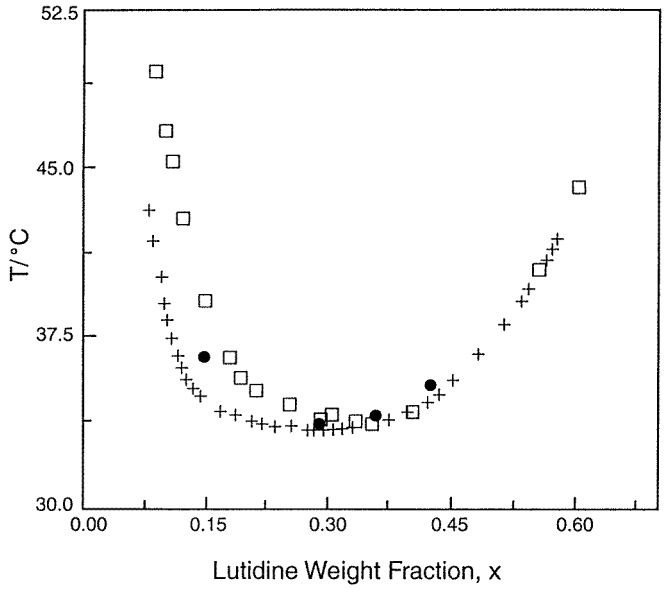

Figure 39. Coexistence curve of a 2,6-lutidine–water mixture in the bulk (+), in the porous glass with a characteristic pore size of 1000 Å (□), and in the porous nickel with a pore size of 2500 Å (●). Reproduced from [375].

and off-critical mole fractions.

In these experiments the peak in the heat capacity around the critical point was shifted to higher temperatures, and dramatically rounded, as shown in figure 38. The amount of shift and rounding varied with pore size; in smaller pores the peak position was shifted further and rounded more than in larger pores. By locating the heat capacity peak position at many mole fractions, phase diagrams for the confined fluids were constructed, which gave a critical

weight fraction of 2,6-lutidine of $x = 0.32$ and a critical temperature of $T = 307.09$ K in pores of 100 nm size, as shown in figure 39. Additional measurements in a porous nickel sample (of very different pore topology) and average pore size of 250 nm, gave $x \simeq 0.30$ and $T = 306.86$ K.

These results were all interpreted in the context of finite-size scaling theory, and augmented by calculations on the three-dimensional periodically bound Ising model. The displacement of the temperature of the specific-heat maxima was described well by the finite-size scaling prediction of equation (25). Ising, porous glass, and porous nickel data all fit the same curve, with an exponent of $\nu = 0.64 \pm 0.02$. Furthermore, good agreement is found between the universal function F that describes the shape of the near-critical heat capacity, for all the systems studied. The authors conclude that the predictions of finite-size scaling theory are not dependent on the geometry of the specific porous media.

Sliwinska-Bartkowiak *et al* [336, 337] have studied the phase diagram of a mixture of nitrobenzene and *n*-hexane in CPGs using nonlinear dielectric effect measurements and light transmission. The nonlinear dielectric effect (NDE) is the change in electrical permittivity of the system due to a strong electric field; near the liquid–liquid critical point this quantity diverges with a critical exponent $\phi = \gamma - 2\beta$. When this mixture is confined in porous glasses with pore sizes of 100 nm and 150 nm, the (T, X) phase diagram is shifted to increased hexane concentrations, and the critical temperature is slightly depressed. This mixture has a type II phase diagram with an upper critical solution temperature (UCST), so this shift corresponds to a shrinking of the phase envelope. These effects are stronger in the sample with smaller pores, and in recent experiments on 7.5 nm porous glasses the depression is much larger, as shown in figure 40. As the temperature is lowered towards the critical point, the NDE value increases as it does in the bulk, with a comparable exponent, but in the region of the confined-system critical point the divergence is replaced with a rounded-off peak. These authors interpret this as a crossover from Ising-like behaviour to classical behaviour, arguing that once the correlation length of the fluid is comparable with the pore size the system enters a mean-field regime [241].

Light transmission measurements in this system [337] implied that the phase-separated mixture in the pores exists in a microscopic domain structure, at least on the timescale of these experiments. As the temperature is reduced, transmission of visible light through the sample drops off sharply at the confined critical temperature; in the bulk system similar behaviour is found at the bulk critical point. In the pore system, at lower temperatures the light transmission continues to decrease, while in the bulk system it returns to a high value just below the critical point. While the pore system is expected to quickly equilibrate on a small length scale, it may be that the two phases cannot globally phase separate in reasonable times, and the system becomes trapped in a state with many small domains of each phase alternating throughout the pore structure. In single-pore models, such alternating domain structures have been shown to have extremely long lifetimes [107, 242].

Other studies of liquid mixtures in large-pore glasses have revealed similar behaviour. Goldburg *et al* [116] used light scattering to study a mixture of carbon disulfide and nitromethane in a 100 nm porous glass. This mixture has an *upper* critical solution temperature of approximately 63.4 °C in the bulk phase. When confined in the porous glass, the critical temperature, as identified by a sharp change in the light transmission with temperature, is depressed to approximately 62.2 °C. In these experiments, the correlation length was found to not exceed 30 nm, so that the random-field hypothesis was not expected to apply at any temperature. The time autocorrelation function of the concentration fluctuations was found to have a non-exponential decay with a spectrum of relaxation times that can be as long as 100 s. In additional experiments on the porous sample immersed in bulk mixtures of various concentration, the form and timescale of the autocorrelation function were different from that

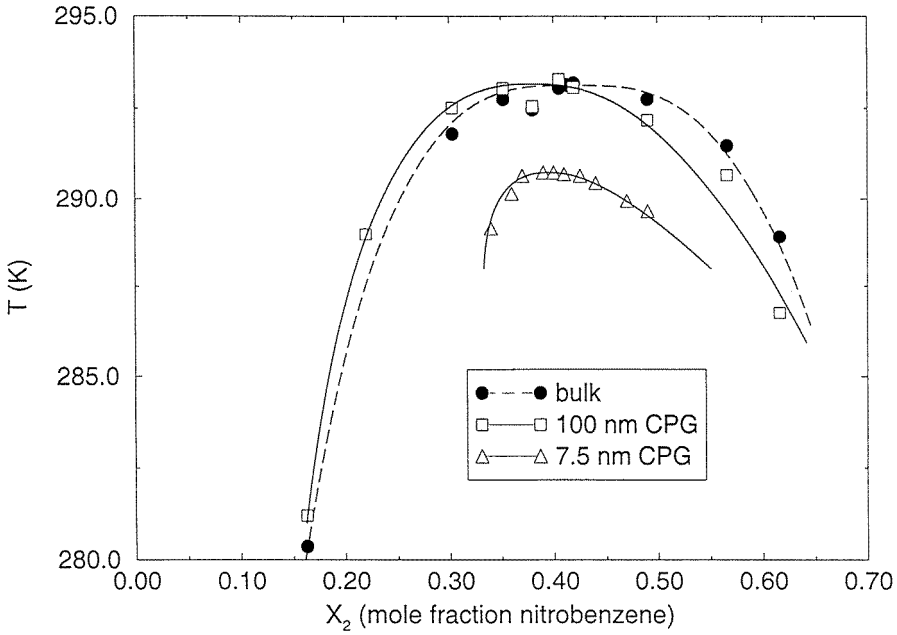

Figure 40. Coexistence curves of a nitrobenzene/*n*-hexane mixture in two different CPGs, compared with the bulk system. From [334].

of the isolated sample, and the confined fluid behaved much more like the surrounding mixture. A simple one-dimensional Brownian domain-diffusion model was described which captured many of the qualitative aspects of these dynamics.

Light scattering experiments have also been used to study the lutidine–water system in Vycor glass, which has an average pore diameter of approximately 7 nm and a porosity near 28%. Wiltzius *et al* [388] measured the phase diagram of this system by measuring the intensity of the Raman bands of lutidine in glass samples which had been exposed to bulk mixtures of various composition. The 'concentration shift' (enrichment of lutidine in the pores) varied between +0.15 weight fraction and −0.05 weight fraction, depending on the bulk concentration. The picture of phase separation proposed in this study involves two 'transitions'. As the system is heated from the one-phase region into the two-phase region, it undergoes a transition from a state in which lutidine is preferentially adsorbed (the finite-size analogue of 'complete wetting') to a state in which small domains rich in lutidine or water are present (the finite-size analogue of 'partial wetting'). This change is not abrupt, and is signalled by a change in the scattered light intensity. Once domains of each phase are formed, the correlation length in the system can grow to scales larger than the pore diameter, and a random-field transition is possible. An effective phase diagram for this transition was found by locating the divergence in the activation time for composition fluctuations. These data were fit to the standard form of the coexistence curve $|\phi_A - \phi_B| = B|T - T_c|^\beta$ (where ϕ is the weight fraction of one component), from which was extracted an *upper bound* for β of 0.21, smaller than the bulk value of near $\frac{1}{3}$, and in agreement with simulated and theoretical predictions for the random-field model. This study also found that far above the bulk separation temperature the system became cloudy, but no macroscopic phase separation was ever observed.

A later study of the same system with small-angle neutron scattering experiments came to somewhat different conclusions. Lin *et al* [201] obtained the structure factor $S(q)$ over a

large range of temperature and concentration for the water–lutidine mixture in Vycor glass. These data were then fit to standard predictions for the random-field model, which are generally similar to the scattering predicted for a collection of random domains. In order to obtain a good fit to the experimental data, an additional term was included to represent the scattering from an adsorbed lutidine-rich layer; the form of this term was determined by separate experiments on alkylsiloxanes attached to the Vycor surface. The conclusions of this study were that there was a surface layer rich in lutidine at all temperatures studied, and that the domain size (as defined by one of the fit parameters) never exceeds the Vycor pore size, even well above the critical temperature, deep into the two-phase region. This picture is consistent with the predictions of the single-pore model discussed above, and seems to represent a transition from the tube phase (at low temperatures) to a 'capsule' phase near the critical temperature.

5.1.3. Liquid crystal transitions. There have been many studies of liquid crystal transitions in controlled-pore and Vycor glasses and other porous materials. Most of these studies have focused on the transition between orientationally ordered (nematic) and disordered (isotropic) phases, with less attention paid to the orientationally and positionally ordered smectic phases. In the bulk phase, the nematic–isotropic (N–I) transition is weakly first order; the heat capacity has a strong peak at the transition temperature related to large fluctuations in the local orientational order parameter.

In confined systems the substrate material affects the local order through surface effects, by which molecules can be 'anchored' at the pore surface. This serves (in many cases) to increase the degree of order in the liquid crystal. The interaction of surfaces and liquid crystal phases has been extensively reviewed [159].

Conversely, 'geometric' confinement in a pore can either increase or hinder orientational and positional order, depending on the regularity of the pore structure and its compatibility with the bulk liquid crystalline structure. The pore geometry can either stabilize or destabilize smectic structures, and these effects are closely linked with the favoured orientation of the first adsorbed layer. Regular pore geometries can stabilize smectic structures, while locally rough surfaces can destabilize them.

Another effect of confinement in low-porosity materials is to separate the adsorbed fluid into weakly-coupled domains. Since the heat capacity peak (and strength of the transition) are related to large fluctuations in the local order, confinement broadens and reduces this peak in much the same way that it affects the susceptibilities of liquid–liquid mixtures near to their critical transitions. For sufficiently small pore sizes, surface interactions dominate over liquid properties and the sharp orientational transition disappears, replaced by a gradual loss of orientational order with increasing temperature.

In the bulk phase, the N–I transition is necessarily first-order because of the change in symmetry of the system. For porous networks with small pores, however, this need not be the case; because most of these materials are homogeneous and isotropic at large length scales, a confined nematic phase would also be *globally* isotropic in order to maintain locally favourable orientation throughout the network. That is, each section of pore would have its own preferred nematic director, but at larger scales these would average to zero. As in the case of adsorbed binary fluids, theoretical descriptions of these systems tend to focus either on a single-pore model, in which surface interactions and local geometry are considered [351], or random-field types of models, in which the system as a whole is studied, with the pore matrix taken as a random or semi-random perturbation of the adsorbed fluid [229].

Dadmun and Muthukumar [63] studied the N–I transition of *p*-azoxyanisole in a series of CPGs using differential scanning calorimetry, and showed that as the pore size was reduced from 313 to 16 nm the transition temperature first increased relative to the bulk phase and

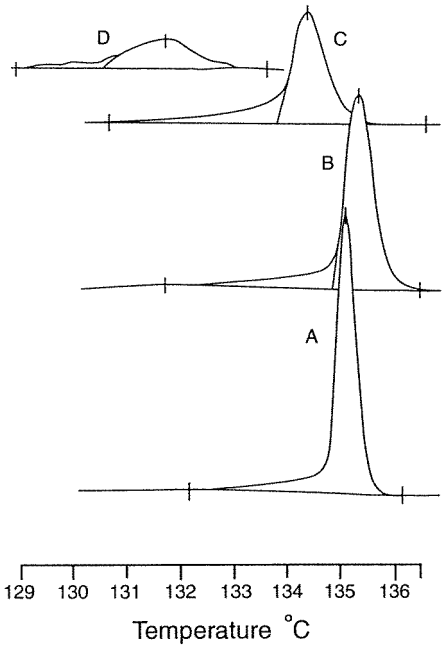

Figure 41. The DSC thermograms of the fully annealed systems. (A) Pure *p*-azoxyanisole (PAA), (B) PAA in CPG1, pore size 3125 Å, (C) PAA in CPG2, pore size 347 Å, and (D) PAA in CPG3, pore size 156 Å. The horizontal axis is the temperature in °C. Reproduced from [63].

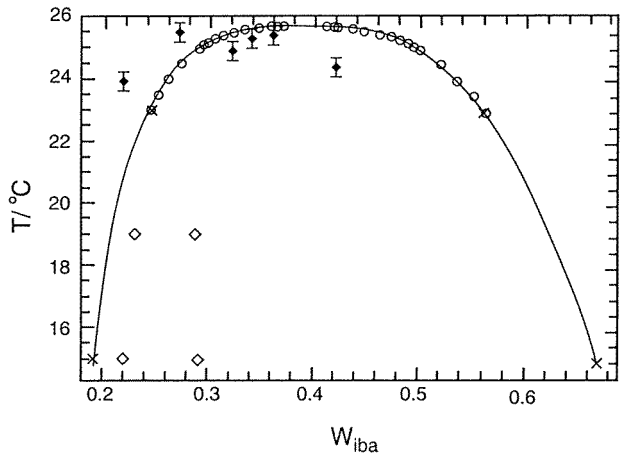

Figure 42. Temperature evolution of the absorption spectrum width for pentylcyanobiphenyl in 12 nm (+), 150 nm (□, path *b*; ×, path *a*), 200 nm (△) CPG, and for the bulk (◇) sample. The half-height widths are shown for the 12 and 150 nm samples (measured via path *b*) and the isotropic phase for all samples. The spectral half splittings are shown for the 150 nm (measured via path *a*), 200 nm and bulk samples in the nematic phase. The inset shows the details close to T_{NI}. Reproduced from [185].

then decreased, as shown in figure 41. For very large pores, the pore network structure has little effect on the liquid crystal, and the major effect of confinement is an enhancement of the nematic phase through surface-induced ordering. As the pore size is reduced, nematic order is still locally enhanced by confinement, but the directors in different parts of the network become decoupled, which overall weakens the nematic phase relative to the isotropic phase, and reduces the temperature of the transition.

Kralj *et al* [185] studied the liquid crystal pentylcyanobiphenyl in several CPGs using deuterium NMR. In samples with 150 and 200 nm radius pores, the transition remained bulk-like, with a discontinuity in the width of the adsorption spectrum near that found in the bulk phase. For a sample with 12 nm radius pores, the discontinuity was replaced by a continuous (though still relatively sharp) change from a somewhat less-ordered nematic state to the isotropic phase. Some of these data are shown in figure 42. This study concluded that far from the transition, in either phase, a single-pore picture was appropriate for these materials, while near the transition their results could be accounted for by introducing strong effects due to the junctions between pores. When the (different) directors in each pore section meet at a junction defects must occur. Because these junctions (in 12 nm radius pores) are of size comparable with the correlation length of the nematic phase, they may be responsible for the continuous nature of the transition, as no sharp transition could occur in such a volume. In the large-pore samples, the same geometric constraints on the director apply, but the junction volumes are much larger and allow for bulk-like behaviour.

Iannacchione *et al* [152] have used deuterium NMR and calorimetry to study the N–I transition of a number of liquid crystals in Vycor and CPGs. For octylcyanobiphenyl in large (100 nm) pores, they found that the nematic phase showed a NMR powder pattern spectra consistent with a locally ordered material with no overall preferred direction. This phase coexisted with an isotropic component. This liquid has a smectic-*A* phase as well, which was strongly suppressed relative to the nematic phase. For this liquid in 10 nm pores, no phase transition was detected, although there was a continuous variation of local orientational order with temperature. In Iannacchione *et al* [150, 151] several different liquid crystals in Vycor glass were studied with the same techniques; in all cases no real transition was found, with a strongly rounded remnant of the orientational transition occurring at a depressed temperature. In these studies Landau-type theories were successfully used to describe these data.

In anopore and nucleopore membranes with 200 nm diameter pores, Crawford *et al* [59] used deuterium NMR to examine the effects of confinement on the orientation of the liquid crystal 4'-pentyl-4-cyanobiphenyl, and found that the preferred orientation was along the axes of the cylindrical pores of the materials. The NMR spectral patterns were used to characterize the pore geometry of the two materials; the roughness of the pore surface was found to strongly influence the degree of order at temperatures above the bulk transition.

5.1.4. Helium transitions. The superfluid phase diagrams and near-critical behaviour of helium-4 (^{4}He) and mixtures of ^{3}He and ^{4}He have been measured in a variety of porous materials by Chan and co-workers. These fluids exhibit transitions to superfluid states at very low temperatures, and attracted a great deal of attention in bulk-phase studies as 'ideal' experimental realizations of critical transitions. Similarly, the confined helium systems are excellent experimental systems with which to study the effects of confinement. Some of the work in this area has been directed at measuring and characterizing the critical exponents of the superfluid transitions of *thin films* of ^{4}He [60, 92]; thin helium films adsorbed on Vycor glass show a crossover from two-dimensional-like to three-dimensional-like critical behaviour very near the superfluid transition. For temperatures far from critical, the films are described well by a modified Kosterlitz–Thouless approach, while near to the transition the correlation length becomes quite large (larger than the characteristic pore length), and a three-dimensional XY-type transition is found. Experiments on porous gold and hydrogen-plated gold reaffirm these findings, and show an additional peak in the heat capacity at temperatures significantly below the transition, which has yet to be explained [60].

Helium and helium mixtures have also been extensively studied in very high porosity aerogel materials. In the case of pure ^{4}He, adsorption in aerogels reduces the transition

temperature, with larger reductions for smaller porosities (higher gel densities.) In addition, as the gel density is increased, the heat capacity signature of the transition is more strongly rounded, when compared with bulk data [393]. For 5% gels, the heat capacity has no singular part below the transition, while for 2% and 0.5% gels it does; in general, as the percentage weight of silica in the gel is reduced the near-critical behaviour shows a smooth evolution towards the bulk limit [393].

In the case of ^{3}He–^{4}He mixtures, the effects of even low gel densities are striking. In the bulk phase, this system has a critical line which intersects a liquid–liquid coexistence loop at a tricritical point. In the pore system, the coexistence region is narrowed so that the critical line 'misses' it and continues down to very low temperatures; the topology of the phase diagram is completely changed [176]. This system has been modelled using the spin-1 Blume Emery–Griffths model with the silica framework described as a quenched random field; the tricritical point was found to be unstable under conditions pertaining to these experimental systems [228].

5.2. Lattice models

MacFarland *et al* [212] used large-scale Monte Carlo calculations to study the Ising model confined in a porous matrix comparable with CPGs. The matrices were produced using separate Monte Carlo simulations of the bulk Ising model with spin-exchange kinetics (conserved order parameter, with $M \equiv 0$); the bulk systems were quenched to subcritical temperatures, and the dynamic phase separation of the two phases was continued until the desired 'pore size' was reached. One phase was taken as the void space, and the other as the substrate. In this model, the void and substrate are entirely symmetric, which is not true in experimental Vycor, though it does hold for some other CPGs. In addition, the interaction between the confined Ising model and the substrate was that of a hard wall; no interaction energy was present between spins and the substrate. Sophisticated Monte Carlo sampling schemes were used to obtain critical temperatures and near-critical properties for many realizations of the porous matrix, and these data were analysed using finite-size scaling methods.

The principal conclusions of this study were that all of the data from all of the different pore systems studied *could* be collapsed together using simple scaling laws, and that all of their observations could be fit with a single set of critical exponents which were consistent with those of the *random Ising model* (also known as the 'site-diluted Ising model', not the same as the RFIM). These exponents were $\nu = 0.8 \pm 0.1$, $\gamma = 1.4 \pm 0.1$ and $\beta = 0.65 \pm 0.13$. While critical exponents are often difficult to measure precisely, these are quite different from those of the bulk Ising model. Since there were no surface fields in this model, the change in universality class appears to be due entirely to the effects of confinement. The dependence of these exponents on the degree of confinement was not measured.

Liu and Grest [203] and Monette [242] used kinetic Monte Carlo studies to support the single-pore model approach to confined liquid–liquid equilibria. These studies used a three-dimensional square cross-sectioned single-pore and spin-exchange Monte Carlo moves to investigate both the kinetics of domain growth and the effects of the pore surface field on domain topology. These studies provide examples of much of the behaviour predicted by the single-pore model. Upon quenching a system with weak surface fields from the disordered (supercritical) phase into a plug region, the domains of each phase grow quickly until the plugs are clearly visible, after which the dynamics slow drastically. The authors do not present quantitative domain-growth data; due to the small number of domains observed in these simulations, repeating these calculations many times would have been necessary for this. Additional simulations showed that upon quenching from the tube phase into the plug

phase, the appearance of plugs appears to be a nucleation-limited process. In simulations of a pore with stronger surface fields and a capsule phase, the transition between capsule and tube systems was also studied, and the rate of growth of capsules into tubes was found to be dependent on the thickness of the wetting layer.

The two-dimensional Ising model has been used in many studies of the effects of confinement on phase separation, with many different geometry 'pores'. Lee [198, 199] has studied a model with parallel pores separated by irregular, broken walls using kinetic Monte Carlo simulations of the type described above. In these studies the kinetics of phase separation were measured at both near-critical and sub-critical temperatures. These studies found very slow dynamics similar to those determined experimentally by light scattering, and support the hypothesis that some microscopic separation of the two phases begins at temperatures above the bulk critical temperature, induced by the correlated disorder of the pore system and the preferential attraction of the pore walls for one species. At sub-critical temperatures these studies found that static correlation data from systems with varying pore size could be fit with a single scaling function, provided that the correlation functions were measured using a minimum-distance convention.

For a one-dimensional system without a conserved order parameter, simulations of a simple 'kink–antikink' model predicted a logarithmic growth of domains upon phase separation [251]. Albano *et al* [3] tested this scaling using simulations of two-dimensional Ising 'strips' with no preferential surface field. They found that at short times, when the spin domain length scale was smaller than the strip width, the kinetics were very similar to those of the unconfined two-dimensional Ising model, and that at late times and large length scales, the system formed 'plug' phases where the growth of plugs was described well by a logarithmic law. Later simulations by Müller and Paul [250], however, indicate that this agreement with a logarithmic law may be spurious, and that at late times the domain growth could be completely described by an annihilating random-walk model, which predicts purely diffusive (power-law) domain growth. While non-conserved order parameter models are not applicable to binary liquid mixtures, they do describe single-component liquid–vapour coexistence, and can also be compared favourably with liquid crystal systems.

Kotelyanskii and Kumar [184] have carried out Monte Carlo simulations for an Ising model of an associating liquid mixture confined in a slit pore, with hydrogen-bond interactions between the fluid molecules and the walls. They find that the single liquid phase can be either stabilized or destabilized by the confinement.

5.3. Molecular simulation results

There have not been many molecular simulation studies of liquid–liquid phase equilibria in porous systems, and no studies based on realistic models of the experimental systems discussed earlier.

Most molecular simulation studies have focused on the kinetics of phase separation upon quenching, with only a few recent efforts at locating the phase diagram itself. Keblinski *et al* [168] used molecular dynamics to study the phase separation of a model LJ mixture in a slit-pore geometry at two slit widths (2σ and 3σ), allowing either one or two layers of adsorbed atoms. The fluid model is a symmetric LJ binary mixture with the attractive part (the dispersion term) of the inter-species potential turned off. This model mixture has been extensively studied in the context of bulk phase separation [190, 209]. This study found that the two-layer fluid showed good scaling in the radial distribution function, while the one-layer fluid did not. Furthermore, the domain growth exponent in the two-layer fluid was found equal to that from the author's earlier study [209]. The growth exponents were sensitive to

the simulation scheme used, with constant-temperature (canonical) simulations giving larger growth exponents than constant-energy (microcanonical) simulations.

These results have not been fully reconciled with other *strictly* two-dimensional simulations of the same mixture, which did find good scaling in the radial distribution function, provided that different growth exponents of $\frac{1}{2}$ and $\frac{2}{3}$ were allowed at short and long times, respectively [371, and references therein], presumably due to a crossover from diffusive domain growth to hydrodynamic domain growth. In these studies a slightly different potential was used, in which the sign of the attractive dispersion term between unlike species was reversed; this potential has a longer range than that used in the Keblinski study. However, the differences between strictly two-dimensional fluids and fluids physically confined to a single monolayer have not been systematically addressed, at least in this context, so comparison of these two studies may not be well founded.

Zhang and Chakrabarti [398] have studied the same binary LJ fluid as Keblinski *et al* in a variety of confined geometries in two and three dimensions. In their study of two-dimensional pores they investigated the kinetics of phase separation in 'strip' pores (the two-dimensional analogue of cylindrical pores) with pore walls that were either parallel or 'uneven'. They found that the phase separation followed a power-law growth with a low exponent (around 0.3) for short times, and then all but stopped once the domains of each phase were large enough to form plugs. In the uneven pores, which contained sections of larger pore radius, the phase separation continued for longer, with a late time crossover to a growth exponent of 0.64 ± 0.04, equal to the $\frac{2}{3}$ power law mentioned above. In a system that included a junction between two simple strip pores, domains were found to grow faster in the region of the junction, although no signature in the growth law was found. In a different study of a three-dimensional fluid in a cylindrical pore [396], the authors found striking qualitative evidence of the 'plug' phase proposed by Liu *et al* in the single-pore theory discussed above, although they did not locate a stable 'tube' phase. The pore system in this study was relatively short ($l = 69.6\sigma$ for a 8.7σ pore radius) which did not allow for the measurement of plug growth properties or size distributions, as only a few plugs could be observed.

Strickland *et al* [343] considered the dynamics of phase separation in a more realistic two-dimensional medium, for several wetting conditions. In this work the porous material was itself generated by a molecular dynamics simulation of bulk two-dimensional liquid–liquid separation; once the desired pore size was reached, one phase was frozen, while the other was split into a binary mixture. This study used a '12–3' LJ-type potential, also with completely repulsive forces between atoms of unlike species. For symmetric wetting conditions in which the pore surface does not prefer either component, plug configurations were observed at late times, while for the asymmetric system studied, in which one component was attracted to the pore wall and one was repelled from it, a capsule 'phase' was observed.

Góźdź *et al* [119] studied the phase diagram of a symmetric LJ mixture in ideal slit-pore geometries using the GEMC method. In this study the inter-species attractive well depth was lessened; $\epsilon_{12} = 0.65\epsilon_{11}$, which is sufficient to induce type II phase separation in this mixture, but gives substantially more diffuse (and realistic) liquid–liquid interfaces than observed in previous studies. The interactions between each fluid component and the pore wall were the same, so that the phase diagram was necessarily symmetric about $X = 0.5$; this allowed a modification of the Gibbs ensemble scheme in which only the 'identity' of particles need be exchanged between cells, as the cell densities can be held equal. Both the influence of the strength of the wall–fluid attraction and the pore size were studied. In this study the temperature was held fixed, and (ρ, X) sections of the phase diagram were measured. This study showed that *increasing* the potential well depth led to an increased critical density (at constant temperature), and that *decreasing* the pore width also increased the critical density,

apparently well into the solid-like region for very narrow pores.

Gelb and Gubbins [106, 107] have studied the kinetics of phase separation of the binary LJ mixture used by Góźdź *et al* in several different cylindrical pores. In these studies, the effective pore density was held constant, and the course of phase separation was followed for different temperatures and pore diameters. The systems used in these studies were all symmetric, and no capsule 'phases' were observed. In all cases, the phase-separating liquids reached plug conformations at late times. For deep quenches (to quench temperatures far below the critical point) the phase separation slowed dramatically when the domain size reached the pore diameter. For only slightly sub-critical quenches this was not the case, and the domains continued a power-law growth to the latest times studied, reaching average sizes of several pore diameters. The authors postulate that this temperature dependence is caused by large fluctuations in the liquid–liquid interface near the pore critical point, which in turn enable the diffusion of plugs of one phase in another. The motion of these domains was studied qualitatively in [106], and over the length of the simulation it does appear that domain growth is by a condensation mechanism.

Gelb and Gubbins [107] also considered the thermodynamics of their systems using a simple model of one-dimensional behaviour. Strictly speaking, the 'single-pore model' cannot have a true phase transition at nonzero temperature, for much the same reason that the one-dimensional Ising model cannot have one: the entropy associated with the position of the domain boundaries causes the system to favour many small plugs, rather than a few large ones. Using a histogram-weighted SGMC simulation they measured the probability distribution of the pore mole-fraction at sub-critical temperatures. A simple division of these probability distributions into 'one-phase' and 'two-phase' components allowed the calculation of the surface tension between adjacent plugs, and hence the average plug length as a function of temperature. The results of these calculations are shown in figure 43, supplemented by estimates of the average plug size from direct canonical Monte Carlo simulations; they indicated that the average plug length was extremely large except quite close to the critical point, and that none of the molecular dynamics simulations had reached a thermodynamically stable state, by at least an order of magnitude in plug length.

In a later study these authors used the same histogram-based methods to study the phase coexistence properties of strongly asymmetric systems [108]. Three different strengths of wetting potential were studied, with wall–fluid well-depth ratios $\epsilon_{2w}/\epsilon_{1w}$ of 3:1, 2.2:1 and 1.67:1, in cylindrical pores of 5σ radius. The phase coexistence curve in the (T, X) plane was shifted towards the more strongly adsorbed component, and the pore critical temperature (as extrapolated from lower-temperature data) was depressed, with both effects being most pronounced for the 3:1 system, as expected. These data are shown in figure 44. Simulation snapshots showed that the coexisting phases were a nearly pure phase of the preferred component and a tubular phase in which the preferred component wet the wall and the non-preferred component occupied the centre of the cylinder. Thus, these coexistence curves could be interpreted as a coexistence between complete-wetting and partial-wetting states. The authors also investigated the effects of the finite-size periodic boundary conditions used in the simulations, and determined that, while the qualitative behaviour of the systems did not change with increasing system *length*, the $P(X)$ distributions and the shape of the top of the phase diagram were quite sensitive, underlining the difficulties of using small ideal-geometry systems for the investigation of near-critical phenomena.

5.3.1. Liquid crystal simulations. There have been many simulation studies of liquid crystals in confined geometries, using both lattice-based models and more sophisticated off-lattice potentials.

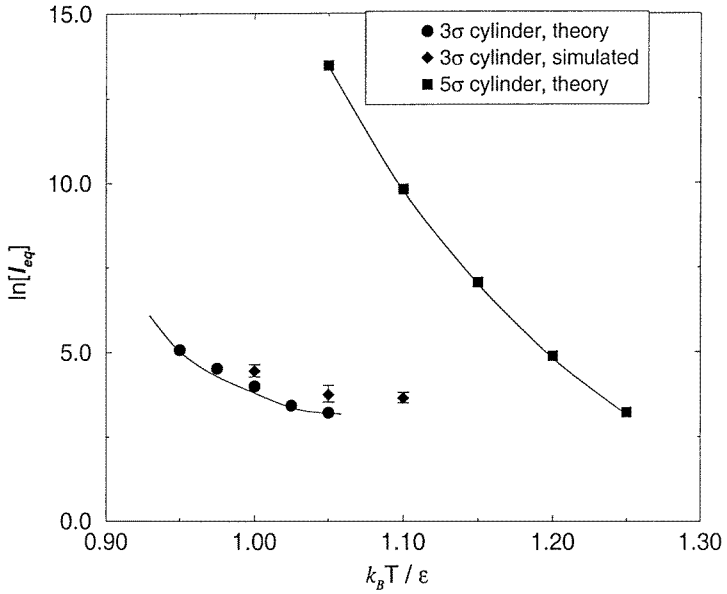

Figure 43. Results from histogram analysis for the equilibrium domain length, l_{eq} (reduced with molecular diameter σ_{ff}) in cylindrical pores of radii 3σ and 5σ, and from direct Monte Carlo simulation of the equilibrium domain length in the 3σ system, over a range of temperature. Potential parameters are chosen to model argon in pores of carbon dioxide. Reproduced from [106].

Telo da Gama *et al* [351] solved a Lebwohl–Lasher model with both simulations and approximate methods to locate the N–I phase transition for a liquid crystal confined in a slit pore at many pore widths. This model consists of rotors fixed to a cubic lattice, interacting through nearest-neighbour potentials based on $P_2(\cos\theta)$, where θ is the angle between rotors and P_2 is the second Legendre polynomial. They found that the Kelvin prediction, that the shift (downwards) in the N–I transition temperature is proportional to $1/L$, where L is the pore width, is accurate for $L \geqslant 64$ layers. In addition, for wide enough pores a wetting layer of the isotropic phase was observed at each wall; in this system the walls did not exert any ordering potential on the fluid model, so that orientational order was greater in the centre of the pore than at the wall. A subsequent study of the same model [53] also considered the effects of an aligning surface field and simulation system size. For zero field, they concluded that the film (pore) has a critical thickness $8 < L_c < 16$ below which no phase transition occurs. Chiccoli *et al* [50] used Monte Carlo simulations of this type of lattice model to study the effects of confinement in a slit pore with two different surfaces that preferred normal and tangential orientations of the molecules, leading to complicated defect structures in the film. Zhang and Chakrabarti [397] used a two-dimensional Lebwohl–Lasher model in a complex tortuous model of Vycor glass to show that the ordered phase breaks into many nematic domains with independent directors, as argued from experimental studies. Measurements of the order parameter relaxation in this study were consistent with predictions based on random-field models.

Most molecular simulations of liquid crystals have used the Gay–Berne potential [103] to model the fluid. The liquid crystal in contact with a graphite surface has been shown to have a highly ordered surface layer oriented normal to the surface, while the second and higher layers are much less strongly ordered [276]. In addition, the rate at which the surface-induced order decays away from the surface depends on the orientation of the bulk nematic director.

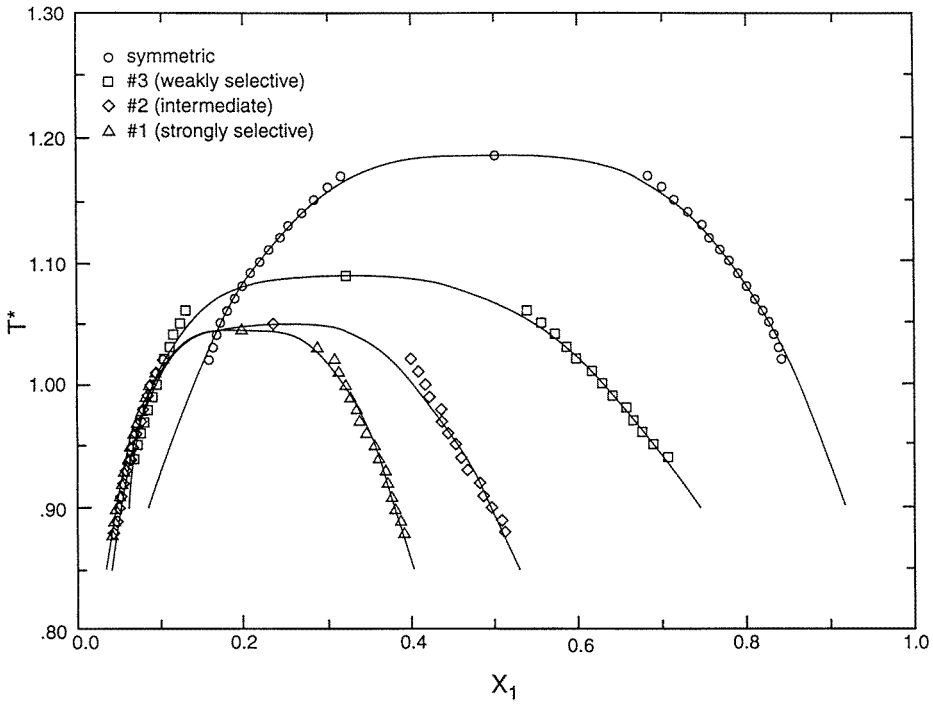

Figure 44. (T, X_1) phase diagrams for the symmetric LJ system and asymmetric systems #1, #2 and #3. These have values of $\epsilon_{2w}/\epsilon_{1w}$ of 3.0, 2.3 and 1.67, respectively. Points are simulation data (except for the estimated critical points) and curves are fits to the Ising lattice-gas form. Reproduced from [108].

Wall and Cleaver [377] studied the Gay–Berne fluid between two graphite-like walls with anisotropic substrate–fluid potentials, and found that the surface layers tilted slightly; this tilt was propagated through the entire film. At lower temperatures layered (smectic) structures were observed and the tilt angle changed considerably to accomodate this; the degree of tilt in the smectic phases was found to be dependent on the strength of the surface–fluid interactions, which was not the case for the nematic fluids. Gruhn and Schoen [124, 125] studied a confined fluid given by a modified Gay–Berne potential with a different pore–wall model and many different pore widths, showing that the normal stress (across the pore) changed in a complex oscillatory sequence as the pore width was increased, due to changes in the number of smectic layers and the compression (axial tilt) of each layer.

6. Freezing

Improved understanding of confinement effects on freezing are essential in areas relating to lubrication, adhesion and fabrication of nanomaterials and nanotribology. In addition, these studies can provide insight into mechanisms involved in frost heaving and distribution of pollutants in soils. Freezing in porous media has been widely employed in the characterization of porous materials. In the method termed thermoporometry, the shift in freezing temperature of water is determined, and the PSD is inferred from a thermodynamic analysis which is analogous to the use of Kelvin equation for capillary condensation.

In this section we focus on theoretical and experimental studies of freezing and melting

behaviour in completely filled, well-characterized porous systems. Various experimental techniques used to measure freezing temperature as well as structure of the condensed phases inside pores are briefly described. The effect of pore size and the nature of the fluid–wall interaction, as well as various methods to calculate the free energy of the confined phases, are discussed. Other important aspects of freezing in confined systems that are not discussed in this review include freezing of monolayers on a substrate, commensurate–incommensurate phase transitions, freezing of quantum fluids, and solid–solid transitions in pores. Some of these topics warrant separate reviews by themselves and are discussed elsewhere [18,127,321]. We note that DFT has been widely successful in addressing freezing transitions in the bulk. However, little progress has been made in extending this to freezing of confined fluids. Some of the early attempts in this direction are reviewed by Henderson [140].

6.1. Experiments on freezing/melting

Freezing of oxygen in sol–gel glasses was studied by Warnock *et al* [379] by a sub-picosecond optical technique. In this method, the optical pump pulses were used to create a birefringence, that occurred due to the rotational motion of the molecules in the liquid, and the subsequent molecular orientational relaxation time was measured. A change in the value of the relaxation time was used as an indicator of the freezing temperature. The freezing temperature in the confined system was always depressed as compared with the bulk; the shift was larger for smaller pores, and as large as 10 K for the smallest (20 nm) pore (figure 45). Unruh *et al* [364] examined the melting behaviour of indium metal in porous silica glasses by differential scanning calorimetry (DSC) measurements, and reported a large depression in melting point due to confinement (see figure 45). Other experiments that used porous silica glass as the confinement medium also found a decrease in the freezing temperature, T_f, as compared with the bulk [36, 74, 129, 186, 240, 245, 272, 335, 339, 342, 350, 358].

The simplest way to understand this behaviour is through a classical thermodynamic argument that determines the freezing temperature, T_f, as the point at which the chemical potential of the solid core inside the pore equals that of the surrounding fluid†. The shift in the chemical potential due to the presence of the pore wall can be determined along the same lines of the Kelvin equation for gas–liquid condensation [260]. It is then easy to show that (see, e.g., [82]),

$$\frac{\Delta T_f}{T_{fb}} = -2\frac{(\gamma_{ws} - \gamma_{wl})\nu}{H\lambda_{fb}} \tag{26}$$

where T_{fb} is the bulk freezing temperature, γ_{ws} and γ_{wl} are the corresponding wall–solid and wall–fluid surface tensions, ν is the molar volume of the liquid, λ_{fb} is the latent heat of melting in the bulk and H is the pore width. Equation (26) is sometimes referred to as the Gibbs–Thomson equation. The sign of $\Delta T_f = T_f - T_{fb}$ depends on whether the walls prefer the solid or the liquid, i.e. whether γ_{ws} is greater or less than γ_{wl}. The observed depression in the melting temperatures varied as $1/H$ in the above-mentioned studies, and were thus consistent with equation (26) down to pore sizes as low as 6 nm (figure 45). However, this type of classical thermodynamic argument breaks down for small pores, for reasons that are analogous to those that lead to the breakdown of the Kelvin equation (section 3.2.1).

One can go further along the same lines to show that the latent heat of the confined solid is related to that of the bulk solid by

$$\lambda_{fp} = \frac{T_f}{T_{fb}}\lambda_{fb}. \tag{27}$$

† Other approaches that lead to the same equation involve balancing the bulk, surface and interfacial components of the excess free energy (see [379]).

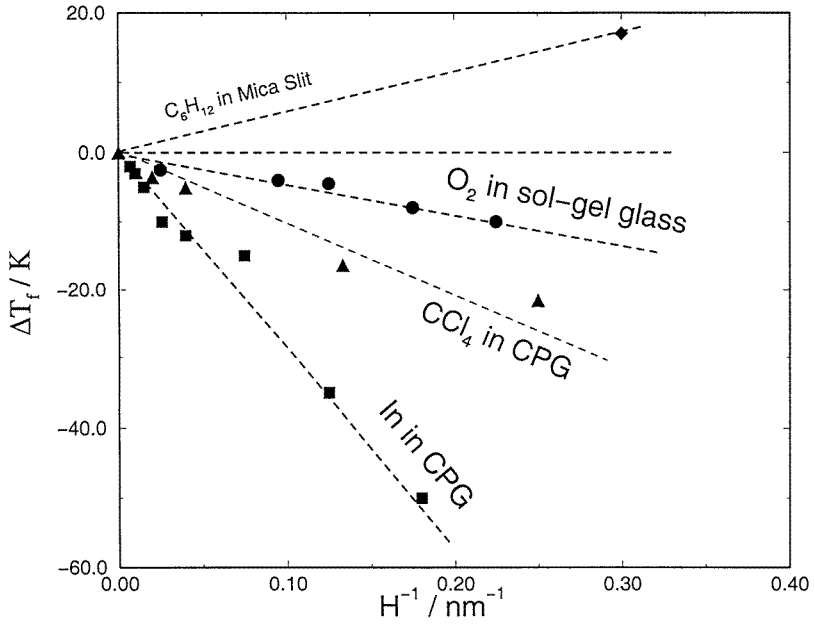

Figure 45. Shift in freezing temperature from experiment: O_2 in sol–gel glass [379], indium in CPG [364], cyclohexane between mica plates in a surface force apparatus [180], CCl_4 in CPG [335]. The dashed lines are a guide to the eye.

Unruh *et al* [364] and Molz *et al* [240] reported latent heat measurements in the confined systems that were less than the bulk values, but the magnitude of λ_{fp} was much less than the value predicted by equation (27). For example, in the case of indium in silica, the latent heat in the bulk is 28.5 J g^{-1} and the latent heat in an 8.2 nm pore glass was measured to be 10.2 J g^{-1}, while that predicted by equation (27) is 26.3 J g^{-1}. These differences were attributed to the premise that, in a pore the first few molecular layers close to the pore wall (contact layer) remained amorphous, while the interior froze to a crystalline form.

There have been experimental reports that investigated the structure of the confined phases through NMR and x-ray diffraction techniques, that corroborate the above hypothesis. Overloop and Gervan [272] studied freezing of water in porous silica using NMR, and they suggest that in the confined solid phase up to three molecular layers adjacent to the pore wall (which they term 'bound water') have a structure that is different from the crystal phase and from that of the free liquid. The rest of the water molecules in the pore interior were in the form of cubic ice (I_c) and the freezing temperatures were consistent with equation (26). The study also indicated a distribution of the molecular correlation times associated with translation and rotation in the bound water phase, with the values lying in a range that was inbetween the liquid and the crystal phases. Morishige and co-workers [244, 245] used x-ray diffraction to study water in siliceous MCM-41 having a range of pore sizes, and also confirmed the existence of a disordered layer of water molecules near the pore wall, with the inner region being the I_c phase. Morishige and Kawano [244] also studied water in Vycor glass and found evidence for both the cubic I_c phase as well as the ordinary hexagonal (I_h) phase. Baker *et al* [9] studied the nucleation of ice in sol–gel silicas and MCM-41 and found that the crystal structure depends strongly on the conditions and nature of the porous material, showing characteristics of both I_h and I_c forms. X-ray diffraction studies of water in activated carbons suggested an increase

in the freezing temperature due to confinement [153, 154]. Morishige and Kawano [244] have reviewed other experimental studies of the freezing/melting behaviour of water in porous silicas and glasses.

In a recent study, Booth and Strange [36] examined the melting of cyclohexane in porous silica using the NMR technique. The melting temperature was below the bulk melting point, and in the confined solid phase there were two distinct components of the transverse relaxation time. The short component (15–30 μs, comparable with the crystal phase in the bulk) was attributed to the crystal phase in the interior of the pore, and the long component was attributed to a liquid-like contact layer. Further lowering of temperature led to the freezing of the surface (contact) layer as well.

Sliwinska-Bartkowiak *et al* [335] attempted to characterize the melting/freezing transition for a dipolar fluid, nitrobenzene confined in CPG of different pore sizes, using DSC and dielectric relaxation spectroscopy. The depression in the melting temperature followed equation (26) for pore sizes larger than 7.5 nm; however, significant deviation was observed for a smaller pore width. The results from both experiments were in good agreement. The authors also made a quantitative estimate of the rotational relaxation time in the fluid and crystal phases by fitting the complex permittivity $\epsilon^* = \epsilon'(\omega) - \mathrm{i}\epsilon''(\omega)$ measurements to the Debye dispersion equation. In addition to the liquid and crystal phase relaxation, a third relaxation component was observed, that supported the existence of a contact layer with dynamic properties that were more liquid like than the inner layers as found in the previous studies.

The experiments described so far show a decrease in melting/freezing temperature in the pore, which seems to indicate that for the set of chosen fluids and porous materials, the wall always prefers the liquid phase to the solid phase. Alternatively, this can be viewed as the fluid–wall interaction being weak relative to the fluid–fluid interaction. The term $-2(\gamma_{ws} - \gamma_{wl})v/H$ in equation (26), can be interpreted as the difference between the actual wall–solid potential energy and the wall–solid potential energy, that would occur if the wall were made up of the adsorbed solid itself. Moreover, for this type of fluid–wall interaction, it appears that the first few layers of the confined solid phase melt at a temperature lower than the depressed melting temperature in the interior of the pore.

In view of this large body of experimental evidence for a decrease in the freezing temperature due to confinement, it is tempting to assume that a decrease always occurs. However, in 1995 an experimental study of cyclohexane and octamethylcyclotetrasiloxane (OCTMS) between parallel mica surfaces in a surface force apparatus provided evidence of *an increase* in freezing temperature in confined systems [180]. In this study, Klein and Kumacheva start from a confined liquid phase and slowly reduce the separation between the mica surfaces. At a separation close to about seven molecular diameters, the liquid freezes abruptly, which they monitor through viscosity measurements. At this separation the increase in the freezing temperature for cyclohexane was about 17 K (figure 45). Similar studies have been reported in a surface force apparatus (with mica surfaces) for linear alkanes [120, 146] and cyclohexane [181], and again show an increase in the freezing temperature. This increase is believed to be due to strong attraction between the confined fluid molecules and potassium in the mica surface. In a subsequent molecular simulation study of the effect of confinement on freezing of simple fluids in slit pores [238] it was shown that T_f was strongly affected by the strength of the attractive forces between the fluid molecules and the walls (see section 6.2). For strongly attracting walls such as carbons, an *increase* in T_f was predicted. Moreover, the increase in T_f was predicted to be larger for slit than cylindrical pores [219]. Recently, experiments on the freezing of CCl_4 in activated carbon fibres by Kaneko and co-workers [380], have indicated a large upward shift in freezing temperature of about 56 K in nanopores of diameter 0.7–1.2 nm (figure 46). Similarly, a large increase in the freezing temperature for

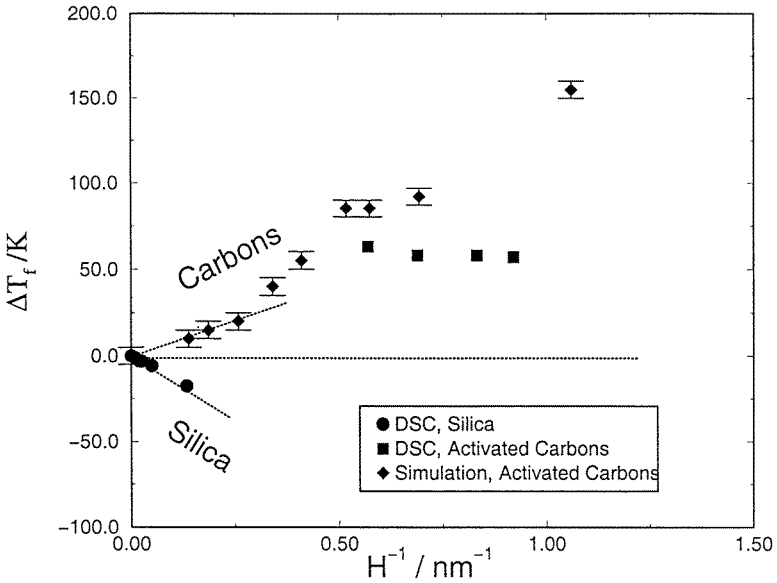

Figure 46. Shift in freezing temperature for CCl_4 from experiment and simulation. For the same adsorbed fluid CCl_4, the direction of the shift depends on the nature of the fluid–wall interaction; a positive shift observed in the case of attractive (graphite) pores and a negative shift observed in the case of porous silica. The plot also shows evidence of a deviation from linearity in ΔT versus $1/H$ in the microporous regime. From [305, 335, 380].

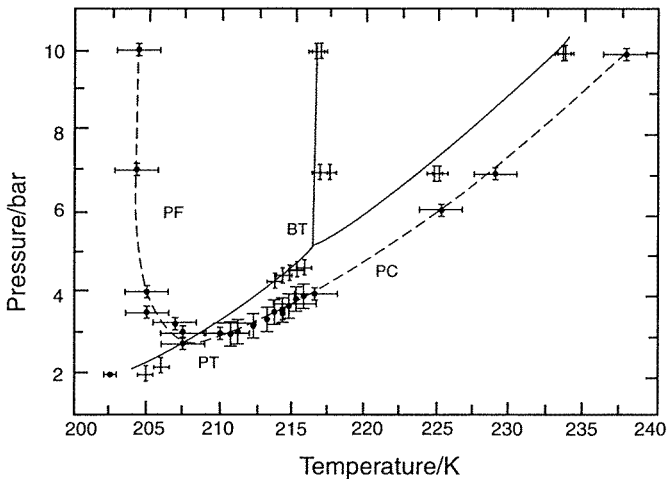

Figure 47. Phase diagram of CO_2 in Vycor glass: the crosses and the solid curves refer to the bulk system while the symbols (●) and the dashed curves refer to the confined (pore) system. Dashed curves, labelled PC (pore condensation) and PF (pore freezing) are a guide to the eye. BT denotes the bulk triple point while PT refers to the 'quasi-' triple point of the pore fluid. From [70].

benzene in activated carbon fibres has been reported by Watanabe and Kaneko [381]. There have been other experiments of simple fluids such as methane on single graphite substrates [48] which have indicated a 10% increase in freezing temperature for the first molecular layer of methane adjacent to the graphite wall (contact layer).

The above studies did not attempt to determine a detailed phase diagram for the confined fluid. However, Duffy *et al* [70] used the positronium annihilation spectroscopy to map out the complete phase diagram (figure 47) for CO_2 in Vycor glass with a mean pore diameter of 70 Å. The confinement shifts the liquid–solid transition to a considerably lower, and the gas–liquid transition to a considerably higher temperature than in the bulk. The triple point is reduced both in pressure and temperature from that of the bulk. The positron annihilation spectroscopy studies, while providing information on the location of the phase transitions, do not provide any information on the microscopic structure of the confined solid phase. Brown *et al* [43] reported studies of the microscopic structure of the confined solid CO_2 adsorbed in porous Vycor glass using x-ray diffraction. Their study concluded that the confined CO_2 solidifies into crystallites with average dimensions of 160 Å, with a structure that is consistent with the *Pa3* structure (which is an fcc lattice with molecules oriented along the diagonals of the cubic lattice) of bulk CO_2. The average crystallite size of the solid phase of the confined CO_2 is comparable with the pore dimensions in Vycor indicating that the solidification occurs separately in each of the pores. However the unit-cell size for the confined solid is larger than what has been observed in the bulk at the same temperature, indicating a less dense solid in the pores. Also a significant amount of disorder was observed in the arrangement of the molecules which could not be accounted for with the Debye–Waller effect.

6.2. Simulation studies: simple pore geometries

6.2.1. Melting and freezing studies. Schmidt and Löwen [324] studied the freezing of hard spheres confined between two parallel hard plates for various plate separations, interpolating between two and three dimensions, using Monte Carlo simulation. The co-existence conditions were obtained by identifying van der Waals loops in pressure versus density curves, and then applying a Maxwell construction. The full phase diagram for this model was mapped out for arbitrary density and plate separations lying between one and two sphere diameters (figure 48). The phase diagram is found to exhibit a rich structure with a fluid phase and many different solid phases of buckled, layered and rhombic crystalline structure. For the finite system sizes studied, the freezing was found to be first order, which was followed by a further solid–solid transition as the density was increased. Some of the solid–solid transitions were found to be weakly first order. These findings can be verified in principle, by performing experiments with colloidal suspensions between parallel plates.

Detailed and systematic simulations aimed at qualitative comparison with the experimental data were made by Miyahara and Gubbins [238] who studied freezing in slit-shaped pores and Maddox and Gubbins [219] who studied freezing in cylindrical pores. The adsorbate was a LJ fluid, and various pore sizes and choices of wall–fluid potential functions were investigated. Miyahara and Gubbins [238] used GCMC simulation, and found that for the case of LJ-methane confined in a hard wall pore the freezing temperature was significantly lower than in the bulk, whereas for strongly attracting walls (modelled on graphite), there was a significant increase in the freezing temperature (figure 49). In addition, the contact layers (the molecular layers adjacent to the two pore walls) behaved differently than the rest of the fluid. For example, the contact layers appeared to freeze at a different temperature than the rest of the fluid in the pore; the freezing temperature was higher than that of the bulk material for the case of attractive walls, and lower for the case of repulsive walls. Maddox and Gubbins [219] used a novel simulation method that combined GCMC simulations with molecular dynamics for better relaxation of the displacement moves for LJ molecules in cylinders. They reached similar conclusions about the nature of the freezing-point shifts, but found important differences because of the increased confinement in a cylindrical geometry. In particular, the additional confinement led

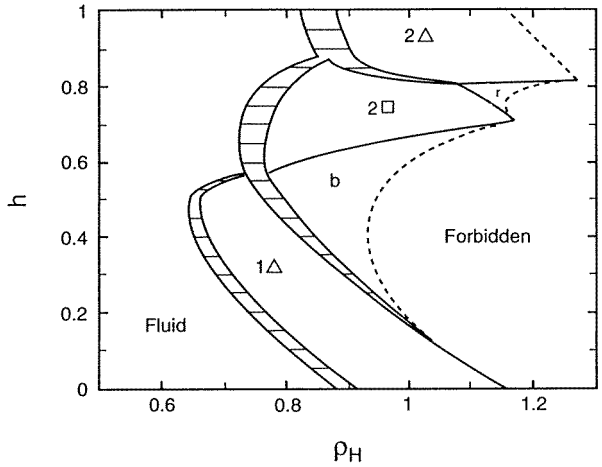

Figure 48. Simulated phase diagram for hard spheres of reduced density ρ between parallel plates with effective reduced separation h. Here $h = (H - \sigma - \sigma_w)/\sigma$, where σ and σ_w are the diameters of the hard sphere and wall molecules, respectively, and H is the pore width as measured between the planes through the centres of the atoms in the first layer of each opposing pore-wall. Six phases occur (fluid; 1△: triangular lattice with one layer; b: crystalline structure of buckled lines; 2□: square lattice with two layers; r: rhombic phase; 2△: triangular lattice with two layers). The closed packed density is marked by a dashed line. Solid curves are guides to the eye. Thin horizontal tie-lines represent two-phase co-existence. From [324].

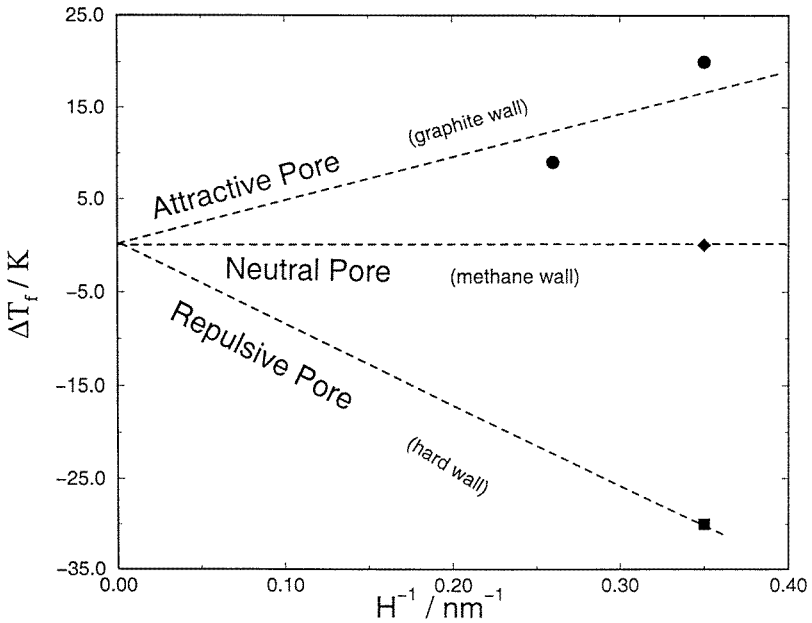

Figure 49. Shift in the freezing temperature from simulation. The symbols show the shift in the freezing temperature of LJ methane in three different pores of pore width $H = 7.5\,\sigma$, σ being the LJ size parameter for methane. The attractive pore was modelled on graphite, the neutral pore consisted of an artificial methane wall and the repulsive pore consisted of two hard plates. The dashed lines are a guide to the eye. From [238].

to downward shifts in the freezing temperatures when compared with confinement in a slit geometry. Miyahara *et al* [239] also studied the effect of the pressure of the equilibrium gas phase on the melting temperature of the confined liquid phase using a innovative simulation setup. They found that, while the solid–fluid co-existence line in a P–T diagram for the confined system remained vertical above the bulk saturation pressures, there is significant variation of the melting temperature with pressure for the confined system for pressures lower than the bulk saturation pressure, which is very different from what is observed for the bulk system. This observation is consistent with the experimental report of the CO_2 phase diagram in Vycor glass that was discussed earlier [70].

These simulation studies made use of pair correlation function and structure factor plots, together with snapshots of molecular configurations to monitor the freezing process. These were also verified by applying the Hansen–Verlet criterion [130, 308] and calculation of self-diffusion coefficients. The findings provide a detailed understanding of the freezing/melting behaviour observed in the experiments. However, a limitation of the simulation studies was that the precise location of the phase transition was not found. The freezing and melting displayed large hysteresis loops, and thus the location of the equilibrium freezing/melting point could be estimated only to the accuracy of the width of the hysteresis loops which often spanned 10–30 K. The nature of the transition was also not clear, as the results of the behaviour in smaller pores suggested a continuous rather than a first-order transition. Answers to these issues lie in a detailed and explicit calculation of the free energies of the phases involved in the phase transition.

6.2.2. Free-energy methods. In an attempt to address the problem of locating the true transition point, Dominguez *et al* [69] used thermodynamic integration [97] to calculate the free energy of the solid and fluid phases in the pore. This method involves a numerical integration of the Gibbs free energy starting from a known reference phase (the Einstein crystal for the solid phase and the ideal gas for the liquid phase) to the state point of interest. It relies on finding a suitable path of integration which is thermodynamically reversible, i.e., the path must not intersect any phase boundary characterized by a first-order transition. The Gibbs free energy was calculated for the case of purely repulsive and weakly attractively pores and the location of the thermodynamic transition temperature was found. Their results also indicated that the transition was first order. In addition, the authors calculated the condensation line and mapped out the complete phase diagram for weakly attractive pores (figure 50). The behaviour of fluids in attractive and repulsive pores was found to be consistent with the study in Maddox and Gubbins [238].

The free-energy study of Dominguez *et al* [69] was limited to confined systems with repulsive or weakly attractive wall–fluid potentials. For the more ubiquitous case of a wall–fluid potential that is moderately or strongly attractive, this method breaks down. This is because the adsorbed molecules adjacent to the pore–wall (the contact layer) freeze before the adsorbed molecules in the interior of the pore. This makes it impossible to find a reversible path from the ideal gas phase to the fluid phase, since any such path runs into a first-order transition corresponding to the freezing of the contact layer.

To overcome this difficulty, Radhakrishnan and Gubbins [303] used a method based on an order parameter formulation to calculate the free energy. They used GCMC simulations on a system similar to that studied by Miyahara and Gubbins [238]. The method relies on calculation of the Landau free energy as a function of an effective bond orientational order parameter Φ. The Landau free energy can be defined through the equation [189],

$$\Lambda[\Phi] = -k_B T \ln(P[\Phi]) + \text{constant} \tag{28}$$

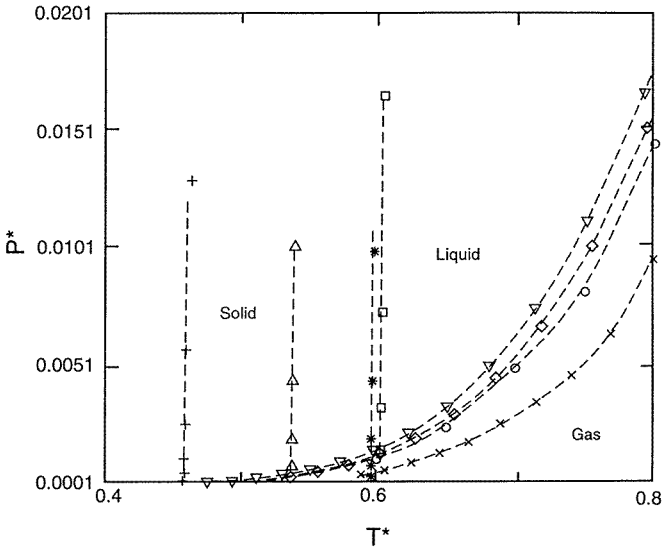

Figure 50. Coexistence curves for confined and bulk LJ fluid in slit pores of width $H = 10\sigma$. Note that for the pore, P denotes the normal pressure P_z, whereas for bulk it is the bulk pressure. The symbols represent,

Bulk	○ liquid–gas	□ liquid–solid	
Repulsive wall	◇ liquid–gas	△ liquid–solid	$N = 600$
Repulsive wall	▽ liquid–gas	+ liquid–solid	$N = 300$
Weakly attractive wall	× liquid–gas	∗ liquid–solid	$N = 300$

where N is the number of molecules used in the simulation. From [69].

where $P[\Phi]$ is the probability of observing the system having an order parameter value between Φ and $\Phi + \delta\Phi$. The probability distribution function $P[\Phi]$ is calculated in a GCMC simulation by collecting statistics of the number of occurrences of a particular value of Φ in the form of a histogram, with the help of umbrella sampling [359]. The grand free-energy Ω, is then related to the Landau free energy by,

$$\exp(-\beta\Omega) = \int \mathrm{d}\Phi \, \exp(-\beta\Lambda[\Phi]). \tag{29}$$

This approach comes under the general classification of histogram re-weighting methods discussed in section 2, and was first used to study solid–fluid transitions in the bulk by Van Duijneveldt and Frenkel [368] and Lynden-Bell *et al* [208]. It can be used sucessfully for the case of strongly attractive walls, as well as weakly attractive and repulsive ones, and is not affected by phase changes in the contact layer. The method requires the choice of an order parameter that is appropriate for the system of interest [303]. For example, for a three-dimensional system a combination of the spherical harmonics of the orientation of the nearest-neighbour bonds is suitable.

The Landau free-energy results of Radhakrishnan and Gubbins [303] for LJ methane in an attractive graphite pore showed that there are three phases for such a system (figure 51); phase A corresponds to all the layers having a liquid structure (figure 52(*a*)), phase B corresponds to the contact layers (the layers adjacent to the two pore walls) being frozen and the rest of the layers having liquid structure (figure 52(*b*)), and phase C corresponds to all the layers being frozen. A plot of the grand free energy for each phase as a function of temperature gave the freezing point for the contact layers as well as for the inner layers, and clearly indicated that both transitions

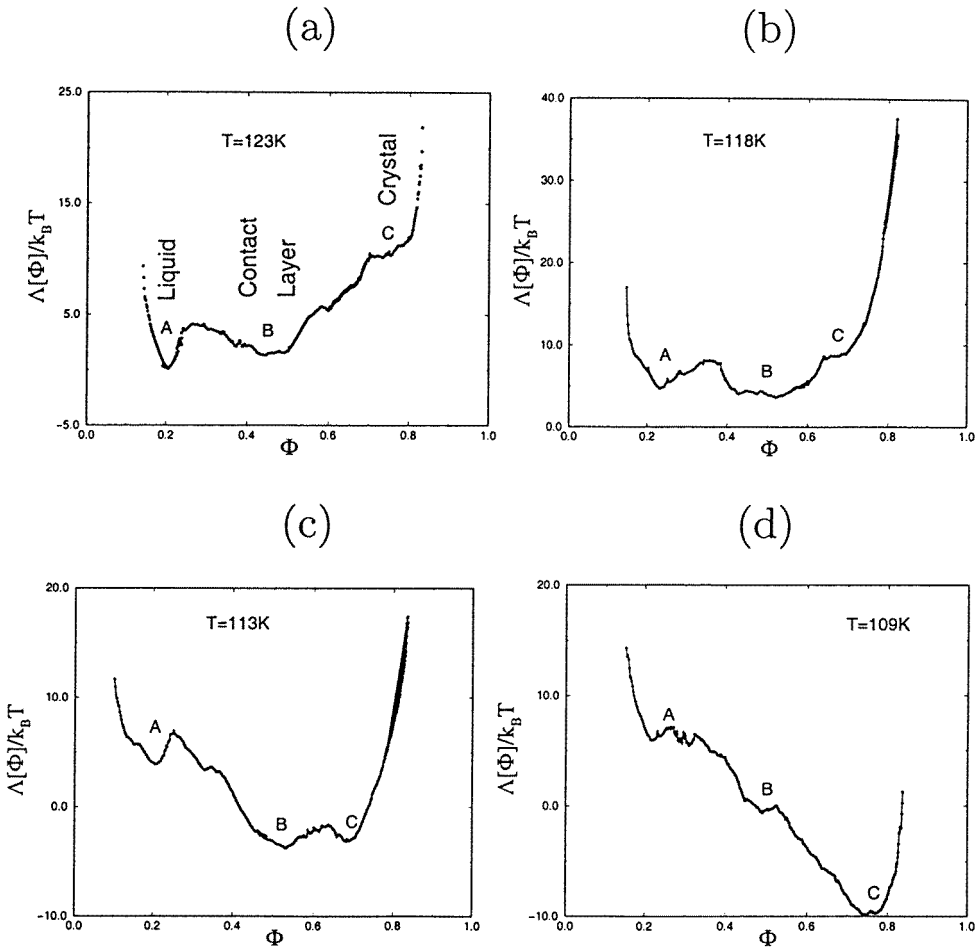

Figure 51. The Landau free energy as a function of the order parameter, for methane confined in a graphite slit pore of width 7.5σ, for (*a*) $T = 123$ K, (*b*) $T = 118$ K, (*c*) $T = 113$ K and (*d*) $T = 109$ K; the relative depths of the minima indicate the stability of each phase. From [303].

were first order (figure 53). We note that the freezing temperature for LJ methane in the bulk is 101 K. Transition temperatures in the pore are well above this value. Radhakrishnan and Gubbins also found strong evidence for a liquid to hexatic transition prior to freezing in the LJ methane/carbon system. They attributed the relatively weak first-order nature of the freezing transition in this system to the large entropy loss associated with this liquid–hexatic transition prior to freezing. The order parameter method can be applied to weakly attractive or purely repulsive walls [303]. In this latter case there is no evidence of a hexatic phase, and the freezing transition is strongly first order.

The effect of the fluid–wall interaction on the freezing behaviour has been investigated for a slit pore model along with the '10–4–3' Steele potential, by a systematic study of the Landau free-energy surfaces as a function of the relative strengths of the fluid–wall to the fluid–fluid interaction, given by $\alpha/\epsilon_{ff} = \rho_s \epsilon_{sf} \sigma_{sf}^2 \Delta/\epsilon_{ff}$ in equation (14) [304]. For weak wall strengths, $\alpha/\epsilon_{ff} < 0.5$, the Landau free-energy function showed just two minima, corresponding to a liquid and a solid phase, the intermediate phase being metastable. For intermediate wall

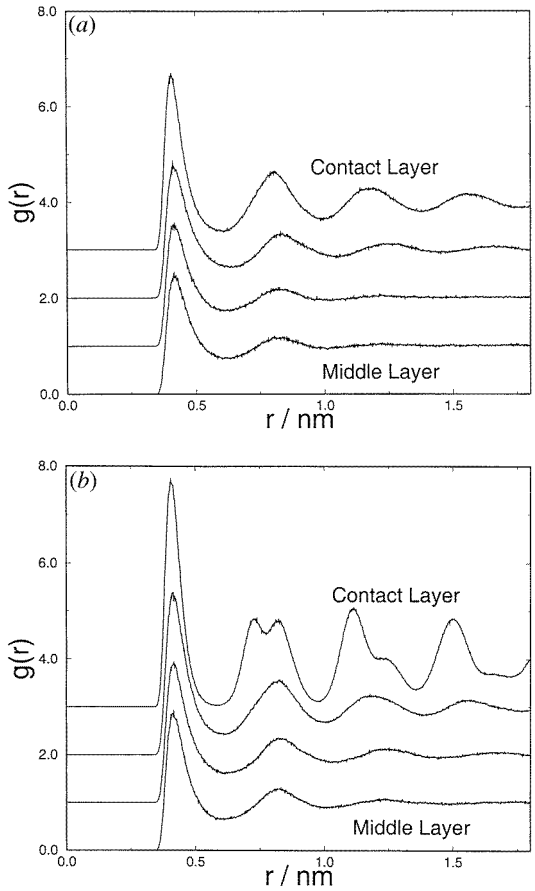

Figure 52. The two-dimensional, in-plane pair correlation function for each of the adsorbed methane layers for the $H = 7.5\sigma$ graphite slit pore at three different temperatures: (*a*) $T = 130$ K, corresponding to phase A; (*b*) $T = 123$ K, corresponding to phase B. Only four of the seven layers are shown because of the symmetry about the mid-plane. From [303].

strengths $0.5 < \alpha/\epsilon_{ff} < 0.85$ there are three phases, with the intermediate phase B having a structure such that the contact layers are liquid like while the inner layers are crystalline. For strongly attractive pore walls, $\alpha/\epsilon_{ff} > 1.15$, the intermediate phase B had frozen contact layers and liquid-like inner layers (as in figure 52(*b*)). The LJ fluid confined in the slit pore showed depression in the freezing temperature for $\alpha/\epsilon_{ff} < 0.85$ and elevation in freezing temperature for $\alpha/\epsilon_{ff} > 1.15$. Radhakrishnan *et al* [304] used corresponding states theory to map out a global phase diagram that predicts the phase behaviour and freezing temperatures for different fluids confined in different porous materials based on the effect of the fluid–wall interactions.

Figure 54 summarizes the predictions of this theory for a variety of fluids. The fluid–fluid terms were determined from second virial coefficient data and the Lorentz–Berthelot mixing rule was invoked to calculate the fluid–wall parameters. For the case of polar molecules, only the dispersive part of the fluid–fluid interaction was used to obtain the fluid–wall parameters and the pore walls were assumed to be non-polarizable. Figure 54 predicts the phase behaviour of different fluids in model (slit shaped) silica and graphite pores. The structure of the confined

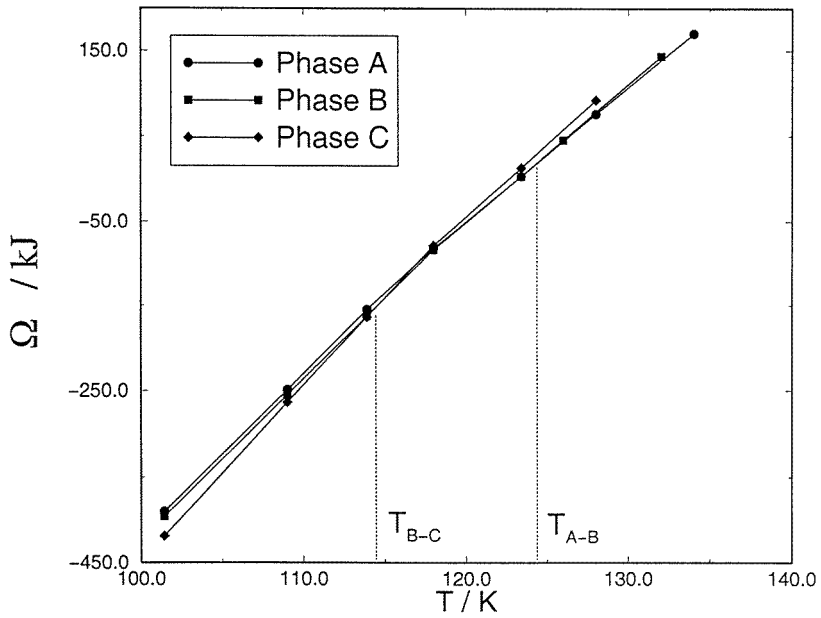

Figure 53. The grand free energy of the three phases A, B and C, as a function of temperature for LJ methane in the graphite slit pore of $H = 7.5\sigma$. The cross-over points T_{A-B} and T_{B-C} correspond to the two first-order phase transitions. The freezing temperature of LJ methane in the bulk is 101 K. From [303].

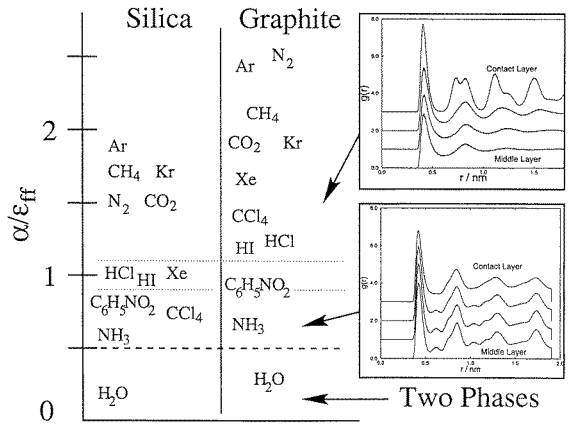

Figure 54. The global phase diagram, summarizing the freezing behaviour of different fluids in model silica and graphite slit pores of width $H = 7.5\sigma$. The two dotted lines represent the boundary between the elevation and depression of the freezing temperature. From [304].

phase is given by the pair correlation function plots of the individual layers of the confined phase. Such a classification can be used to estimate freezing temperature shifts and phase behaviour of a fluid/pore system. However, one should bear in mind that, apart from the fluid–wall strength parameter α, other factors such as change in geometry (cylindrical instead of slit shaped pore) and surface polarizability of the pore walls will also contribute significantly to the freezing behaviour.

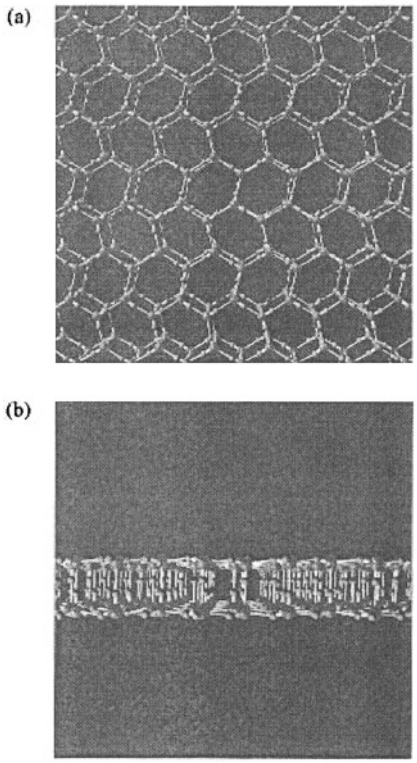

Figure 55. The structure of water adsorbed in a slit carbon pore of width $H = 3\sigma$ at $T = 180$ K under a loading pressure of 1 Gpa, showing a distorted hexagonal lattice: (*a*) top view, (*b*) side view. From [183].

Koga *et al* [183] have studied the freezing of water in hydrophobic nanopores by molecular dynamics simulation, using the TIP4P model for water and a weakly interacting, structureless wall. They observed a bilayer ice formation by controlling the pressure normal to the pore walls. The bilayer ice crystal is characterized by a hydrogen-bonding network of water molecules, each layer forming a distorted hexagonal lattice (figure 55). However, the study only focused on the approximate bounds for the free energies of the condensed phases.

6.3. Simulation studies: complex pore geometries

One of the first efforts in studying the effects of surface epitaxy on phase behaviour [313] considered a slit pore model with the pore wall atoms arranged on a fcc lattice. The nature of the confined phase (whether a liquid or solid) was found to depend on whether the top wall surface was 'in' or 'out' of registry with the bottom surface. It was also found that, for the same number of layers in the confined phase, pore widths below a critical value did not support a solid phase, that is, below a certain value of inter-layer separation, the solid phase was not stable. Similarly, under conditions that supported a confined solid phase [61], moving the top plate such that the configuration goes from 'out' of registry to 'in' registry, melts the solid phase. This observation was also confirmed by other studies modelling the shear behaviour in a surface force apparatus, in which the 'stick–slip' behaviour was attributed to shear-induced melting transitions [207, 356].

The freezing of simple fluids in a corrugated pore model that consisted of a slit pore with rectangular grooves carved out of one of the surfaces exhibits a rich phase behaviour that depends on the width of the pore, width of the groove and depth of the groove [61]. Over a

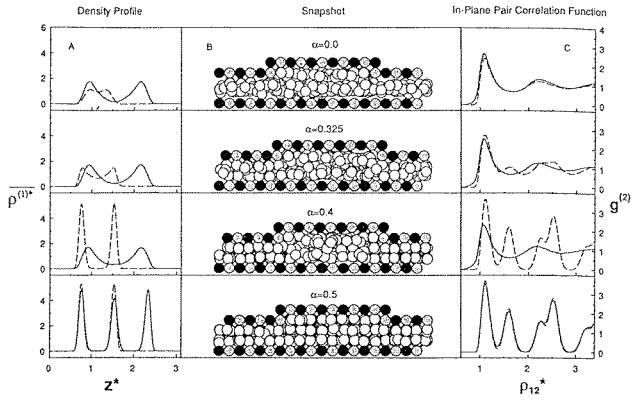

Figure 56. Local density profiles $\rho^{(1)}(z)$, in-plane pair correlation functions $g^{(2)}$ and snapshots of the configuration of LJ molecules in a 'grooved' slit pore. The shaded spheres represent the wall atoms (the grey and the black spheres represent alternate rows of an fcc lattice), and the open spheres represent the adsorbed molecules. The parameter α defines the lateral allignment or 'registry' of the opposing pore walls, ($\alpha = 0$: the walls are precisely in registry, $\alpha = 0.5$: the walls are completely out of registry). The dashed and the solid curves represent the profiles for fluid adsorbed in the narrow region and the wide region of the pore, respectively. From [61].

range of registries and groove depth, the confined phase consisted of fluid and solid portions in equilibrium, i.e., fluid filled nanocapillaries separated by solid strips (figure 56).

The effect of the presence of active sites on the adsorbent surface was briefly addressed by Vishnyakov *et al* [372] for graphitic slit pores. The authors considered several models for graphitic pores with varying pore widths and different densities of NH_2, $CH = O$, CH_3OH groups on a graphitic surface to model anthracite. The freezing temperature was found to be strongly dependent on the nature and the density of the active sites present.

6.4. Freezing versus glass transition

In general, one must exercise care in interpreting freezing inside pores. Experiments such as differential scanning calorimetry do not give any information on the structure of the confined phase. It is also difficult to use diffraction methods to characterize the structure of the confined phase, because of the presence of the additional signal due to the adsorbent molecules. Spectroscopic methods such as NMR and dielectric relaxation spectroscopy are useful under these circumstances, as they yield information about the translational and orientational relaxation time of the molecules in the confined phase. For example, in the study of freezing of O_2 in sol–gel glasses [379], the orientational relaxation time τ of molecules was measured as a function of T and a sharp drop in τ (about four orders of magnitude) was observed at the transition. A similar measurement for a glass transition would show a continuous change from liquid phase to glass phase relaxation times.

In computer simulation studies of freezing in confined geometries, it is possible to directly measure the pair correlation function to monitor the freezing process. However, for finite system size even a glassy phase can display extended positional correlations [52]. An additional measure of the self-diffusion coefficient often provides a distinction between a freezing transition and a glass transition. Free-energy calculations are very useful, as the nature of the phase transition can be inferred directly. The order parameter provides a direct measure of the difference in bond orientational order between the ordered and disordered phase. Thus,

for the case of a glass transition, the minimum in the Landau free-energy curve at the value of the order parameter corresponding to the crystalline phase would be absent, unlike figure 51.

The glass transition in a porous medium is an interesting topic in its own right. There have been a number of studies that have investigated the effect of confinement on glass-forming organic liquids [296,297,329,330]. It is well established that the glass transition temperature T_g of a liquid inside a porous glass is shifted by ΔT_g, the sign and extent of which is material specific, just as for the case of freezing. Dielectric relaxation studies have indicated a slower relaxation process in the confined liquid as compared with the bulk, and the appearance of an additional relaxation component due to the contact layer, consistent with the studies on freezing. However, unlike freezing, there seems to be no general basis to explain the nature of the shift in ΔT_g.

7. Conclusions

There has been a considerable advance in our understanding of phase equilibria and separation in model pores of simple geometry, particularly cylindrical and slit-shaped pores, over the last decade. Capillary condensation and layering transitions have been extensively investigated. Less work has been done on liquid–liquid equilibria and freezing in such systems, but a clearer picture of these phenomena is also beginning to emerge. Little work seems to have been reported on the effects of confinement on phase equilibria for mixtures, other than that for liquid–liquid separations.

The relationship between this rather large body of theoretical work and the behaviour of adsorbates in real porous materials remains unclear. All experimental materials possess some degree of heterogeneity in the pores (an exception is the surface force apparatus), and it is not easy to distinguish effects of chemical and geometric heterogeneity. On the modelling side, there is a need now to develop better models for such materials, and to use these to gain a better understanding of phase equilibria in real materials. Examples of steps in this direction were discussed in section 3.3 for the case of capillary condensation. The need for better models is particularly acute for the amorphous porous materials, such as activated carbons, aerogels and oxides. In some cases it may be possible to mimic the manufacturing process (as in the case of the CPGs discussed in section 3.3). In others, such as the activated carbons, this will be difficult or impossible because of the complexity of the processes involved; nevertheless, it may prove possible to simulate the final stages of manufacture and thus produce structures that more closely resemble the real materials.

On the experimental side there is a continuing need to develop more well-characterized materials in which it is possible to control and vary the pore size in the manufacturing process. Better ways to characterize such materials are needed. Many of the standard methods used to estimate pore sizes, pore volumes and surface area are more than 50 years old, and in some cases are known to be seriously in error for pore sizes below a few nanometres. Hopefully, improved methods for interpreting experimental data will emerge from improved models of the type discussed in the previous paragraph.

A persistent problem in this field has been the difficulty of bringing experiment and theory together in a fruitful way, a result of the difficulty of characterization of materials on the experimental side, combined with the difficulty of developing adequate models for use in the theories and simulations. We hope that this situation will gradually improve as increased computational power makes more sophisticated models a reality, and as new materials become available.

Acknowledgments

It is a pleasure to thank M Endo, S Hyde, K Kaneko and L C Rainey for providing electron micrograph figures of porous materials. We are grateful for support of our work by the National Science Foundation (grant no CTS-9896195), the Department of Energy (grant no DE-FG02-98ER14847), and KBN (grant no 2-PO3B-17508). Supercomputer time was provided under a NSF/NPACI grant (no MCA93S011P). LDG thanks the National Science Foundation for a CISE postdoctoral award (grant no ACI-9896107). International cooperation was aided by a grant from the US–Poland Maria Sklodowska–Curie Joint Fund (no MEN/DOE-97-314).

References

[1] Adams D J 1975 *Mol. Phys.* **29** 307–11
[2] Ajayan P M 1996 *Carbon Nanotubes: Preparation and Properties* ed T W Ebbesen (Boca Raton, FL: Chemical Rubber Company)
[3] Albano E V, Binder K, Heerman D W and Paul W 1992 *Physica* A **183** 130–47
[4] Allen M P and Tildesley D J 1987 *Computer Simulation of Liquids* (Oxford: Clarendon)
[5] Alvarez M, Levesque D and Weiss J-J 1999 *Phys. Rev.* E **60** at press
[6] Asada H 1990 *Surf. Sci.* **230** 323–8
[7] Attard G S, Glyde J C and Göltner C G 1995 *Nature* **378** 366
[8] Bailey A E, Frisken B J and Cannell D S 1997 *Phys. Rev.* E **56** 3112–18
[9] Baker J M, Dore J C and Behrens P 1997 *J. Phys. Chem.* B **101** 6226
[10] Balbuena P B and Gubbins K E 1992 *Fluid Phase Equilib.* **76** 21–35
[11] Balbuena P B and Gubbins K E 1993 *Langmuir* **9** 1801–14
[12] Balbuena P B and Gubbins K E 1994 *Characterization of Porous Solids III (Studies in Surface Science and Catalysis vol 87)* ed J Rouquerol *et al* (Amsterdam: Elsevier) pp 41–50
[13] Ball P C and Evans R 1988 *J. Chem. Phys.* **89** 4412
[14] Ball P C and Evans R 1989 *Langmuir* **5** 714–23
[15] Bansal R C, Donnet J B and Stoeckli H F 1988 *Active Carbon* (New York: Dekker)
[16] Barber M N 1983 *Phase Transitions and Critical Phenomena* vol 8, ed C Domb and J L Lebowitz (London: Academic) ch 2, pp 145–475
[17] Baumgärtner A and Muthukumar M 1996 *Adv. Chem. Phys.* vol XCIV, ed I Prigogine and S A Rice (New York: Wiley) pp 625–708
[18] Beamish J R, Hikata A, Tell L and Elbaum C 1983 *Phys. Rev. Lett.* **50** 425
[19] Beck J S *et al* 1992 *J. Am. Chem. Soc.* **114** 10 834
[20] Bennett C H 1976 *J. Comput. Phys.* **22** 245–68
[21] Berendsen H J C, Postma J P M, van Gunsteren W F, DiNiola A and Haak J R 1984 *J. Chem. Phys.* **81** 3684–90
[22] Berg B A and Neuhaus T 1991 *Phys. Lett.* B **267** 249
[23] Berg B A and Neuhaus T 1992 *Phys. Rev. Lett.* **68** 9–12
[24] Bienfait M 1987 *Europhys. Lett.* **4** 79–84
[25] Bienfait M, Gay J M and Blank H 1988 *Surf. Sci.* **204** 331–44
[26] Bienfait M, Zeppenfeld P, Gay J M and Palmari J P 1990 *Surf. Sci.* **226** 327–38
[27] Biggs M and Agarwal P 1992 *Phys. Rev.* A **46** 3312
[28] Biggs M and Agarwal P 1995 *Phys. Rev.* E **49** 531–7
[29] Binder K 1990 *Finite Size Scaling and Numerical Simulation of Statistical Systems* ed V Privman (Singapore: World Scientific) ch 4, pp 173–221
[30] Binder K and Landau D P 1988 *Phys. Rev.* B **37** 1745
[31] Binder K and Landau D P 1992 *J. Chem. Phys.* **96** 1444–54
[32] Bock H and Schoen M 1999 *Phys. Rev.* E **59** 4122–36
[33] Bojan M J, Cheng E, Cole M W and Steele W A 1996 *Adsorption* **2** 51–8
[34] Bojan M J, Stan G, Curtarolo S, Steele W A and Cole M W 1999 *Phys. Rev.* E **59** 864–73
[35] Bojan M J and Steele W A 1993 *Proc. 4th Int. Conf. on Fundamentals of Adsorption* ed M Suzuki (Tokyo: Kodansha) pp 51–8
[36] Booth H F and Strange J H 1998 *Mol. Phys.* **93** 263
[37] Branton P J, Hall P G and Sing K S W 1993 *J. Chem. Soc., Chem. Commun.* 1257–8

[38] Branton P J, Hall P G, Sing K S W, Reichert H, Schüth F and Unger K K 1994 *J. Chem. Soc., Faraday Trans.* **90** 2965
[39] Branton P J, Sing K S W and White J W 1997 *J. Chem. Soc., Faraday Trans.* **93** 2337–40
[40] Brennan J K and Dong W 1999 *J. Chem. Phys.* submitted
[41] Brochard F and De Gennes P G 1983 *J. Physique Lett.* **44** L785–91
[42] Brown A J, Burgess C G V, Everett D H and Nuttall S 1997 *Characterization of Porous Solids* vol IV, ed T J McEnaney *et al* (Cambridge: Royal Society of Chemistry) pp 1–8
[43] Brown D W, Sokol P E, Clarke A P, Alam M A and Nuttall W J 1997 *J. Phys.: Condens. Matter* **9** 7317–25
[44] Bruno E, Marini Bettolo Marconi U and Evans R 1987 *Physica* A **141** 187
[45] Bryk P, Patrykiejew A, Reszko-Zygmunt J and Sokolowski S 1999 *Mol. Phys.* **96** 1509–16
[46] Burgess C G V, Everett D H and Nuttall S 1989 *Pure Appl. Chem.* **61** 1845–52
[47] Cascarini de Torre L E, Bottani E J and Steele W A 1996 *Langmuir* **12** 5399–406
[48] Castro M A, Clarke S M, Inaba A and Thomas R K 1997 *J. Phys. Chem.* B **101** 8878
[49] Chiarello R, Coulomb J P, Krim J and Wang C L 1988 *Phys. Rev.* B **38** 8967–73
[50] Chiccoli C, Lavrentovich O D, Pasini P and Zannoni C 1997 *Phys. Rev. Lett.* **79** 4401–4
[51] Chmiel C, Karykowski K, Patrykiejew A, Rzysko W and Sokolowski S 1994 *Mol. Phys.* **81** 691
[52] Chokappa D K and Clancy P 1987 *Mol. Phys.* **61** 617
[53] Cleaver D J and Allen M P 1993 Computer simulation of liquid crystal films *Mol. Phys.* **80** 253–76
[54] Cole M W, Crespi V H, Stan G, Hartman J M, Moroni S and Boninsegni M 1999 *Phys. Rev. Lett.* submitted
[55] Cracknell R F, Gubbins K E, Maddox M W and Nicholson D 1995 *Accs. Chem. Res.* **28** 281–8
[56] Cracknell R F, Koh C A, Thompson S M and Gubbins K E 1993 *Mat. Res. Soc. Symp. Proc.* **290** 135–46
[57] Cracknell R F, Nicholson D and Quirke N 1993 *Mol. Phys.* **80** 885–97
[58] Cracknell R F, Nicholson D, Tennison S R and Bromhead J 1996 *Adsorption* **2** 193–203
[59] Crawford G P, Steele L M, Ondris-Crawford R, Iannachhione G S, Yeager C J, Doane J W and Finotello D 1992 *J. Chem. Phys.* **96** 7788–96
[60] Csáthy G A, Tulimieri D, Yoon J and Chan M H W 1998 *Phys. Rev. Lett.* **80** 4482–5
[61] Curry J E, Zhang F, Cushman J H, Schoen M and Diestler D J 1994 *J. Chem. Phys.* **101** 10 824–32
[62] Curtarolo S, Stan G, Cole M W, Bojan M J and Steele W A 1999 *Phys. Rev.* E **59** 4402–7
[63] Dadmun M D and Muthukumar M 1993 *J. Chem. Phys.* **98** 4850–2
[64] DeKeizer A, Michalski T and Findenegg G H 1991 *Pure Appl. Chem.* **63** 1495
[65] Derjaguin B V 1940 *Zh. Fiz. Khim.* **40** 137 (Engl. transl. *Acta. Phys. Chem.* **12** 181)
[66] De Gennes P G 1984 *J. Phys. Chem.* **88** 6469–72
[67] De Miguel E, del Rio E M and Telo de Gama M M 1995 *J. Chem. Phys.* **103** 6188–96
[68] De Oliveira M J and Griffiths R B 1978 *Surf. Sci.* **71** 687–94
[69] Dominguez H, Allen M P and Evans R 1998 *Mol. Phys.* **96** 209–29
[70] Duffy J A, Wilkinson N J, Fretwell H M, Alam M A and Evans R 1995 *J. Phys.: Condens. Matter* **7** L713
[71] Ebbesen T W 1997 *Carbon Nanotubes* (Boca Raton, FL: Chemical Rubber Company)
[72] Ebner C 1981 *Phys. Rev.* A **23** 1925
[73] Ebner C 1983 *Phys. Rev.* B **28** 2890
[74] Elder K J, Reynolds P A, Trouw F and White J W 1996 *J. Chem. Soc. Chem. Commun.* 155
[75] Entov L V, Levchenko V A and Voronov V P 1993 *Int. J. Thermophys.* **14** 221–9
[76] Escobedo F A and de Pablo J J 1999 *Phys. Rep.* **318** 85–112
[77] Evans R 1979 *Adv. Phys.* **28** 143
[78] Evans R 1990 *Liquids at Interfaces (Les Houches Session XLVIII)* ed J Charvolin, J Joanny and J Zinn-Justin (Amsterdam: Elsevier)
[79] Evans R 1990 *J. Phys.: Condens. Matter* **2** 8989–9007
[80] Evans R 1992 *Fundamentals of Inhomogeneous Fluids* ed D Henderson (New York: Dekker) ch 5
[81] Evans R and Marini Bettolo Marconi U 1985 *Chem. Phys. Lett.* **114** 415
[82] Evans R and Marini Bettolo Marconi U 1987 *J. Chem. Phys.* **86** 7138–48
[83] Evans R, Marini Bettolo Marconi U and Tarazona P 1986 *J. Chem. Soc. Faraday Trans.* **2** 1763–87
[84] Evans R, Marini Bettolo Marconi U and Tarazona P 1986 *J. Chem. Phys.* **84** 2376–99
[85] Fan Y and Monson P A 1993 *J. Chem. Phys.* **99** 6897
[86] Ferrenberg A M, Landau D P and Swendsen R H 1995 *Phys. Rev.* E **51** 5092–100
[87] Ferrenberg A M and Swendsen R H 1988 *Phys. Rev. Lett.* **61** 2635–8
[88] Ferrenberg A M and Swendsen R H 1989 *Phys. Rev. Lett.* **63** 1195–8
[89] Feuston B P and Garofalani S H 1988 *J. Chem. Phys.* **89** 5818
[90] Findenegg G H, Gross S and Michalski T 1994 *Characterization of Porous Solids III (Studies in Surface Science and Catalysis vol 87)* ed J Rouquerol *et al* (Amsterdam: Elsevier)

[91] Finn J E and Monson P A 1989 *Phys. Rev.* A **39** 6402–8
[92] Finotello D, Gillis K A, Wong A and Chan M H W 1988 *Phys. Rev. Lett.* **61** 1954–7
[93] Fisher L R and Israelachvili J N 1981 *J. Colloid Interface Sci*. **80** 528
[94] Fisher M and Nakanishi H 1981 *J. Chem. Phys.* **75** 5857–63
[95] Forsman J and Woodward C E 1999 *Mol. Phys* **96** 189–200
[96] Franck C 1992 *Fundamentals of Inhomogeneous Fluids* ed D Henderson (New York: Dekker) pp 277–302
[97] Frenkel D and Ladd A J C 1984 *J. Chem. Phys.* **81** 3188
[98] Frenkel D and Smit B 1996 *Understanding Molecular Simulation* (New York: Academic)
[99] Frisken B J and Cannell D S 1992 *Phys. Rev. Lett.* **69** 632–5
[100] Frisken B J, Cannell D S, Lin M Y and Sinha S K 1995 *Phys. Rev.* E **51** 5866–79
[101] Frisken B J, Ferri F and Cannell D S 1995 *Phys. Rev.* E **51** 5922–43
[102] Gaucher H, Grillet Y, Beguin F, Bonnamy S and Pellenq R J M 1998 ed F Meunier *Fundamentals of Adsorption* vol 6 (Paris: Elsevier) pp 243–8
[103] Gay J G and Berne B J 1981 *J. Chem. Phys.* **74** 3316–19
[104] Gay J M, Suzanne J and Coulomb J P 1990 *Phys. Rev.* B **41** 11 346–51
[105] Gelb L D 1994 *Phys. Rev.* B **50** 11 146–50
[106] Gelb L D and Gubbins K E 1997 *Phys. Rev.* E **56** 3185–96
[107] Gelb L D and Gubbins K E 1997 *Phys. Rev.* E **55** 1290R
[108] Gelb L D and Gubbins K E 1997 *Physica* A **244** 112–23
[109] Gelb L D and Gubbins K E 1998 *Langmuir* **14** 2097–111
[110] Gelb L D and Gubbins K E 1999 *Langmuir* **15** 305–8
[111] Gelb L D and Gubbins K E 1999 in preparation
[112] Gelb L D and Lynden-Bell R M 1994 *Phys. Rev.* B **49** 2058–66
[113] Givens J A and Stell G 1992 *J. Chem. Phys.* **97** 4573–4
[114] Givens J A and Stell G 1993 *Condensed Matter Theories* vol 8, ed L Blum and F B Malik (New York: Plenum) pp 395–410
[115] Givens J A and Stell G 1994 *Physica* A **209** 495–510
[116] Goldburg W I, Aliev F and Wu X-I 1995 *Physica* A **213** 61–70
[117] Göltner C G and Antonietti M 1997 *Adv. Mater.* **9** 431
[118] González A, White J A, Román F L, Velasco S and Evans R 1997 *Phys. Rev. Lett.* **79** 2466–9
[119] Góźdź W T, Gubbins K E and Panagiotopoulos A Z 1995 *Mol. Phys.* **84** 825–34
[120] Granick S 1991 *Science* **253** 1374
[121] Gray C G and Gubbins K E 1984 *Theory of Molecular Fluids* (Oxford: Clarendon) ch 2 and appendix C
[122] Gregg S J and Sing K S W 1982 *Adsorption, Surface Area and Porosity* (London: Academic)
[123] Gross S and Findenegg G 1997 *Ber. Bunsenges. Phys. Chem.* **101** 1726–30
[124] Gruhn T and Schoen M 1997 *Phys. Rev.* E **55** 2861–75
[125] Gruhn T and Schoen M 1998 *J. Chem. Phys.* **108** 9124–36
[126] Gubbins K E 1997 *Physical Adsorption: Experiment, Theory and Applications* ed J Fraissard (Dordrecht: Kluwer) pp 65–103
[127] Gubbins K E, Sliwinska-Bartkowiak M and Suh S-H 1996 *Mol. Simul.* **17** 333–67
[128] Haller W 1983 *Solid Phase Biochemistry* ed W H Scouten (New York: Wiley) ch 11, pp 535–97
[129] Hansen E W, Stöker M and Schmidt R 1996 *J. Phys. Chem.* **100** 2195
[130] Hansen J P and Verlet L 1969 *Phys. Rev.* **184** 151
[131] Hanzawa Y, Kaneko K, Pekala R W and Dresselhaus M S *Langmuir* **12** 6167–9
[132] Hanzawa Y, Kaneko K, Yoshizawa N, Pekala R W and Dresselhaus M S 1998 *Adsorption* **4** 187–95
[133] Hanzawa Y, Yoshizawa T and Kaneko K 1998 Private communication
[134] Hastings W K 1970 *Biometrika* **57** 97–109
[135] Heffelfinger G S, Tan Z, Gubbins K E, Marini Bettolo Marconi U and Van Swol F 1988 *Int. J. Thermophys.* **9** 1051–60
[136] Heffelfinger G S, Tan Z, Gubbins K E, Marini Bettolo Marconi U and Van Swol F 1989 *Mol. Simul.* **2** 393–411
[137] Heffelfinger G S, Van Swol F and Gubbins K E 1987 *Mol. Phys.* **61** 1381–90
[138] Heffelfinger G S, Van Swol F and Gubbins K E 1988 *J. Chem. Phys.* **89** 5202–5
[139] Henderson D 1992 *J. Chem. Phys.* **97** 1266–70
[140] Henderson D 1992 *Fundamentals of Inhomogeneous Fluids* (New York: Dekker)
[141] Henderson D and Plischke M 1992 *J. Chem. Phys.* **97** 7822–4
[142] Henderson J R 1994 *Phys. Rev.* E **50** 4836–46
[143] Hess G B 1991 *Phase Transitions in Surface Films* vol 2, ed H Taub *et al* (New York: Plenum) pp 357–89
[144] Hill T L 1956 *Statistical Mechanics, Principles and Selected Applications* (New York: McGraw-Hill) ch 7

[145] Hoover W G 1985 *Phys. Rev.* A **31** 1695–7
[146] Hu H W, Carson G A and Granick S 1991 *Phys. Rev. Lett.* **66** 2758
[147] Huang K 1963 *Statistical Mechanics* 2nd edn (New York: Wiley)
[148] Hunter J E III and Reinhardt W P 1995 *J. Chem. Phys.* **103** 8627–37
[149] Hyde S 1993 Private communication
[150] Iannachione G S, Crawford G P, Qian S, Doane J W and Finotello D 1996 *Phys. Rev.* E **53** 2402–11
[151] Iannachione G S, Crawford G P, Žumer S, Doane J W and Finotello D 1993 *Phys. Rev. Lett.* **71** 2595–8
[152] Iannachione G S, Qian S, Finotello D and Aliev F M 1997 *Phys. Rev.* E **56** 554–61
[153] Iiyama T, Nishikawa K, Otowa T and Kaneko K 1995 *J. Phys. Chem.* **99** 10 075
[154] Iiyama T, Nishikawa K, Suzuki T and Kaneko K 1997 *Chem. Phys. Lett.* **274** 152
[155] Iler R K 1979 *The Chemistry of Silica* (New York: Wiley)
[156] IUPAC 1985 *International Committee for Characterization and Terminology of Carbon* **20** 445
IUPAC 1985 *International Committee for Characterization and Terminology of Carbon* **21** 517
IUPAC 1985 *International Committee for Characterization and Terminology of Carbon* **23** 601
[157] Jagiello J and Tolles D 1998 ed F Meunier *Fundamentals of Adsorption* vol 6 (Paris: Elsivier) pp 629–34
[158] Jayanthi C S 1991 *Phys. Rev.* B **44** 427
[159] Jérôme B 1991 *Rep. Prog. Phys.* **54** 391–451
[160] Jiang S and Gubbins K E 1995 *Mol. Phys.* **86** 599–612
[161] Jiang S, Gubbins K E and Balbuena P B 1994 *J. Phys. Chem.* **98** 2403–241
[162] Jiang S, Rhykerd C L and Gubbins K E 1993 *Mol. Phys.* **79** 373–91
[163] Kahng J and Ebner C 1989 *Phys. Rev.* B **40** 11 269
[164] Kaminsky R D and Monson P A 1991 *J. Chem. Phys.* **95** 2936–48
[165] Kaminsky R D and Monson P A 1994 *Langmuir* **10** 530–7
[166] Kaminsky R D and Monson P A 1994 *Chem. Engng Sci.* **49** 2967–77
[167] Kaneko K 1998 *Adsorption and its Application to Industry and Environmental Protection: Surface Science and Catalysis 120B* vol II, ed A Dobrowski (Amsterdam: Elsevier)
[168] Keblinski P, Ma W-J, Maritan A, Koplik J and Banavar J R 1993 *Phys. Rev.* E **47** R2265–8
[169] Kellay H, Bonn D and Meunier J 1993 *Phys. Rev. Lett.* **71** 2607
[170] Kierlik E and Rosinberg M 1990 *Phys. Rev.* A **42** 3382–7
[171] Kierlik E and Rosinberg M 1991 *Phys. Rev.* A **44** 5025–37
[172] Kierlik E, Rosinberg M L, Tarjus G and Monson P A 1996 *J. Phys.: Condens. Matter* **8** 9621–5
[173] Kierlik E, Rosinberg M L, Tarjus G and Monson P A 1998 ed F Meunier *Fundamentals of Adsorption* vol 6 (Paris: Elsevier) pp 867–72
[174] Kierlik E, Rosinberg M L, Tarjus G and Pitard E 1998 *Mol. Phys.* **95** 341–51
[175] Kim H K, Feng Y P, Zhang Q M and Chan M H W 1988 *Phys. Rev.* B **37** 1745–65
[176] Kim S B, Ma J and Chan M H W 1993 *Phys. Rev. Lett.* **71** 2268–71
[177] Kim Y W, Kim S C and Suh S H 1999 *J. Chem. Phys.* **110** 1230–4
[178] Kjellander R and Sarman S 1990 *Mol. Phys.* **70** 215–37
[179] Kjellander R and Sarman S 1991 *Mol. Phys.* **74** 665–88
[180] Klein J and Kumacheva E 1995 *Science* **269** 816
[181] Klein J and Kumacheva E 1998 *J. Chem. Phys.* **108** 6996
Klein J and Kumacheva E 1998 *J. Chem. Phys.* **108** 7010
[182] Kofke D A and Glandt E D 1988 *Mol. Phys.* **64** 1105–31
[183] Koga K, Zeng X C and Tanaka H 1997 *Phys. Rev. Lett.* **79** 5262
[184] Kotelyanskii M and Kumar S K 1998 *Phys. Rev. Lett.* **80** 1252–5
[185] Kralj S, Zidanšek A, Lahajnar G, Muševič I, Žumer S, Blinc R and Pintar M M 1996 *Phys. Rev.* E **53** 3629–38
[186] Krim J, Coulomb J P and Bouzidi J 1987 *Phys. Rev. Lett.* **58** 583–6
[187] Kruk M, Jaroniec M and Sayari A 1997 *Langmuir* **13** 6267–73
[188] Lachet V, Boutin A, Tavitian B and Fuchs A H 1998 *J. Phys. Chem.* B **102** 9224–33
[189] Landau L D and Lifshitz E M 1980 *Statistical Physics* 3rd edn (London: Pergamon)
[190] Laradji M, Toxvaerd S and Mouritsen O G 1996 *Phys. Rev. Lett.* **77** 2253–6
[191] Larese J Z 1993 *Acc. Chem. Res.* **26** 353–60
[192] Larese J Z, Harada M, Passell L, Krim J and Satija S 1988 *Phys. Rev.* B **37** 4735–42
[193] Larese J Z and Zhang Q M 1990 *Phys. Rev. Lett.* **64** 922–5
[194] Larese J Z and Zhang Q M 1995 *Phys. Rev.* B **51** 17 023–7
[195] Lastoskie C M, Gubbins K E and Quirke N 1993 *J. Phys. Chem.* **97** 4786–96
[196] Lastoskie C M, Gubbins K E and Quirke N 1993 *Langmuir* **9** 2693–702
[197] Lastoskie C M, Quirke N and Gubbins K E 1997 *Equilibria and Dynamics of Gas Adsorption on Heteregeneous*

Surfaces (Studies in Surface Science and Catalysis vol 104) ed W Rudzinski, W A Steele and G Zgrablich (Amsterdam: Elsevier) pp 745–75
[198] Lee J C 1992 *Phys. Rev.* B **46** 8648–51
[199] Lee J C 1993 *Phys. Rev. Lett.* **70** 3599–602
[200] Lee M and Chan K Y 1995 *Chem. Phys. Lett.* **275** 56–62
[201] Lin M Y, Sinha S K, Drake J M, Wu X-I, Thiyagarajan P and Stanley H B 1994 *Phys. Rev. Lett.* **72** 2207–10
[202] Liu A J, Durian D J, Herbolzheimer E and Safran S A 1990 *Phys. Rev. Lett.* **65** 1897–900
[203] Liu A J and Grest G S 1991 *Phys. Rev.* A **44** R7894–7
[204] Lo W Y and Chan K-Y 1995 *Mol. Phys.* **86** 745–58
[205] Lomba E, Given J A, Stell G, Weis J J and Levesque D J 1993 *Phys. Rev.* E **48** 233–44
[206] Long Y, Xu T, Sun Y and Dong W 1998 *Langmuir* **14** 6173–8
[207] Lupowski M and VanSwol F 1991 *J. Chem. Phys.* **95** 1995–8
[208] Lynden-Bell R M, van Duijneveldt J S and Frenkel D 1993 *Mol. Phys.* **80** 801
[209] Ma W-J, Maritan A, Banavar J R and Koplik J 1992 *Phys. Rev.* A **45** R5347–50
[210] MacElroy J M D 1993 *Langmuir* **9** 2682–92
[211] MacElroy J M D and Raghavan K K 1990 *J. Chem. Phys.* **93** 2068–79
[212] MacFarland T, Barkema G T and Marko J F 1996 *Phys. Rev.* B **53** 148–58
[213] Machin W D 1992 *J. Chem. Soc., Faraday Trans.* **88** 729–35
[214] Machin W D 1994 *Langmuir* **10** 1235–40
[215] Machin W D 1999 *Langmuir* **15** 169–73
[216] Maciolek A, Ciach A and Evans R 1998 *J. Chem. Phys.* **108** 9765–74
[217] Maciolek A, Evans R and Wilding N B 1999 *Phys. Rev.* E at press
[218] Madden W G and Glandt E D 1988 *J. Stat. Phys.* **51** 537–58
[219] Maddox M and Gubbins K E 1997 *J. Chem. Phys.* **107** 9659
[220] Maddox M W and Gubbins K E 1995 *Langmuir* **11** 3988–96
[221] Maddox M W, Lastoskie C M, Quirke N and Gubbins K E 1996 *Fundamentals of Adsorption* ed M D LeVan (Boston, MA: Kluwer) pp 571–8
[222] Maddox M W, Olivier J P and Gubbins K E 1997 *Langmuir* **13** 1737–45
[223] Maddox M W, Quirke N and Gubbins K E 1997 *Mol. Simul.* **19** 267–83
[224] Maddox M W, Ulberg D and Gubbins K E 1995 *Fluid Phase Equilib.* **104** 145–8
[225] Madih K, Croset B, Coulomb J P and Lauter H J 1989 *Europhys. Lett.* **8** 459–64
[226] Maher J V, Goldburg W I, Pohl D W and Lanz M 1984 *Phys. Rev. Lett.* **53** 60–3
[227] Maitland G C, Rigby M, Smith E B and Wakeham W A 1981 *Intermolecular Forces: Their Origin and Determination*. (Oxford: Clarendon)
[228] Maritan A and Cieplak M 1992 *Phys. Rev. Lett.* **69** 221–4
[229] Maritan A, Cieplak M, Bellini T and Banavar J R 1994 *Phys. Rev. Lett.* **72** 4113–16
[230] Marini Bettolo Marconi U and Van Swol F 1989 *Phys. Rev.* A **39** 4109–16
[231] Mason G 1982 *J. Colloid Interface Sci.* **88** 36
[232] Mason G 1983 *Proc. R. Soc.* A **390** 47–72
[233] Mattson J S and Mark H B 1971 *Activated Carbon, Surface Chemistry and Adsorption from Solution* (New York: Dekker)
[234] McCallum C, Bandosz T J, McGrother S C, Muller E A and Gubbins K E 1999 *Langmuir* **15** 533–44
[235] McDonald I R and Singer K 1967 *J. Chem. Phys.* **47** 4766–72
[236] McEnaney B and Mays T M 1989 *Introduction to Carbon Science* (London: Butterworths)
[237] Meier W M and Olson D H 1992 *Atlas of Zeolite Structure Types* (London: Butterworth–Henemann)
[238] Miyahara M and Gubbins K E 1997 *J. Chem. Phys.* **106** 2865
[239] Miyahara M, Kanda H, Higashitani K and Gubbins K E 1999 *Proc. COPS-V, Characterization of Porous Solids* (Amsterdam: Elsevier) at press
[240] Molz E, Wong A P Y, Chan M H W and Beamish J R 1993 *Phys. Rev.* B **48** 5741
[241] Mon K K and Binder K 1992 *J. Chem. Phys.* **96** 6989–95
[242] Monette L, Liu A J and Grest G S 1992 *Phys. Rev.* A **46** 7664–79
[243] Morishige K, Fujii H, Uga M and Kinukawa D 1997 *Langmuir* **13** 3494–8
[244] Morishige K and Kawano K 1998 *J. Chem. Phys.* **110** 4867–72
[245] Morishige K and Nobuoka K 1997 *J. Chem. Phys.* **107** 6965
[246] Morishige K and Shikimi M 1998 *J. Chem. Phys.* **108** 7821–4
[247] Müller E A and Gubbins K E 1998 *Carbon* **36** 1433–8
[248] Müller E A, Rull L F, Vega L F and Gubbins K E 1996 *J. Phys. Chem.* **100** 1189–96
[249] Müller E A, Vega L F and Gubbins K E 1995 *Int. J. Thermophys.* **16** 705–13

[250] Müller M and Paul W 1993 *J. Stat. Phys.* **73** 209–33
[251] Nagai T and Kawasaki K 1983 *Physica* A **120** 587–99
[252] Nakanishi H and Fisher M E 1983 *J. Chem. Phys.* **78** 3279–92
[253] Nardon Y and Lahrer Y 1974 *Surf. Sci.* **42** 299
[254] Neimark A V and Ravikovitch P I 1998 *Mat. Res. Soc. Symp. Proc.* **492** 27–33
[255] Neimark A V, Ravikovitch P I, Grun M, Schüth F and Unger K K 1998 *J. Colloid Interface Sci.* **207** 159–69
[256] Nham H S and Hess G B 1988 *Phys. Rev.* B **38** 5166–9
[257] Nicholson D 1987 *Surf. Sci.* **181** L189–92
[258] Nicholson D 1991 *Fundamentals of Adsorption* ed A B Mersmann and S E Scholl (New York: Engineering Foundation) pp 3–12
[259] Nicholson D 1994 *J. Chem. Soc., Faraday Trans.* **90** 181–5
[260] Nicholson D and Parsonage N G 1982 *Computer Simulation and the Statistical Mechanics of Adsorption* (London: Academic)
[261] Nicholson D and Pellenq R J M 1998 *Adv. Colloid. Interface Sci.* **76–77** 179–202
[262] Nicolaides D and Evans R 1989 *Phys. Rev. Lett.* **63** 778
[263] Norman G E and Filinov V S 1969 *High Temp. (USSR)* **7** 216–22
[264] Nosé S 1991 *Prog. Theor. Phys. Suppl.* **103** 1–46
[265] Nuttall S 1974 Adsorption and capillary condensation of xenon in porous glass and porous carbon *PhD Thesis* University of Bristol
[266] Olivier J P 1995 *J. Porous Mater.* **2** 9–17
[267] Olivier J P 1996 *Fundamentals of Adsorption* ed M D LeVan (Boston, MA: Kluwer) pp 699–707
[268] Olivier J P 1998 *Fundamentals of Adsorption* vol 6, ed F Meunier (Paris: Elsevier) pp 207–11
[269] Olivier J P 1998 *Carbon* **36** 1469–72
[270] Orkoulas G and Panagiotopoulos A Z 1999 *J. Chem. Phys.* **110** 1581
Orkoulas G and Panagiotopoulos A Z 1999 *J. Chem. Phys.* **110** 1590
[271] Oshida K and Endo M 1998 Private communication
[272] Overloop K and Van Gerven L 1993 *J. Magn. Res.* A **101** 179
[273] Page J H, Liu J, Abeles B, Deckman H W and Weitz D A 1996 *Phys. Rev. Lett.* **71** 1216–19
[274] Page K S and Monson P A 1996 *Phys. Rev.* E **54** 6557–64
[275] Page K S and Monson P A 1996 *Phys. Rev.* E **54** R29–32
[276] Palermo V, Biscarini F and Zannoni C 1998 *Phys. Rev.* E **57** R2519–22
[277] Palotás A B, Rainey L C, Feldermann C J, Sarofim A F and Van der Sande J B 1996 *Microsc. Res. Tech.* **33** 266–78
[278] Panagiotopoulos A Z 1987 *Mol. Phys.* **62** 701–19
[279] Panagiotopoulos A Z 1987 *Mol. Phys.* **61** 813–26
[280] Panagiotopoulos A Z 1992 *Mol. Simul.* **9** 1–23
[281] Panagiotopoulos A Z, Quirke N, Stapleton M and Tildesley D J 1988 *Mol. Phys.* **63** 527–45
[282] Pandit R, Schick M and Wortis M 1982 *Phys. Rev.* B **26** 5112
[283] Papadopoulou A, Van Swol F and Marini Bettolo Marconi U 1992 *J. Chem. Phys.* **97** 6942–52
[284] Park I A and MacElroy J M D 1989 *Mol. Simul.* **2** 105–45
[285] Patrick J W 1995 *Porosity in Carbons: Characterization and Applications* (New York: Halsted)
[286] Pekala R W and Alviso C T 1992 *Mat. Res. Soc. Symp. Proc.* **270** 3–14
[287] Pekala R W, Alviso C T, Kong F M and Hulsey S S 1992 *J. Non-Cryst. Solids* **145** 90–8
[288] Pellenq R J M and Nicholson D 1998 *Mol. Phys.* **95** 549–70
[289] Pérez L, Sokolowski S and Pizio O 1998 *J. Chem. Phys.* **109** 1147–51
[290] Peterson B K and Gubbins K E 1987 *Mol. Phys.* **62** 215–26
[291] Peterson B K, Gubbins K E, Heffelfinger G S, Marini Bettolo Marconi U and Van Swol F 1988 *J. Chem. Phys.* **88** 6487–500
[292] Peterson B K, Gubbins K E, Heffelfinger G S and Van Swol F 1990 *J. Chem. Phys.* **93** 679–85
[293] Peterson B K, Walton J P R B and Gubbins K E 1985 *Int. J. Thermophys.* **6** 585–93
[294] Peterson B K, Walton J P R B and Gubbins K E 1986 *J. Chem. Soc., Faraday Trans.* **2** 1789–800
[295] Phillips J M, Zhang Q M and Larese J Z 1993 *Phys. Rev. Lett.* **71** 2971–4
[296] Pissis P, Daoukaki-Diamanti D, Apekis L and Christodoulides C 1994 *J. Phys.: Condens. Matter* **6** L325
[297] Pissis P, Kyritsis A, Daoukaki D, Barut G, Pelster R and Nimtz G 1998 *J. Phys.: Condens. Matter* **10** 6205
[298] Pitard E, Rosinberg M L, Stell G and Tarjus G 1995 *Phys. Rev. Lett.* **74** 4361–4
[299] Pitard E, Rosinberg M L and Tarjus G 1996 *Mol. Simul.* **17** 399–419
[300] Privman V and Fisher M 1983 *J. Stat. Phys.* **33** 385
[301] Quirke N and Tennison S R R 1997 *Carbon* **34** 1281–6

[302] Radhakrishnan R and Gubbins K E 1997 *Phys. Rev. Lett.* **79** 2847–50
[303] Radhakrishnan R and Gubbins K E 1999 *Mol. Phys.* **96** 1249–67
[304] Radhakrishnan R, Gubbins K E and Sliwinska-Bartkowiak M 1999 *J. Chem. Phys.* submitted
[305] Radhakrishnan R, Gubbins K E, Watanabe A and Kaneko K 1999 *J. Chem. Phys.* at press
[306] Ramsay J D F and Booth B O 1991 *Fundamentals of Adsorption, Proc. 3rd Int. Conf.* ed A B Mersmann and S E Scholl (New York: Engineering Foundation) pp 701–14
[307] Ramsay J D F, Russell P J and Swanton S W 1991 *Characterization of Porous Solids* vol II, ed F Rodriguez-Reinoso *et al* (Amsterdam: Elsevier) pp 257–65
[308] Ranganathan S and Pathak K N 1992 *Phys. Rev.* A **45** 5789
[309] Rathousky J, Zukal A, Franke O and Schulz-Ekloff G 1995 *J. Chem. Soc., Faraday Trans.* **91** 937–40
[310] Ravikovitch P I, Domhnaill S C O, Neimark A V, Schüth F and Unger K K 1995 *Langmuir* **11** 4765–72
[311] Ravikovitch P I, Haller G L and Neimark A V 1998 *Adv. Colloid Interface Sci.* **76–77** 203–26
[312] Rhykerd C, Tan Z, Pozhar L A and Gubbins K E 1991 *J. Chem. Soc. Faraday Trans.* **87** 2011–16
[313] Rhykerd C L, Schoen M, Diestler D J and Cushman J H 1987 *Nature* **330** 461–3
[314] Röcken P, Somoza A, Tarazona P and Findenegg G H 1998 *J. Chem. Phys.* **108** 8689–97
[315] Röcken P and Tarazona P 1996 *J. Chem. Phys.* **105** 2034–43
[316] Rosinberg M L 1999 *New Approaches to Problems in Liquid State Theory (NATO Science Series C vol 529)* ed C Caccam *et al* (New York: Kluwer) p 245
[317] Rosinberg M L, Tarjus G and Stell G 1994 *J. Chem. Phys.* **100** 5172–7
[318] Ross S M 1997 *Simulation* 2nd edn (San Diego, CA: Academic)
[319] Saam W F 1983 *Surf. Sci.* **125** 253–64
[320] Samios S, Stubos A K, Kanellopoulos N K, Cracknell R F, Papadopoulos G K and Nicholson D 1997 *Langmuir* **13** 2796–802
[321] Sandburg K J 1992 *Bond Orientational Order in Condensed Matter Systems* (New York: Springer)
[322] Saravanan C and Auerbach S M 1999 *J. Chem. Phys.* submitted
[323] Sarkisov L, Page K S and Monson P A 1998 *Fundamentals of Adsorption* vol 6, ed F Meunier (Paris: Elsevier) pp 847–53
[324] Schmidt M and Löwen H 1996 *Phys. Rev. Lett.* **76** 4552
[325] Schoen M 1993 *Computer Simulation of Condensed Phases in Complex Geometries* (Berlin: Springer)
[326] Schoen M and Diestler D J 1997 *Chem. Phys. Lett.* **270** 339–44
[327] Schoen M and Diestler D J 1997 *Phys. Rev.* E **56** 4427–40
[328] Schoen M and Diestler D J 1998 *J. Chem. Phys.* **109** 5596–606
[329] Schüller J, Mel'nichenko Y B, Richert R and Fischer E W 1994 *Phys. Rev. Lett.* **73** 2224–7
[330] Schüller J, Richert R and Fischer E W 1995 *Phys. Rev.* B **52** 15 232
[331] Seaton N A, Walton J P R B and Quirke N 1989 *Carbon* **27** 853
[332] Segarra E I and Glandt E D 1993 *Chem. Eng. Sci.* **49** 2953
[333] Sing K S W, Everett D H, Haul R A, Moscou L, Pierotti R A, Rouquerol J and Siemineiewska T 1985 *Pure Appl. Chem.* **57** 603
[334] Sliwinska-Bartkowiak M 1999 to be published
[335] Sliwinska-Bartkowiak M, Gras J, Sikorski R, Radhakrishnan R, Gelb L D and Gubbins K E 1999 *Langmuir* at press
[336] Sliwinska-Bartkowiak M, Sikorski R, Sowers S L, Gelb L D and Gubbins K E 1997 *Fluid Phase Equilib.* **136** 93–109
[337] Sliwinska-Bartkowiak M, Sowers S L and Gubbins K E 1996 *Langmuir* **13** 1182–8
[338] Smit B and Frenkel D 1989 *Mol. Phys.* **68** 951–8
[339] Sokol P E, Ma W J, Herwig K E, Soon W M, Wang Y, Koplik J and Banavar J R 1992 *Appl. Phys. Lett.* **61** 777
[340] Steele W A 1973 *Surf. Sci.* **36** 317–52
[341] Steele W A 1974 *The Interaction of Gases with Solid Surfaces* (Oxford: Pergamon)
[342] Strange J H, Rahman M and Smith E G 1993 *Phys. Rev. Lett.* **71** 3589
[343] Strickland B, Leptoukh G and Roland C 1995 *J. Phys. A: Math. Gen.* **28** L403–8
[344] Sullivan D E and Telo da Gama M M 1986 *Fluid Interfacial Phenomena* ed C A Croxton (Chichester: Wiley) pp 45–134
[345] Sutton M, Mochrie S G J and Birgeneau R J 1983 *Phys. Rev. Lett.* **51** 407
[346] Tan Z and Gubbins K E 1992 *J. Phys. Chem.* **96** 845–54
[347] Tan Z, Van Swol F and Gubbins K E 1987 *Mol. Phys.* **62** 1213–24
[348] Tarazona P 1985 *Phys. Rev.* A **31** 2672–9
[349] Tarazona P, Marini Bettolo Marconi U and Evans R 1987 *Mol. Phys.* **60** 573–95
[350] Tell J L, Maris H J and Seidel G M 1983 *Phys. Rev.* B **28** 5122

[351] Telo da Gama M M, Tarazona P, Allen M P and Evans R 1990 *Mol. Phys.* **71** 801–21
[352] Teraoka Y 1993 *Surf. Sci.* **294** 273–83
[353] Teraoka Y and Seto T 1993 *Surf. Sci.* **283** 371–6
[354] Thommes M and Findenegg G H 1994 *Langmuir* **10** 4270–7
[355] Thommes M, Findenegg G H and Schoen M 1995 *Langmuir* **11** 2137–142
[356] Thompson P A and Robbins M O 1990 *Science* **250** 792–4
[357] Thompson S M, Gubbins K E, Walton J P R B, Chantry R A R and Rowlinson J S 1984 *J. Chem. Phys.* **81** 530
[358] Torii R H, Maris H J and Seidel G M 1990 *Phys. Rev.* B **41** 7167
[359] Torrie G M and Valleau J P 1974 *Chem. Phys. Lett.* **28** 578
[360] Tovbin Y K and Votyakov K V 1993 *Langmuir* **9** 2652–60
[361] Trokhymchuk A and Sokolowski S 1998 **109** 5044–9
[362] Ulberg D E and Gubbins K E 1995 *Mol. Phys.* **84** 1139–53
[363] Unger K K 1979 *Porous Silica (Journal of Chromatography Library Vol 16)* (Amsterdam: Elsevier)
[364] Unruh K M, Huber T E and Huber C A 1993 *Phys. Rev.* B **48** 9021
[365] Van Megen W and Snook I K 1982 *Mol. Phys.* **45** 629–36
[366] Van Megen W and Snook I K 1985 *Mol. Phys.* **54** 741–55
[367] Vanderlick T K, Scriven L E and Davis H T 1989 *J. Chem. Phys.* **90** 2422–36
[368] Van Duijneveldt J S and Frenkel D 1992 *J. Chem. Phys.* **96** 4655
[369] Vega L F, Müller E A, Rull L F and Gubbins K E 1995 *Mol. Simul.* **15** 141–54
[370] Vega L F, Müller E A, Rull L F and Gubbins K E 1996 *Adsorption* **2** 59–68
[371] Velasco E and Toxvaerd S 1996 *Phys. Rev.* E **54** 605–10
[372] Vishnyakov A, Piotrovskaya E M and Brodskaya E N 1998 *Adsorption* **4** 207–24
[373] Van Roij R, Dijkstra M and Evans R 1999 *Phys. Rev. Lett.* submitted
[374] Van Slooten R, Bojan M J and Steele W A 1994 *Langmuir* **10** 542–8
[375] Voronov V P and Buleĭko V M 1998 *J. Exp. Theor. Phys.* **86** 586–90
[376] Votyakov E V, Tovbin Yu K, MacElroy J M D and Roche A 1999 *Langmuir* **15** 5713–21
[377] Wall G D and Cleaver D J 1997 *Phys. Rev.* E **56** 4306–16
[378] Walton J P R B and Quirke N 1989 *Mol. Simul.* **2** 361–91
[379] Warnock J, Awschalom D D and Shafer M W 1986 *Phys. Rev. Lett.* **57** 1753
[380] Watanabe A, Iiyama T, Kaneko K, Radhakrishnan R and Gubbins K E 1999 *J. Phys. Chem.* at press
[381] Watanabe A and Kaneko K 1999 *Chem. Phys. Lett.* at press
[382] Weeks J D, Chandler D and Andersen H C 1971 *J. Chem. Phys.* **54** 5237–47
[383] Weissenberger M C, Göltner C G and Antonietti M 1997 *Ber. Bunsenges. Phys. Chem.* **101** 1679
[384] White J C and Hess A 1993 *J. Phys. Chem.* **97** 6398
White J C and Hess A 1993 *J. Phys. Chem.* **97** 8703
[385] Wilding N B 1995 *Phys. Rev.* E **52** 602–11
[386] Wilding N B and Bruce A D 1992 *J. Phys.: Condens. Matter* **4** 3087–108
[387] Wilding N B and Schoen M 1999 *Phys. Rev.* E at press
[388] Wiltzius P, Dierker S B and Dennis B S 1989 *Phys. Rev. Lett.* **62** 804–7
[389] Wong A P Y and Chan M H W 1990 *Phys. Rev. Lett.* **65** 2567–70
[390] Wong A P Y, Kim S B, Goldburg W I and Chan M H W 1993 *Phys. Rev. Lett.* **70** 954–7
[391] Woods G B, Panagiotopoulos A Z and Rowlinson J S 1988 *Mol. Phys.* **63** 49
[392] Yoon D V, Vacatello M and Smith G D 1995 *Monte Carlo and Molecular Dynamics Simulations in Polymer Science* ed K Binder (New York: Oxford University Press) ch 8
[393] Yoon J, Sergatskov D, Ma J, Mulders N and Chan M H W 1998 *Phys. Rev. Lett.* **80** 1461–4
[394] Youn H S and Hess G B 1990 *Phys. Rev. Lett.* **64** 443
[395] Youn H S, Meng X F and Hess G B 1993 *Phys. Rev.* B **48** 14 556–76
[396] Zhang Z and Chakrabarti A 1994 *Phys. Rev.* E **50** R4290–3
[397] Zhang Z and Chakrabarti A 1995 *Phys. Rev.* E **52** 4991–9
[398] Zhang Z and Chakrabarti A 1995 *Phys. Rev.* B **52** 2736–41
[399] Zhuang Z, Casielles A G and Cannell D S 1996 *Phys. Rev. Lett.* **77** 2969–72